

# **Methods for Computational Design Optimization of Fluid-Structure Systems: A Thesis Proposal**

by

Nicholas Jenkins

B.S. Mechanical Engineering, Oregon State University, 2009.

M.S. Aerospace Engineering Sciences, University of Colorado,  
Boulder, 2013.

---

---

## Contents

<b>List of Figures</b>	<b>5</b>
<b>1 Introduction</b>	<b>10</b>
1.1 Computational Design Optimization of Multiphysics Systems . . . . .	10
1.2 Fluid-Structure Interaction . . . . .	12
<b>2 Finite Elements for Incompressible Fluid-Structure Interaction</b>	<b>13</b>
2.1 Incompressible Navier-Stokes . . . . .	14
2.2 Galerkin Finite Element Discretization . . . . .	15
2.3 Numerical Instabilities and Stabilization . . . . .	17
2.3.1 Numerical Example: Unsteady Flow around a Cylinder . . . . .	18
2.4 Arbitrary-Lagrangian-Eulerian (ALE) Reference Frame . . . . .	22
2.4.1 Time Integration with the ALE method . . . . .	23
2.4.2 Auxiliary Mesh Motion Elastic Field . . . . .	25
2.4.3 Numerical Example: Pitching NACA 0012 Airfoil . . . . .	26
2.5 Elasticity . . . . .	29
2.5.1 Material Models . . . . .	30
2.5.2 Linear Elastic Model . . . . .	30
2.5.3 St. Venant Kirchhoff Model . . . . .	30
2.5.4 Structural Time Integration . . . . .	32
2.6 Monolithic Fluid-Structure Interaction via Residual Coupling Scheme	32
2.6.1 Numerical Example: Stationary Beam in Fluid Channel . . . . .	35

2.6.2	Numerical Example: Transient Cylinder-Flag structure in Fluid Channel . . . . .	38
2.6.3	Numerical Example: Transient Cylinder-Flag structure in 3D Fluid Channel . . . . .	40
2.7	Computer Programming and Utilities . . . . .	44
2.7.1	Code Development . . . . .	44
2.7.2	Pre-Processing . . . . .	44
2.7.3	Post-Processing . . . . .	44
2.7.4	Linear Solvers and Preconditioners . . . . .	44
2.8	Global Optimization and Sensitivity Analysis . . . . .	45
2.8.1	Sensitivity Analysis . . . . .	48
<b>3</b>	<b>Summary of <i>The Level Set and Extended Finite Element Methods for Topology Optimization of Fluid-Structure Interaction Problems.</i></b>	<b>50</b>
<b>4</b>	<b>Generalized Lagrangian XFEM for Fluid-Structure Interaction</b>	<b>52</b>
4.1	The XFEM for Immersed Boundaries in Incompressible Flow . . .	55
4.1.1	Numerical Example: Unsteady Flow about an immersed Cylinder . . . . .	56
4.2	Stabilized Lagrange Multipliers for Fluid-Structure Coupling . . .	59
4.2.1	Numerical Examples: Stationary FSI using LSM-XFEM .	62
4.2.2	Numerical Example: Deforming NACA 65 Airfoil in Channel Flow . . . . .	68
4.2.3	Numerical Example: Unsteady Cylinder-Flag Fluid-Structure Interaction . . . . .	71
<b>5</b>	<b>Fully Eulerian Fluid-Structure Interaction</b>	<b>74</b>

5.1	Dynamically Evolving Level Set / XFEM Interface with Hamilton-Jacobi Equation . . . . .	75
5.1.1	Numerical Example: Translating Level Set Field via modified Hamilton-Jacobi Formulation . . . . .	77
5.1.2	Numerical Example: Vertically moving Cylinder in Channel Flow . . . . .	78
5.2	Eulerian Structural Mechanics . . . . .	80
<b>6</b>	<b>Conclusion and Thesis Time Frame</b>	<b>83</b>
<b>7</b>	<b>Bibliography</b>	<b>87</b>
<b>8</b>	<b>Appendix</b>	<b>92</b>

**A Pre-Print: The Level Set and Extended Finite Element Methods for Topology Optimization of Fluid-Structure Interaction Problems**

## List of Figures

1	(i) Various physics in automotive applications. [1]. (ii) Fretting crack propagation, which is reduction in fatigue strength in contacting manufacturing.[2] . . . . .	10
2	Topology optimization used for pressure-actuated morphing wing aircraft. [3] . . . . .	12
3	(i) US Air Force Dragonfly Drone MAV [4]. (ii) Arterial wall, hemodynamics illustration[5]. (iii) Off-shore wind farm. . . . .	13
4	Overall cylinder mesh used in the simulation. . . . .	19
5	Zoomed view near the cylinder of the mesh. . . . .	19
6	Cylinder Flow (i) Velocity Norm Contours. (ii) Pressure Contours.	20
7	Lift, Drag, and coefficients evolution for the unsteady cylinder test.	21
8	0 degree Angle of Attack:(i) Pressure. (ii) Velocity Norm. (iii) Mesh. . . . .	27
9	20 degree Angle of Attack: (i) Pressure. (ii) Velocity Norm. (iii) Mesh. . . . .	27
10	Pitching NACA0012 Airfoil Lift ALE Comparison. . . . .	28
11	Computational mesh used for the stationary FSI beam problem. . . . .	35
12	FSI Beam (i) Pressure solution. (ii) Velocity norm solution. . . . .	36
13	FSI Beam (i) Volumetric stress in y-direction. (ii) von Mises stress.	37
14	Transient FSI cylinder-flag (i) Pressure contours. (ii) Velocity norm contours. (iii) Fluid Mesh. (iv) Structure with von Mises stress contours. . . . .	39

15	Transient FSI cylinder-flag (i) Horizontal displacement of flag tip overlaid in red with benchmark results. (ii) Vertical displace- ment of flag tip overlaid in red with benchmark results. . . . .	39
16	3D cylinder-flag geometry . . . . .	40
17	3D FSI Cylinder-Flag (i) $yz$ -plane mesh. (ii) $xz$ -plane mesh. (iii) $xy$ -plane mesh. . . . .	41
18	3D FSI Cylinder-Flag (i) $y$ -displacement at $x=0.32$ m. (ii) -displacement at $x=0.6$ m (rear edge of flag). . . . .	42
19	3D FSI Cylinder-Flag (i) Structural displacement. (ii) Fluid ve- locity and structural displacement. . . . .	42
20	3D FSI Cylinder-Flag fluid pressure on FSI interface. (ii) Fluid pressure on FSI interface. . . . .	43
21	Illustration of optimality point in a two dimensional design space.	47
22	AeroElastic Optimization Schemes . . . . .	52
23	Zoomed view of the XFEM triangulated interface mesh for the cylinder. . . . .	56
24	Unsteady cylinder flow (i) Un-intersected fixed grid mesh. (ii) Velocity contours. (iii) Pressure contours. . . . .	57
25	Aerodynamic Coefficients for the Body Fitted and LSM-XFEM for the unsteady cylinder benchmark. . . . .	58
26	LSM-XFEM FSI Beam (i) Body Fitted Solution. (ii) LSM-XFEM with Stab. Lagrange Multipliers solution. . . . .	62
27	The LSM-XFEM structural solution plotted with the body fitted fluid solution. . . . .	63
28	FSI Beam problem sweep for mesh resolutions and velocity penalty.	63

29	Stationary FSI cylinder sweep errors in (i) Displacement at interface. and (ii). Velocity at interface. . . . .	65
30	Stationary FSI cylinder sweep Elastic modulus 1.0e4 results for $k_{vel}$ and $k_{disp}$ sweep. . . . .	66
31	Stationary FSI cylinder resolution Sweep. . . . .	67
32	L2-errors in x-velocity for stationary FSI cylinder resolution Sweep.	67
33	Problem setup for the FSI NACA 65 example. The line from the nose point to the bottom of the support region is 0.025 . . . . .	68
34	FSI NACA 65 Airfoil (i) Velocity contours. (ii). Pressure contours.	69
35	The Lift and Drag evolution for the NACA 65 FSI example. . . . .	70
36	Transient FSI Cylinder-Flag Problem (i) Velocity contours. (ii) Deformed fluid mesh. (ii) Pressure contours. (iv) Deformed structural mesh. . . . .	72
37	Generalized LSM-XFEM Method overlayed <b>in red</b> with Turek, et al results for the third FSI benchmark case. . . . .	73
38	Translating circle Level Set field via Hamilton-Jacobi equation. . .	77
39	Vertically moving cylinder in parabolic channel flow of $Re = 10$ . .	78
40	Thesis development and results timeline. . . . .	86

Jenkins, Nicholas.

Methods for Computational Design Optimization of Fluid-Structure Systems: A Thesis Proposal

Thesis directed by Prof. Dr. Kurt Maute

This thesis proposal presents novel methods for topology optimization of fluid-structure interaction (FSI) problems, and proposes additional plans for even more efficient and robust methods to accomplish this task. Section 1 gives a brief introduction and motivation for design optimization of multiphysics systems, namely fluid-structure interacting applications. Section 2 presents theory and applications for incompressible viscous flow using stabilized finite elements in an arbitrary-Lagrangian-Eulerian (ALE) reference frame. A monolithic coupling is introduced to couple the flow with an elasto-dynamic field. Stationary and transient examples with both linear and nonlinear structural models are presented, and compared with well-known literature benchmarks. Theory for nonlinear constrained optimization and sensitivity analysis is also presented.

Section 3 presents a summary of a pre-print of the future publication: *The Level Set and Extended Finite Element Methods for Topology Optimization of Fluid-Structure Interaction Problems*, which can be found in Appendix A.

Section 4 presents a generalization of the previously presented method for topology optimization of the fluid-structure problem. The generalized method uses a Level Set field to distinguish between fluid and structure, eliminating the need for a body fitted mesh. Stabilized Lagrange multipliers are employed to couple the fluid to the immersed structural boundary. Convergence and errors are investigated, and numerical examples are presented and compared to literature benchmarks.

Section 5, is devoted to the proposal of the final thesis goal: topology optimization of fully Eulerian fluid-structure interaction analyses. Some numerical examples of dynamically evolving immersed boundaries are presented, along with theory for Eulerian structural mechanics. Foreseeable challenges are discussed.

The document is concluded in section 6 where a list of milestones is presented, accompanied by a time line for the remainder of the year.

## 1. Introduction

### 1.1. Computational Design Optimization of Multiphysics Systems

Toward the end of the twentieth century, engineers have become increasingly interested in the analysis and design of multiphysics systems. Multiphysics systems in this context refers to more than one discipline in one system. Most, if not all, realistic engineering systems are multidisciplinary in nature, yet are typically approximated or idealized due to limited analysis tools and methods. With the advent of parallel computing and computational tools developed by researchers across the world, modeling of multiphysics systems has taken a giant leap in the past three decades. Multiphysics modeling is becoming increasingly more sought after with the development of innovative applications like: morphing wing aircraft, bio-mimetic applications, electric transport, renewable energy sources, and much more. Figure 1 shows two examples of multiphysics applications: (i) integrated automotive systems; (ii) crack propagation due to fretting in an industrial manufacturing process. Modeling multiphysics systems is cumbersome due to contrasting spatial and temporal scales of each discipline which result in stiff problems. Further difficulties arise from numerical models that perform well for one type of physics, and not others.

Design Optimization also became popular toward the end of the twentieth century. Commonly displaying familiar black and white images of simple truss-like optimal structural designs, optimization methods are adapting to tackle some of the world's most challenging and complex engineering problems. Figure 2 show a topology optimized pressure-actuated morphing aircraft wing.

Applying computational optimization to a multiphysics analysis gives rise to further challenges. Multiphysics problems exhibit more complex and higher di-



Figure 1: (i) Various physics in automotive applications. [1]. (ii) Fretting crack propagation, which is reduction in fatigue strength in contacting manufacturing.[2]

mensional design spaces due to their coupled nature, making for a more difficult search, and greater susceptibility to local minima. A multiphysics system is also typically more sensitive to ill-posed candidate designs (leading to numerical instabilities), causing the user to over-constrain the design problem leading to more conservative design performance. Optimization by nature is an expensive pursuit. It is not uncommon for search algorithms to need hundreds of design evaluations. Multiphysics analyses often require a greater degree of grid refinement to resolve the coupled response. Given these facts, finding the global optimum for a realistic (3D, transient) engineering problem can be immensely computationally expensive.

Notable names in commercial industry are COMSOL Multiphysics and ANSYS for performing optimization of multiphysics systems, but from an academic point of view, there is still much research to be done. This thesis proposal aims at raising the bar with the development of new solution methods for these kinds of tasks.

This work proposes some relief to these challenges associated with computa-



Figure 2: Topology optimization used for pressure-actuated morphing wing aircraft. [3]

tional optimization of multiphysics systems, namely gradient based optimization of two-way coupled, large deflection, incompressible fluid-structure systems.

### 1.2. Fluid-Structure Interaction

Fluid-structure interaction (FSI) includes aero-elasticity (air flow applications), and liquid-solid (hydro-elasticity), and any other fluid interacting with a structure. Some examples of FSI are given in figure 3: a micro-aerial-vehicle with very thin flapping wings, arterial walls in the human body, and an offshore wind farm. These examples all have in common the need for a fully integrated FSI analysis. A purely fluid, or even one-way coupled analysis would most likely be a poor approximation to the physical response. Additionally, the evolution of the fluid-structure system is probably highly non-intuitive. From a modeling standpoint, a fluid dynamics model can exert elliptic, parabolic, or hyperbolic characteristics in the same domain, depending on the Reynolds and Mach numbers. Coupling these highly nonlinear differential equations to a nonlinear elasto-dynamic structural equation, only magnifies the counter-intuition that the FSI problem could exhibit.

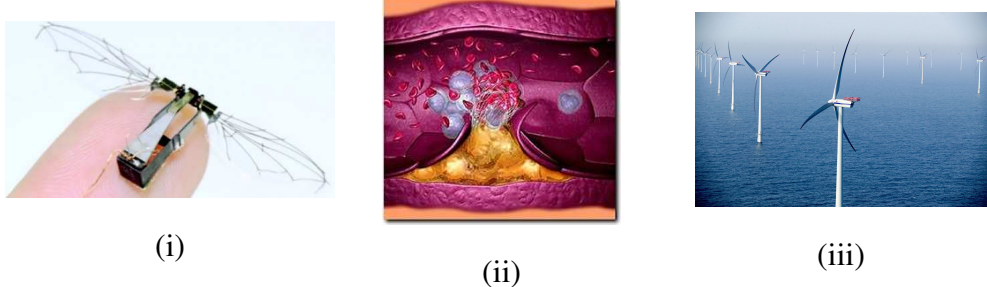


Figure 3: (i) US Air Force Dragonfly Drone MAV [4]. (ii) Arterial wall, hemodynamics illustration[5]. (iii) Off-shore wind farm.

Potentially the greatest challenge associated with modeling fluid-structure interacting systems is a product of unifying a material which reacts as a function of the rate of shear, with a material which responds as a function of the amount it's molecules are displaced. This is why fluids are almost always modeled in an Eulerian reference frame, and solids are almost always modeled in a Lagrangian reference frame. Consequently, the governing equations for the fluid and structure have very different forms, dimensions, and physics scales.

This proposal presents previously developed methods for modeling fluid-structure action, yet applies new methods for design optimization. However, later proposes less conventional FSI modeling methods in order to be used in unison with design optimization.

## 2. Finite Elements for Incompressible Fluid-Structure Interaction

The Finite Element Method (FEM), have emerged as a competent method for computational fluid dynamics (CFD) with the advent of stabilization methods. Additionally, the FEM is convenient for integration with topology optimization and sensitivity analysis frameworks. To this end, an FEM fluid dynamics solver

is to be coupled with a FEM structural discretization subsequently. All work presented in this document use bilinear/trilinear interpolation with QUAD4 and HEX8 finite elements.

### 2.1. Incompressible Navier-Stokes

Conservation of mass of each infinitesimal piece of fluid material obeys conservation of mass:

$$\frac{\partial \rho^f}{\partial t} + \frac{\partial (\rho^f v_i)}{\partial x_i} = \frac{\partial \rho^f}{\partial t} + \rho^f \frac{\partial v_i}{\partial x_j} + v_i \frac{\partial \rho^f}{\partial x_j} = 0 \quad (1)$$

where for an incompressible fluid the volume remains unchanged in time, forcing the density to remain unchanged in space and time.  $v_i$  is the fluid velocity in the  $i$ th direction,  $\rho^f$  is the fluid density,  $\frac{\partial}{\partial t}$  and  $\frac{\partial}{\partial x_j}$  are partial derivatives with respect to time, and spatial direction  $j$ , respectively. Requiring no dilation or contraction of the fluid volume leads to the conservation of mass for an incompressible flow, often referred to as the incompressibility condition:

$$\frac{\partial v_i}{\partial x_i} = 0 \quad (2)$$

which states the velocity is a divergence free field. Conservation of momentum is derived by first invoking Newton's Second Law per each fluid volume:

$$\rho_f \frac{Dv_i}{Dt} = F_i \quad (3)$$

where  $\frac{D}{Dt}$  is the total material derivative, where for an Eulerian reference frame, is given by:

$$\frac{D\phi}{Dt} = \frac{\partial v_i}{\partial t} + v_j \frac{\partial v_i}{\partial x_j} \quad (4)$$

The material derivative takes into account the total time derivative of the quantity  $v_i$  whilst accounting for the deforming material advecting through the fixed frame.

$F_i$  is the sum of forces in the  $i$ th direction. Using equation 4 to expand the left side of equation 3, and expanding the total forces into internal and external forces on the fluid volume:

$$\rho^f \left( \frac{\partial v_i}{\partial t} + v_j \frac{\partial v_i}{\partial x_j} \right) = \frac{\partial \sigma_{ij}^f}{\partial x_j} + g_i \quad (5)$$

where  $\sigma_{ij}^f$  and  $g_i$  are the fluid Cauchy stress tensor and external forces in the  $i$ th direction, respectively. The constitutive relation for a Newtonian, isotropic, incompressible fluid, taking into account stress tensor symmetry (conservation of angular momentum), is

$$\sigma_{ij}^f = -p\delta_{ij} + \mu \left( \frac{\partial v_j}{\partial x_i} + \frac{\partial v_i}{\partial x_j} \right) \quad (6)$$

where  $p$  is the fluid *mechanical pressure*,  $\delta_{ij}$  is the Kronicker Delta, and  $\mu^f$  is the fluid dynamic viscosity. Note the pressure is defined as a mechanical pressure because there is no equation of state to determine a thermodynamic pressure, and in fact gradients of the pressure can only be computed for the incompressible fluid equations.[6]. Dropping the external body force terms, and substituting the constitutive relation in equation 6 into equation 5, the common form of the incompressible Navier-Stokes equations is:

$$\rho^f \left( \frac{\partial v_i}{\partial t} + v_j \frac{\partial v_i}{\partial x_j} \right) = \frac{\partial}{\partial x_j} \left( -p\delta_{ij} + \mu \left( \frac{\partial v_j}{\partial x_i} + \frac{\partial v_i}{\partial x_j} \right) \right) \quad (7)$$

The intent is to solve equation 7 in the domain  $\Omega^f$  subject to the essential boundary conditions:

$$v_i = \tilde{v}_i \quad \text{on} \quad \Gamma \quad (8)$$

## 2.2. Galerkin Finite Element Discretization

Casting the incompressible Navier-Stokes equations (equations 2 and 7) into variational form by multiplying them by an appropriate weighting function, and integrating them over discrete domain  $\Omega^f$ :

$$R^v = \int_{\Omega^f} \delta v_i \left( \rho^f \left( \frac{\partial v_i}{\partial t} + v_j \frac{\partial v_i}{\partial x_j} \right) - \frac{\partial}{\partial x_j} \left( -p \delta_{ij} + \mu \left( \frac{\partial v_j}{\partial x_i} + \frac{\partial v_i}{\partial x_j} \right) \right) \right) d\Omega = 0 \quad (9)$$

$$R^p = \int_{\Omega^f} \delta p \frac{\partial v_i}{\partial x_i} d\Omega = 0 \quad (10)$$

where  $\delta v_i$  and  $\delta p$  are the test functions associated with the fluid velocity and pressure, respectively. Equation 9 is the residual equation for the fluid velocity, and due to the state variable of the governing equation is in units of power ( $\frac{J}{s}$ ). It is inferred that the trial solutions that minimize the residual (equation 9 and 10) are the solutions of the incompressible Navier-Stokes equations.

Next to satisfy the bilinear form and generate a natural boundary condition [7], the higher order derivatives are reduced in order by integrating by parts. For convenience later on, however, the entire stress tensor term in equation 9 will be integrated by parts, and the Divergence Theorem applied keeping in mind the variation of a quantity is zero on the boundary due to the essential boundary condition. For clarity the stress tensor is kept intact for these next steps:

$$\int_{\Omega} \delta v_i \frac{\partial \sigma_{ij}^f}{\partial x_j} d\Omega = \int_{\Omega} \left( -\frac{\partial \delta v_i}{\partial x_j} \sigma_{ij}^f + \frac{\partial \delta v_i \sigma_{ij}^f}{\partial x_j} \right) d\Omega \quad (11)$$

$$\cancel{2 \delta v_i \sigma_{ij}^f \Big|_{\Gamma^f}}^0 - \int_{\Omega^f} -\frac{\partial \delta v_i}{\partial x_j} \sigma_{ij}^f d\Omega + \underbrace{\int_{\Omega^f} \frac{\partial \delta v_i \sigma_{ij}^f}{\partial x_j} d\Omega}_{\text{Divergence Theorem}} \quad (12)$$

$$\int_{\Omega} \delta v_i \frac{\partial \sigma_{ij}^f}{\partial x_j} d\Omega = - \int_{\Omega^f} -\frac{\partial \delta v_i}{\partial x_j} \sigma_{ij}^f d\Omega + \int_{\Gamma^f} \delta v_i \sigma_{ij}^f \hat{n}_j^f d\Gamma \quad (13)$$

where  $\hat{n}_i^f$  is the *i*th component of the outward facing normal for the fluid. Modifying the Navier-Stokes equations in 9:

$$R^v = \int_{\Omega^f} \left( \delta v_i \rho^f \left( \frac{\partial v_i}{\partial t} + v_j \frac{\partial v_i}{\partial x_j} \right) + \frac{\partial \delta v_i}{\partial x_j} \sigma_{ij}^f \right) d\Omega - \int_{\Gamma^f} \delta v_i \sigma_{ij}^f \hat{n}_j^f d\Omega \quad (14)$$

$$R^p = \int_{\Omega^f} \delta p \frac{\partial v_i}{\partial x_i} d\Omega = 0 \quad (15)$$

### 2.3. Numerical Instabilities and Stabilization

Finite Elements were first developed for structural and diffusion problems, which yield a symmetric stiffness matrices, and provide bounded deviation from analytical solutions with respect to grid refinement [8]. Convection dominated flows such as the Navier-Stokes equations, or advection-diffusion problems, yield spurious oscillations and require a highly refined grid to approach a diffusion dominated problem on the elemental level. The streamline upwind Petrov/Galerkin (SUPG) method is chosen to alleviate these instabilities. The SUPG scheme adds in numerical diffusion from upwinding (forward differences) in a sophisticated way, that is dependent upon the Peclet number and element area. Employing equal order (bilinear, and linear) interpolation bases for both the velocity vector space, and the pressure scalar space, leads to pressure oscillations. Thus a pressure stabilizing Petrov/Galerkin (PSPG) [8],[9] method is used. The SUPG/PSPG scheme stabilizes the system by multiplying the entire governing equation by a new Petrov-Galerkin based test function  $\eta_i^{PG}$ :

$$\begin{aligned} R^v &= \int_{\Omega^f} \left( \delta v_i \rho^f \left( \frac{\partial v_i}{\partial t} + v_j \frac{\partial v_i}{\partial x_j} \right) + \frac{\partial \delta v_i}{\partial x_j} \sigma_{ij}^f \right) d\Omega - \int_{\Gamma^f} \delta v_i \sigma_{ij}^f \hat{n}_j^f d\Gamma \\ &\quad + \sum_{n_{elem}} \int_{\Omega^f} \eta_i^{PG} \left( \rho^f \left( \frac{\partial v_i}{\partial t} + v_j \frac{\partial v_i}{\partial x_j} \right) - \frac{\partial \sigma_{ij}^f}{\partial x_j} \right) d\Omega \end{aligned} \quad (16)$$

$$\eta_i^{PG} = v_j \frac{\partial \delta v_i}{\partial x_j} \tau_{SUPG} + \frac{1}{\rho^f} \frac{\partial \delta p}{\partial x_j} \tau_{PSPG} \quad (17)$$

$$\tau_{SUPG} = \frac{h}{2\|\hat{v}_i\|} z(Re_v) \quad \tau_{PSPG} = \frac{h^\#}{2\|V\|} z(Re_V^\#)$$

$$Re_v = \frac{\|\hat{v}_i\| h}{2\nu} \quad Re_V^\# = \frac{\|V\| h^\#}{2\nu}$$

$$h = 2 \left( \sum_{a=1}^{n_{en}} |s \cdot \nabla N_a| \right)^{-1} \quad z(Re) = \begin{cases} Re/3 & \text{if } 0 \leq Re \leq 3 \\ 1 & \text{if } 3 \leq Re. \end{cases}$$

where  $h$  and  $h^\#$  are element area/volume measures,  $V$  is the so-called *global scaling velocity* that should be equal to the reference (eg. inflow) velocity.  $\nu^f$  is the fluid kinematic viscosity,  $N_a$  is the element shape function. Refer to [9] for further details on the SUPG/PSPG stabilization scheme.

The fluid equations are solved using the second-order (3-point) BDF (Backward Difference Formula) time integration scheme. This scheme will not be discussed here as it's common, and easy to reference in any text book.

### 2.3.1. Numerical Example: Unsteady Flow around a Cylinder

The following benchmark problem was taken from [10] as the two-dimesional case 2 problem setup (2D-2). The problem is unsteady, incompressible flow about a cylinder in a channel. The inflow velocity profile is parabolic with mean velocity of  $1.0 \frac{m}{s}$ , and the outlet is traction free ( $\sigma_{ij}^f \hat{n}^f = 0$ ). The density and dynamic viscosity are  $1.0 \frac{kg}{m^3}$  and  $0.001 \frac{kg}{ms}$ , respectively.

The cylinder was run with 6990 degrees of freedom, and a time step of  $0.005s$ , and the simulation was run to a final time of  $10.0s$ . Figures 4 and 5 show the

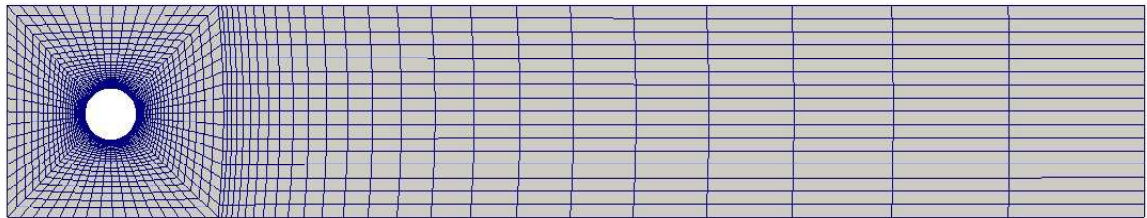


Figure 4: Overall cylinder mesh used in the simulation.

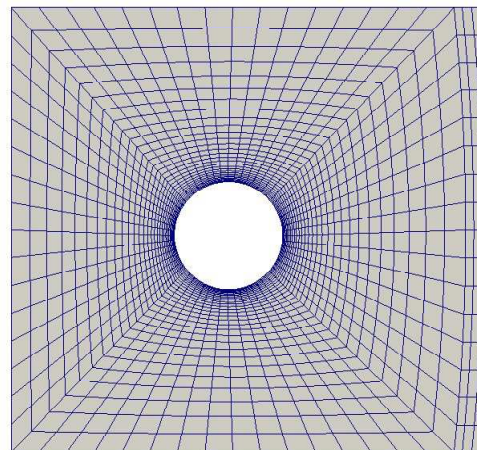


Figure 5: Zoomed view near the cylinder of the mesh.

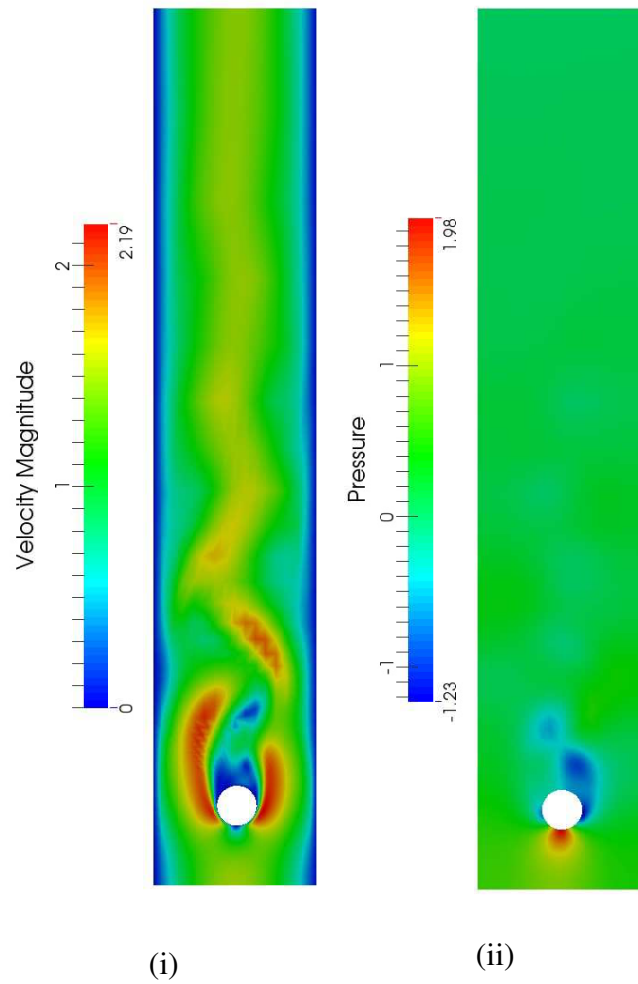


Figure 6: Cylinder Flow (i) Velocity Norm Contours. (ii) Pressure Contours.

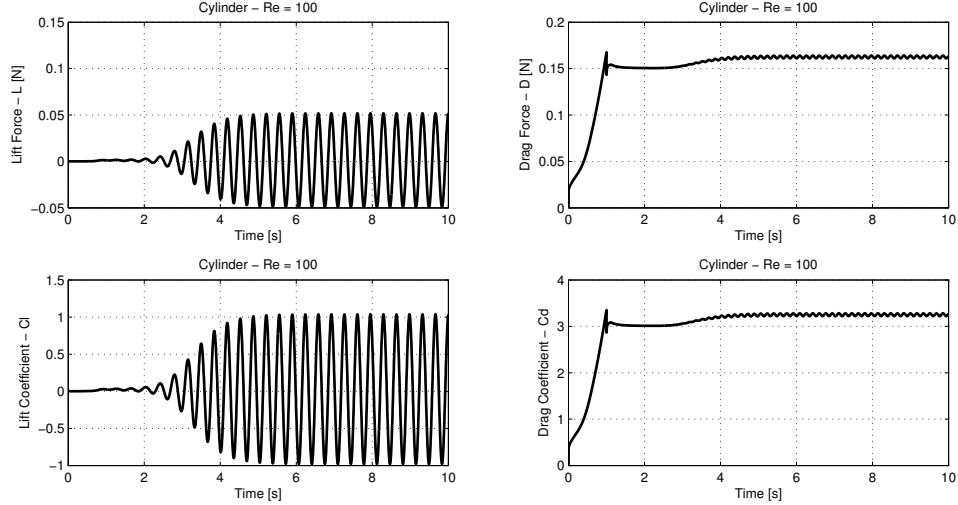


Figure 7: Lift, Drag, and coefficients evolution for the unsteady cylinder test.

computational mesh employed in the simulation. Figure 6 show the velocity norm and pressure contours at the final time of 10 seconds.

The evolution of the lifting force, drag force, and lift ( $C_l$ ) and drag ( $C_d$ ) coefficients are give in figure 7.

A frequency analysis on these responses yields a frequency of oscillation  $f$  of **2.9197**. This is then used to compute the Strouhal number for the cylinder simulation:

$$St = \frac{fD}{V_\infty} = 0.2915$$

where  $D$  is the cylinder diameter, equal to 0.1, and  $V_\infty$  is the reference (inflow) mean velocity, equal to  $1.0 \frac{m}{s}$ . **St=0.29197** lies conservatively within the bounds of the results in Schafer and Turek's study, which range from 0.2880 to 0.3050. Further, the maximum value for  $C_l$  was **1.01341** which also lines up well with results from said study, which range from 0.9632 to 1.0740.

#### 2.4. Arbitrary-Lagrangian-Eulerian (ALE) Reference Frame

The ALE method was originally proposed in 1960s and was later developed further by National Labs for robustness in Lagrangian hydrocodes. Donea, et al [11] were one of the first groups to employ the ALE method for fluid-structure interaction of coupled, transient systems, namely for analysis of nuclear reactors. Today, ALE is a popular and widely used method in many commercial and research codes, yet has seen limited use in the context of design optimization.

The concept of ALE is to generalize the fluid Eulerian grid to translate in a Lagrangian fashion. Where now each grid vertex is given degrees of freedom, similar to a structural analysis. Different methods exist for how to handle these extra degrees of freedom, but a common approach is to assign an auxiliary elastic field to keep the mesh smooth and from tangling on itself. This field is sometimes referred to as a Laplacian, or second-derivative field because it can be modeled as a simple linear elastic stress field. The mesh displacement is prescribed or constrained (via the coupling method) at boundaries such that it is one-way coupled, and the fluid feels no stiffness to mesh deformation. The modification of the governing equation hinges on the fact that the form of the total material derivative accounts for the relative motion of a material point as seen from an observer fixed on grid point. Now that relative motion is modified by the fact that the grid point is moving. Recalling the total material derivative for a fluid, equation 4 is modified to account for the ALE reference frame:

$$\frac{Dv_i}{Dt} = \frac{\partial v_i}{\partial t} + \hat{v}_j \frac{\partial v_i}{\partial x_j} \quad (18)$$

where the velocity at which the state variable (fluid velocity) is convected ( $\hat{v}_i$ ) is now not directly equal to the fluid velocity, but a function of the mesh rate of mesh

displacement as well:

$$\hat{v}_i = v_i - \dot{d}_i \quad (19)$$

where  $d_i$  is the grid point displacement in the  $i$ th direction, and overdots ( $\cdot$ ) represents the time rate of change of a quantity. Modifying equation 16, the result is the stabilized weak form of the incompressible Navier-Stokes equations in an ALE reference frame:

$$R^v = \int_{\Omega^f} \left( \delta v_i \rho^f \left( \frac{\partial v_i}{\partial t} + \hat{v}_j \frac{\partial v_i}{\partial x_j} \right) + \frac{\partial \delta v_i}{\partial x_j} \sigma_{ij}^f \right) d\Omega - \int_{\Gamma^f} \delta v_i \sigma_{ij}^f \hat{n}_j^f d\Omega \\ + \sum_{n_{elem}} \int_{\Omega^f} \eta_i^{PG} \left( \rho^f \left( \frac{\partial v_i}{\partial t} + \hat{v}_j \frac{\partial v_i}{\partial x_j} \right) - \frac{\partial \sigma_{ij}^f}{\partial x_j} \right) d\Omega \quad (20)$$

$$\eta_i^{PG} = \hat{v}_j \frac{\partial \delta v_i}{\partial x_j} \tau_{SUPG} + \frac{1}{\rho^f} \frac{\partial \delta p}{\partial x_j} \tau_{PSPG} \quad (21)$$

Noting the presence of the new *differential* velocity in the Petrov-Galerkin test function  $\eta_i^{PG}$ .

#### 2.4.1. Time Integration with the ALE method

Since the fluid mesh moves with time, the issue arises of building the residual with mesh coordinates at n, n+1, or an intermediate configuration. [12] gives a method to time average four intermediate snapshots from n to n+1 which greatly improves accuracy of the scheme, but also increases computational cost. Instead of computing once the residual (internal force) and consistent tangent, for each time step, they are computed at four planes. Then a total residual for that time step

is function of the four intermediate residuals accompanied by weighting values:

$$R^{fluid} = \sum_{k=1}^4 R_k \alpha_k \quad (22)$$

$$J^{fluid} = \sum_{k=1}^4 J_k \alpha_k \quad (23)$$

$$\alpha_1 = \alpha_2 = \frac{3}{4} \quad \alpha_3 = \alpha_4 = -\frac{1}{2}$$

where k is intermediate plane between n and n+1. Next, the mesh velocity is calculated specifically for each plane as:

$$\dot{d}_j^{(k)} = \frac{\theta_k^{n+1} d_j^{n+1} + \theta_k^n d_j^n + \theta_k^{n-1} d_j^{n-1}}{\Delta t} \quad (24)$$

where theta has the value:

$$\theta_1^{n+1} = \theta_2^{n+1} = 1 \quad \theta_3^{n+1} = \theta_4^{n+1} = 0 \quad (25)$$

$$\theta_1^n = \theta_2^n = -1 \quad \theta_3^n = \theta_4^n = 1$$

$$\theta_1^{n-1} = \theta_2^{n-1} = 0 \quad \theta_3^{n-1} = \theta_4^{n-1} = -1$$

Substituting the values for  $\theta_k$  into (24) reveals a Forward Euler scheme for the first two steps, and a Backward Euler scheme in the second two steps of the mesh motion. This stencil is only applicable to the 2nd order BDF time integration scheme, that is also a three point stencil.

#### 2.4.2. Auxiliary Mesh Motion Elastic Field

A static, linear elastic field is employed for the mesh grid points to keep the mesh from tangling, and to smooth the displacements. This approach allows for a second set of equations that can be integrated in the standard assembly loop for the ALE fluid problem:

$$\frac{\partial \sigma_{ij}^m}{\partial x_j} = 0 \quad (26)$$

$$\sigma_{ij}^m = C_{ijkl}^m \epsilon_{kl}^m \quad (27)$$

$$\epsilon_{ij}^m = \frac{1}{2} \left( \frac{\partial d_i}{\partial x_j} + \frac{\partial d_j}{\partial x_i} \right) \quad (28)$$

where  $\sigma_{ij}^m$  and  $C_{ijkl}^m$  are the mesh stress tensor, and constitutive tensor. After the assumptions of angular momentum, isotropy, symmetric tensor, and a pure compressibility (Poisson's ratio is zero),  $C_{ijkl}^m$  reduces to a second order tensor with the elastic modulus ( $E^m$ ) along the diagonal. Given these simplifications and inspecting equation 26, one can conclude the elastic modulus has bearing on the physics of the problem, it only needs to be non-zero. The mesh only feels stress from itself, internally, and exerts no reaction force to fluid flow, or structural coupling. Given in a Galerkin Finite Element context, the weak form of the elastic mesh field is:

$$R^d = \int_{\Gamma_f} \delta d_i \sigma_{ij}^m \hat{n}_j^f d\Gamma - \int_{\Omega^f} \frac{\partial \delta d_i}{\partial x_j} \sigma_{ij}^m d\Omega = 0 \quad (29)$$

$V_\infty$	20.0 $\frac{m}{s}$	Inflow Horizontal Velocity
$\mu^f$	0.001 $\frac{kg}{ms}$	Fluid Dynamic Viscosity
$\rho^f$	1.0 $\frac{kg}{m^3}$	Fluid Density
$L_c$	2.11727e-4 m	Airfoil Chord Length

Table 1: Parameters for the pitching NACA001 airfoil problem.

#### 2.4.3. Numerical Example: Pitching NACA 0012 Airfoil

To verify the ALE implementation a NACA0012 air foil's angle of attack is pitched between 0 and 20 degrees using two methods: 1) varying inflow direction at boundary, and 2) holding inflow direction constant, and prescribing radial movement of the mesh points around the airfoil. This problem was modeled after the compressible counterpart from [13], which was originally taken from [14]. 85400 degrees of freedom (fluid plus mesh displacement), a time step of  $dt = 0.01$  s. The remaining relevant problem parameters are given in table 1.

Due to the low Reynolds (**Re=4.23**) number of the flow, the flow is steady. The pressure, velocity, and mesh are zero angle of attack are given in figure 8, and again at angle of attack of 20 degrees in figure 9.

The Lift evolution for the ALE reference frame in figure 10 shows good agreement with the Eulerian simulation, see figure 10.

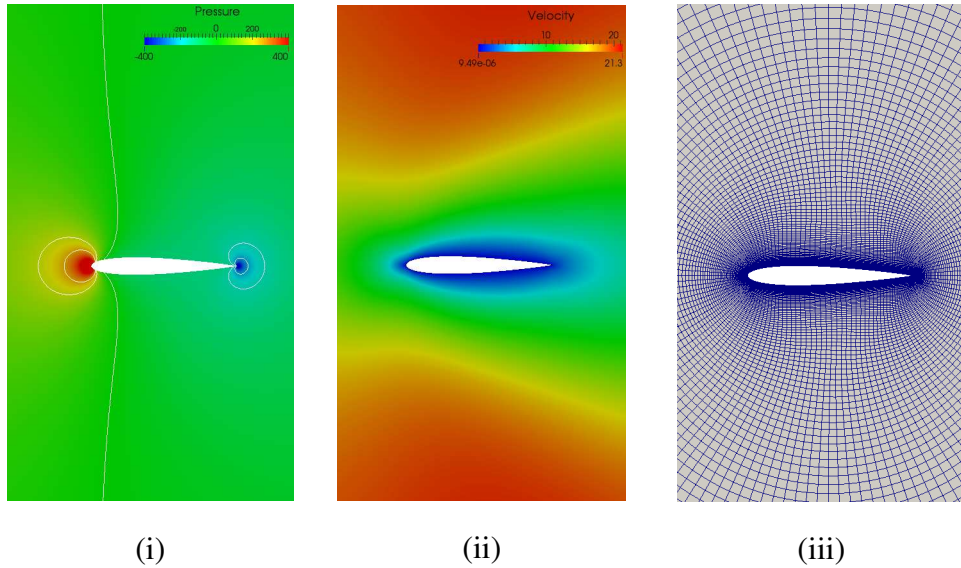


Figure 8: 0 degree Angle of Attack:(i) Pressure. (ii) Velocity Norm. (iii) Mesh.

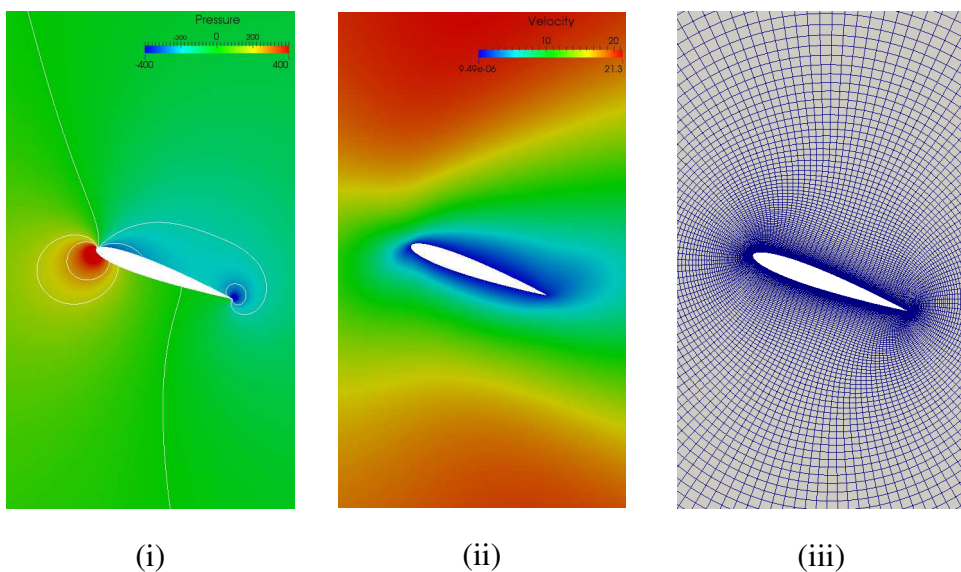


Figure 9: 20 degree Angle of Attack: (i) Pressure. (ii) Velocity Norm. (iii) Mesh.

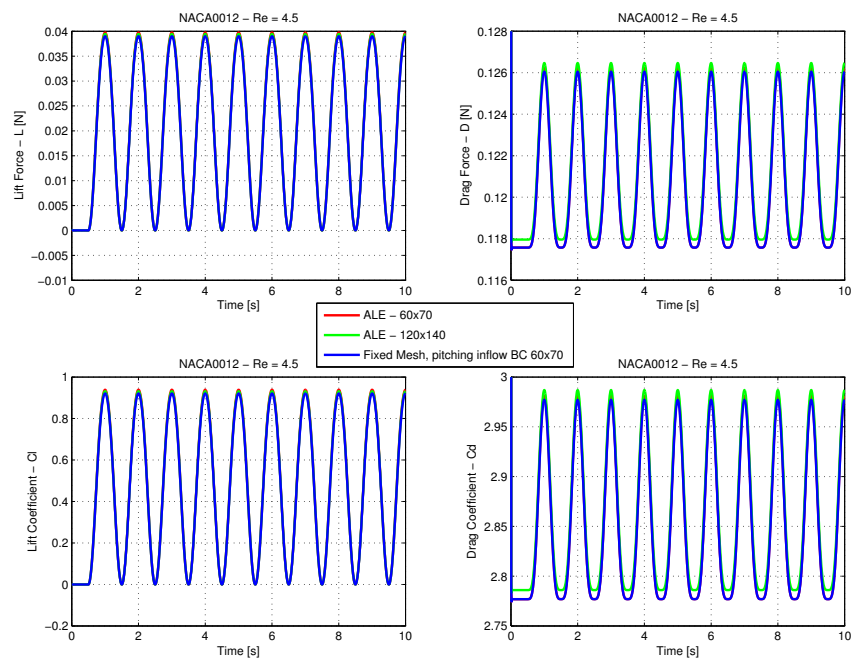


Figure 10: Pitching NACA0012 Airfoil Lift ALE Comparison.

## 2.5. Elasticity

Transient structural mechanics, in the absence of damping and external loading, are governed by the elastodynamic equation:

$$\rho^s \frac{\partial^2 u_j}{\partial t^2} = \frac{\partial \sigma_{ij}^s}{\partial x_i} \quad (30)$$

where  $\rho^s$  is the structural density,  $u_i$  is the solid displacement in the  $i$ th direction, and  $\sigma_{ij}^s$  is the structural Cauchy stress tensor. The stress tensor here is general to any linear or nonlinear material constitutive relationship. Just as with the fluid equations, Equation 30 is a conservation of momentum, or Newton's second law, per unit volume (giving the unit of force per unit volume).

Equation 30 is called the elastodynamic due to the inclusion of the left hand side, the acceleration (inertial) term. Elastostatics consist of only the divergence of the structural stress tensor equal to external loading. Equation 30 is cast into Galerkin Finite Element formulation by multiplying the residual equation by a weighting function, and integrating each differential volume  $d\Omega^s$  over the domain  $\Omega^s$ :

$$R^u = \int_{\Omega^s} \delta u_j \left( \rho^s \frac{\partial^2 u_j}{\partial t^2} - \frac{\partial \sigma_{ij}^s}{\partial x_i} \right) d\Omega \quad (31)$$

Here  $\delta u_j$  is the kinematically admissible displacement (test function), leaving equation 31 as energy norm, known as the Principal of Virtual Work. The stress tensor is separated from the rest of the equation. Integration by parts and the Divergence Theorem are both applied, to allow for a convenient boundary traction enforcement.

$$\int_{\Omega^s} \delta u_j \frac{\partial \sigma_{ij}^s}{\partial x_i} d\Omega = \int_{\Gamma^s} \sigma_{ij}^s \delta u_j \hat{n}_i^s d\Gamma - \int_{\Omega^s} \sigma_{ij}^s \frac{\partial \delta u_j}{\partial x_i} d\Omega \quad (32)$$

Resulting in a total structural residual

$$R^u = \int_{\Omega} \left( \delta u_j \rho^s \frac{\partial^2 u_j}{\partial t^2} + \sigma_{ij}^s \frac{\partial \delta u_j}{\partial x_i} \right) d\Omega \quad (33)$$

$$- \int_{\Gamma^s} \sigma_{ij}^s \delta u_j \hat{n}_i^s d\Gamma \quad (34)$$

### 2.5.1. Material Models

#### 2.5.2. Linear Elastic Model

The constitutive equation for linear elasticity (Hooke's Law) is:

$$\sigma_{ij} = D_{ijkl} \epsilon_{kl}^s \quad (35)$$

where  $D_{ijkl}$  is a fourth order tensor that is reduced to the Lamè parameters by way of conservation of angular momentum (stress tensor is symmetric), tensorial symmetry, and material isotropy. The Lamè are related to the elastic modulus ( $E^s$ ) and Poisson's ratio ( $\nu^s$ ).  $\epsilon_{ij}^s$  is the structural strain tensor:

$$\epsilon_{ij}^s = \frac{1}{2} \left( \frac{\partial u_i}{\partial x_j} + \frac{\partial u_j}{\partial x_i} \right) \quad (36)$$

#### 2.5.3. St. Venant Kirchhoff Model

The structural stress tensor can also be a nonlinear function of the displacement  $u_i$ . Here the concept of hyperelasticity is introduced. The theory and implementation was taken directly from [15]. The only nonlinear structural model used in the results shown here is the St. Venant Kirchhoff finite strain model. The structural configuration is mapped back to the reference configuration by computing the 2cd Piola-Kirchhoff stress tensor  $S_{ij}$ . Then computing the Cauchy stress tensor  $\sigma_{ij}^s$  is simply:

$$P_{ij} = F_{ij} S_{ij} \quad (37)$$

$$\sigma_{ij}^s = J^{-1} P F_{ij}^T \quad (38)$$

Where  $P_{ij}$  is the nominal stress tensor. Given the structural displacement solution at the current step (Newton step)  $u_i$ , a displacement gradient  $F$  is computed:

$$F = \frac{\partial x_i^{n+1}}{\partial X_j} \quad (39)$$

$$x_i^{n+1} = x_i^n + u_i^{n+1}$$

where  $x_i^n$  are the undeformed coordinates. Next the determinant of the deformation gradient and the right Cauchy-Green deformation tensor are computed:

$$J = \det(F_{ij}) \quad (40)$$

$$C_{ij} = F^{ji} F_{ij} \quad (41)$$

Continuing with a compressible formulation, the 2cd Piola-Kirchhoff stress tensor is computed:

$$S = \frac{\partial \Psi}{\partial C_{ij}} \quad (42)$$

Where for a St. Venant-Kirchhoff model:

$$\Psi(E_{ij}) = \frac{\mu^s}{4} (C_{ij} C_{ji} - 2C_{ii} + 3) + \frac{\lambda^s}{8} (C_{ii} - 3)^2 \quad (43)$$

where  $\lambda^s$  is Lamè's first parameter. Leading to the 2cd PK2 stress tensor:

$$S_{ij} = \mu^s (C_{ij} - \delta_{ij}) + \frac{\lambda^s}{2} (C_{kk} - 3) \delta_{ij} \quad (44)$$

Refer to [15] for results and verification against the literature.

#### 2.5.4. Structural Time Integration

The generalized- $\alpha$  method given in [16] is employed here for time integration of the structural system where  $\alpha_f = \alpha_m = 0$  which leads to unconditional stability. Good numerical dissipation of high frequencies is achieved with the choice of the values:

$$\gamma = \frac{1}{2}$$

$$\beta = \frac{1}{4}$$

Time integration of the full fluid-structure system is discussed later.

#### 2.6. Monolithic Fluid-Structure Interaction via Residual Coupling Scheme

The global system of equations is assembled for fluid, fluid mesh, and structure, and is in general non-linear. On each time step, the system of equations is linearized and the global residual norm is incremented to zero with Newton's Method. To this end, all Jacobian terms (gradient of residuals with respect to state variables) must be built to correctly approximate the tangent used in the iterative algorithm. Symbolically the total residual  $R$  and Jacobian  $J$  are:

$$R(p, v_i, d_i, u_i) = \begin{bmatrix} R^p \\ R^v \\ R^d \\ R^u \end{bmatrix} \quad (45)$$

$$J(p, v_i, d_i, u_i) = \begin{bmatrix} \frac{\partial R^p}{\partial p} & \frac{\partial R^p}{\partial v_i} & \frac{\partial R^p}{\partial d_i} & \frac{\partial R^p}{\partial u_i} \\ \frac{\partial R^v}{\partial p} & \frac{\partial R^v}{\partial v_i} & \frac{\partial R^v}{\partial d_i} & \frac{\partial R^v}{\partial u_i} \\ \frac{\partial R^d}{\partial p} & \frac{\partial R^d}{\partial v_i} & \frac{\partial R^d}{\partial d_i} & \frac{\partial R^d}{\partial u_i} \\ \frac{\partial R^u}{\partial p} & \frac{\partial R^u}{\partial v_i} & \frac{\partial R^u}{\partial d_i} & \frac{\partial R^u}{\partial u_i} \end{bmatrix} \quad (46)$$

To couple the fluid and structure, continuity of: traction, velocity, and displacement, must be enforced. This is enforced in the weak sense:

$$\int_{\Gamma^{fsi}} \left( \sigma_{ij}^f \hat{n}_j^f - \sigma_{ij}^s \hat{n}_j^s \right) d\Gamma \quad (47)$$

$$\int_{\Gamma^{fsi}} (v_i - \dot{u}_i) d\Gamma \quad (48)$$

$$\int_{\Gamma^{fsi}} (u_i - d_i) d\Gamma \quad (49)$$

A *residual based coupling* scheme developed by Howard and Bova [13], [17] is implemented here for coupling the fluid and structure. The advantage of this scheme is that there is no need for Lagrange multipliers (multiple point constraints), allowing us to retain the original linear system size. Taking advantage of the boundary integrals from both fluid (equation 15) and structure (equation 34) continuity of traction is enforced. By not computing a boundary integral for either fluid or structure at the fluid-structure interface, and replacing the residual terms as given below, continuity with 2cd order accuracy is achieved[17]:

$$R^{fsi}(p, v_i, d_i, u_i) = \begin{bmatrix} R^p \\ R^v \\ R^d \\ R^u \end{bmatrix} \rightarrow \begin{bmatrix} R^p \\ \int_{\Gamma^{fsi}} (v_i - \dot{u}_i) d\Gamma \\ \int_{\Gamma^{fsi}} (u_i - d_i) d\Gamma \\ R^v + R^u \end{bmatrix} \quad (50)$$

Equation 50 couples the continuity by taking advantage of the fact that the residual vector is driven to zero in the Newton solver, therefore the boundary term is equal to the volume term. By not computing the boundary term, and summing the remaining volumetric terms for fluid and structure, the two boundary terms become equal (weakly). The remaining two coupling conditions enforce the continuity in velocity of fluid and structure, and displacement in fluid mesh and structure.

Note here, a hybrid time solver method is employed. The fluid equations are integrated with the 2nd order BDF scheme, while the structural equations are integrated with the generalized- $\alpha$  method. This is done building a total Jacobian  $J$  that has structural 2nd order, 1st order, and static entries multiplied by the appropriate generalized- $\alpha$  parameters. Then the fluid entries for the 1st order and static jacobians are multiplied by the appropriate BDF-2 parameters and summed into the total jacobian. [13].

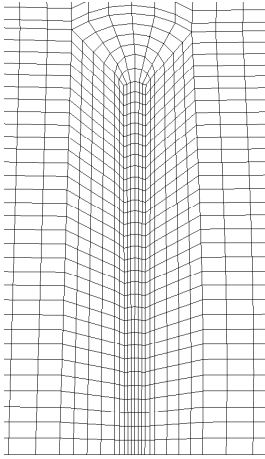


Figure 11: Computational mesh used for the stationary FSI beam problem.

### 2.6.1. Numerical Example: Stationary Beam in Fluid Channel

A structural beam is immersed in a parabolic channel, in a benchmark taken from COMSOL MultiPhysics [18], except here only the steady state solution is of interest. The channel is 100 [ $\mu\text{m}$ ] high, 300 [ $\mu\text{m}$ ] wide, and a 47.5 [ $\mu\text{m}$ ] tall beam with a 2.5 [ $\mu\text{m}$ ] radius circular top. The left structural interface is placed at 100 [ $\mu\text{m}$ ] from the inflow boundary. The fluid density  $\rho^f$  is 1000  $\frac{\text{kg}}{\text{m}^3}$ , and the dynamic viscosity  $\mu^f$  is 0.001  $\frac{\text{kg}}{\text{ms}}$ . The inflow is parabolic with a mean velocity  $\bar{v} = 0.0333 \frac{\text{m}}{\text{s}}$ , and given the beam height, the Reynolds number of the flow is **Re=1.5**. The structural density  $\rho^s$  is 7850  $\frac{\text{kg}}{\text{m}^3}$  (although does not matter for a stationary problem), Elastic modulus  $E^s$  is 2.0e5 Pa, and Poisson's ratio is 0.33. The top and bottom walls are no-slip, and the outlet is traction free ( $\sigma_{ij}^f \hat{n}_j^\Gamma = 0$ ). The residual was converged in one time step ( $dt = 1000\text{s}$ ) from 6.079896516e-04 to 4.354672628e-11 in 5 newton steps.

A close-up of the beam section of the grid is given in figure 11, and the pressure and velocity norm contours are given in figure 12. The horizontal structural

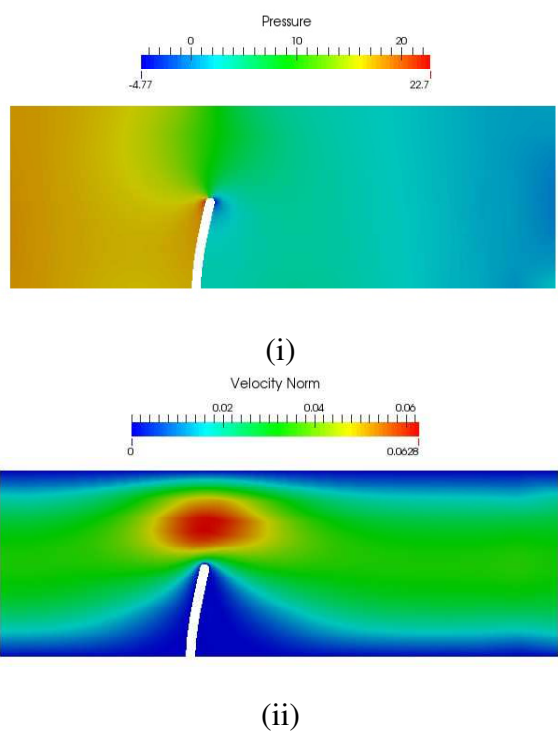


Figure 12: FSI Beam (i) Pressure solution. (ii) Velocity norm solution.

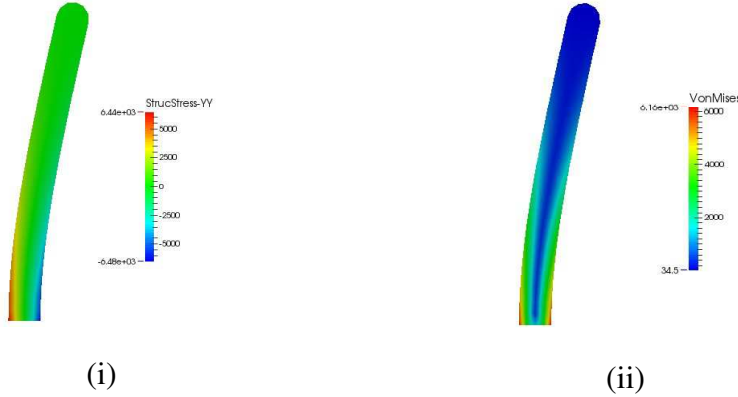


Figure 13: FSI Beam (i) Volumetric stress in y-direction. (ii) von Mises stress.

displacement (and mesh displacement) at the top beam node is **7.9492E-06**, which is in good agreement with the COMSOL benchmark [18]. The structural volumetric stress in the y-direction, and the von Mises stress are given in Figure 13.

### 2.6.2. Numerical Example: Transient Cylinder-Flag structure in Fluid Channel

The well-known FSI benchmark proposed by Turek, et al. [19] is computed for the 2cd FSI (FSI-2) test case. The fluid Reynolds number is **Re=100**, resulting in an unsteady fluid-structure response. The channel is 0.41 m high, 2.5 m wide, and has no-slip top and bottom boundaries. The inflow is parabolic, and linearly ramped up with time a mean velocity  $\bar{v}_{in} = 1.0 \frac{m}{s}$  in one second. The outlet is traction free( $\sigma_{ij}^f \hat{n}_j^\Gamma = 0$ ), and the cylinder center is at (x=0.2 m,y=0.2 m), with a radius of 0.1 m. The flag extends from the cylinder edge at 0.25 to 0.6 m, giving a flag length of 0.35 m in the x-direction. The flag thickness in the y-direction is 0.02 m. The fluid density  $\rho^f$  is  $1000 \frac{kg}{m^3}$  and dynamic viscosity  $\mu^f$  is  $0.001 \frac{kg}{ms}$ . The structural density is  $10000 \frac{kg}{m^3}$ , the elastic modulus  $E^s$  is  $1.4e6 Pa$ , and Poisson's ratio is 0.4.

The structure is modeled by a hyperelastic St. Venant-Kirchhoff constitutive model. The simulation is ran for 35 seconds, at a time step of 0.001, where in each time step the global residual norm is converged by at least 4 orders of magnitude. The mesh resolution is 2553 points in the fluid, and 144 structural points. Figure 14 shows the pressure, velocity, mesh, and von Mises stress, all in the deformed configuration at the final time.

The plots for vertical displacement, horizontal displacement at the flag tip were extracted from [19], and the results from this work were **overlaid in red**, given in figure 15.

From figure 15 one can see that the displacement amplitude in the y-direction is slightly smaller than the benchmark results, yet the frequency looks pretty close. Further, the x-displacement appears to exhibit a second mode, which is not seen in the benchmark results.

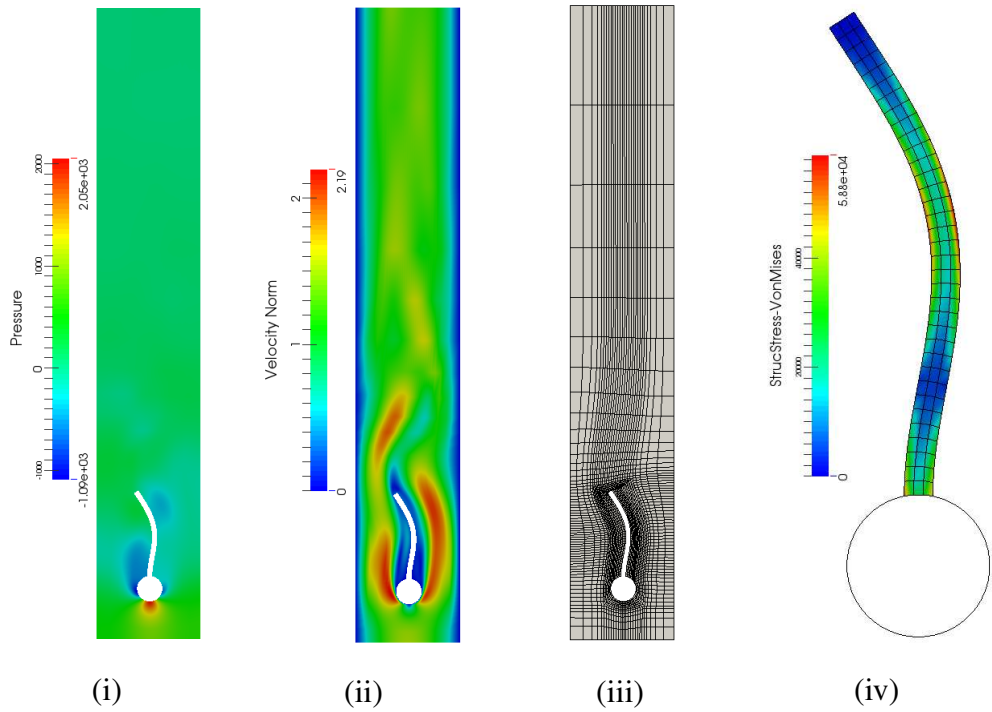


Figure 14: Transient FSI cylinder-flag (i) Pressure contours. (ii) Velocity norm contours. (iii) Fluid Mesh. (iv) Structure with von Mises stress contours.

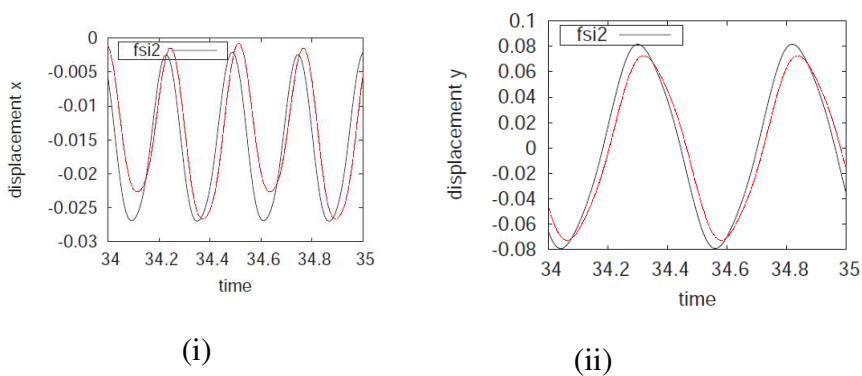


Figure 15: Transient FSI cylinder-flag (i) Horizontal displacement of flag tip overlayed in red with benchmark results. (ii) Vertical displacement of flag tip overlayed in red with benchmark results.

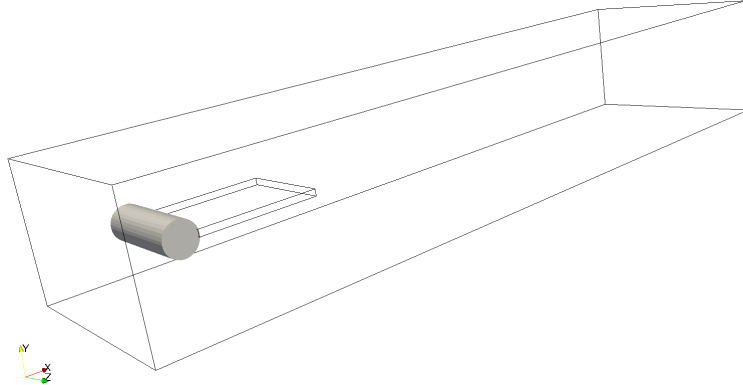


Figure 16: 3D cylinder-flag geometry

### 2.6.3. Numerical Example: Transient Cylinder-Flag structure in 3D Fluid Channel

This example is a three-dimensional analog to the previous cylinder-flag problem. The channel is 2.5 m long in the x direction, 0.41 m tall in the y-direction, and 0.65 thick in the z-direction. The geometry is given in figure 16.

The cylinder is radius 0.1, the flag x length is 0.35 from the cylinder edge, as in the 2D problem. The width of the cylinder and flag in the z-direction are 0.35 m. The inflow condition is parabolic in both y and z directions, with a peak (centerline) velocity of  $3.0 \frac{m}{s}$ . All walls are no-slip. With the exception of the elastic modulus  $E^s = 5.6e6$  and the structural density  $\rho^s = 1000 \frac{kg}{m^3}$ , all of the material properties are the same as in section 2.6.2. 37816 fluid nodes and 2421 structural nodes are used in the simulation. The cylinder+flag mesh from x,y, and z planes are in figure 17.

The simulation was run for 10 seconds. The dynamic response is most apparent just after 1.0 second (see figure 18 for velocity and displacement images) until 2.0 seconds. Some asymmetric effects are observed (see figure 19) just after 2.0

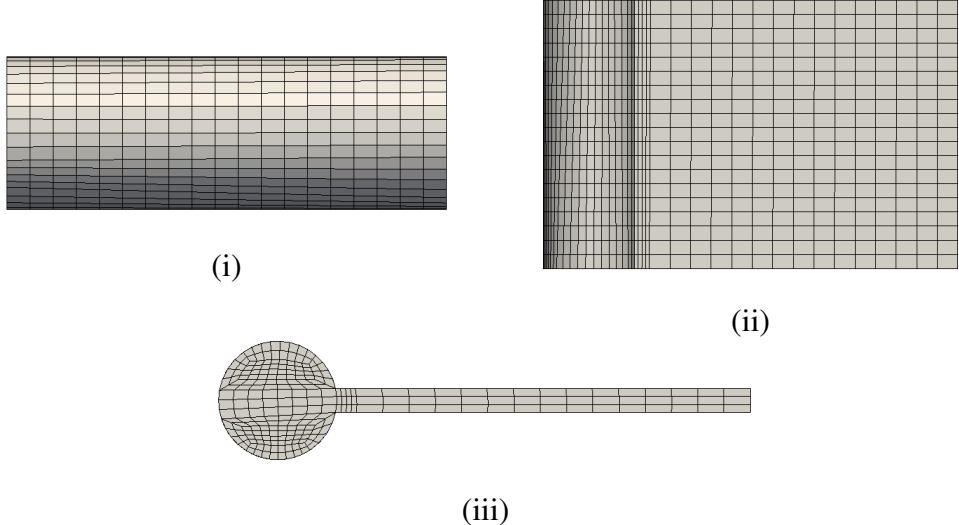


Figure 17: 3D FSI Cylinder-Flag (i) yz-plane mesh. (ii) xz-plane mesh. (iii) xy-plane mesh.

seconds. Then the response mostly damps out to relatively small (displacement ; order 1.0e3 m) displacements of the structure. The pressure is given in figure 20 just after 2.0 seconds.

This problem was run on 32 cpu cores for about 36 hours, using the iterative linear solver GMRES, and an incomplete lower-upper decomposition preconditioner. Further verification of this example is intended in the future. A full-steady state response, and lift/drag profile will be calculated.

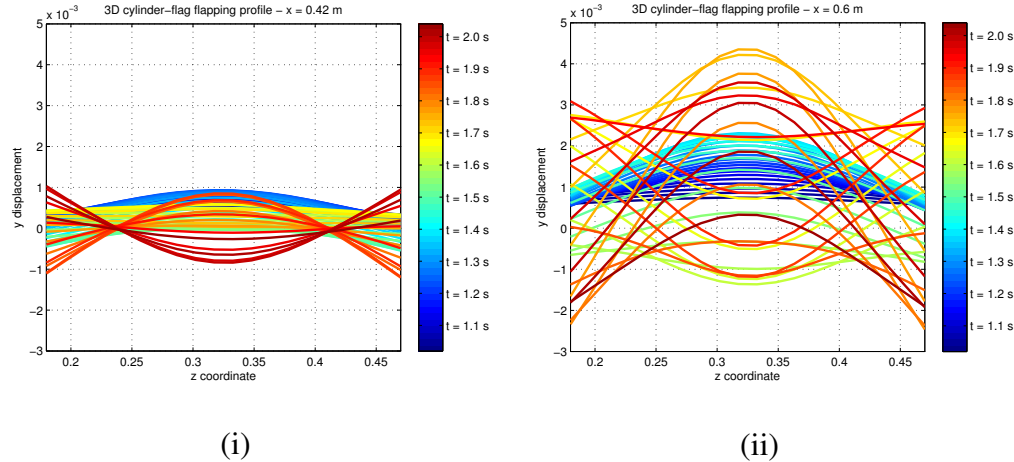


Figure 18: 3D FSI Cylinder-Flag (i) y-displacement at  $x=0.32$  m. (ii) -displacement at  $x=0.6$  m (rear edge of flag).

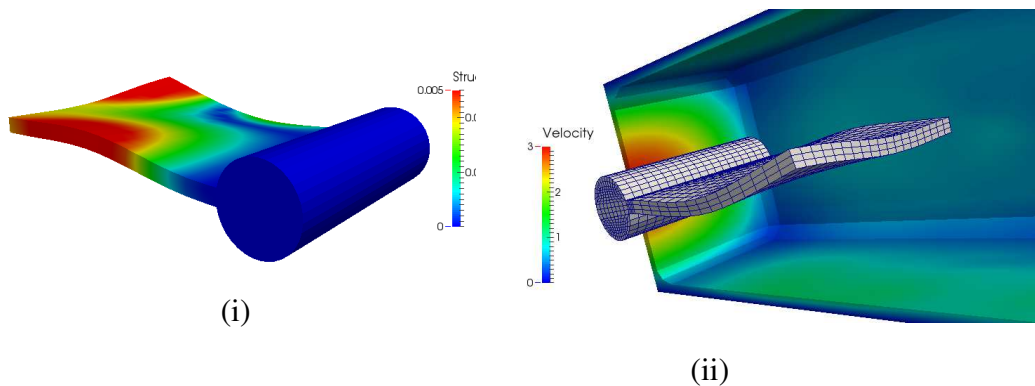


Figure 19: 3D FSI Cylinder-Flag (i) Structural displacement. (ii) Fluid velocity and structural displacement.

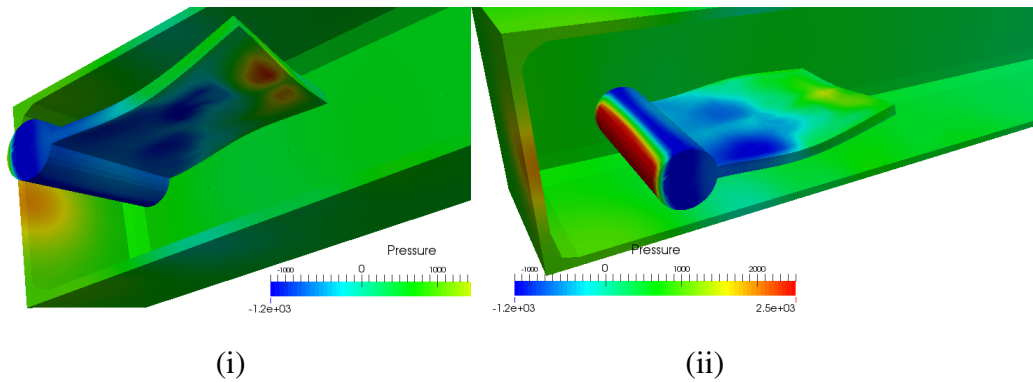


Figure 20: 3D FSI Cylinder-Flag fluid pressure on FSI interface. (i) Fluid pressure on FSI interface.

## *2.7. Computer Programming and Utilities*

In this section I discuss some of the utilities, programs, and computational tools that were used to implement and obtain the results shown here.

### *2.7.1. Code Development*

The code is implemented in C++, allowing for much faster memory allocation, and in turn much faster simulations, compared to a tool like Matlab. C++ is flexible, and permits the utmost modularity, when used correctly. The code is developed with OpenMPI to allow for parallel computing on a decomposed computational mesh. The free code development environment Eclipse is used to develop, and debug simulations.

### *2.7.2. Pre-Processing*

Pre-processing, such as mesh generation, is completed using an Academic Licensed version of Cubit, developed at Sandia National Labs. More complex mesh generation warrants a more powerful tool, such as ICEM CFD, which is part of the ANSYS suite. The exodus / genesis database format for the mesh is employed. Python scripting was also a powerful tool for writing and submitting large sweeps of simulations for parametric studies, for example.

### *2.7.3. Post-Processing*

The free visualization program Paraview was used to visualize and post-process solution files. As well as Matlab for plotting, and observing trends.

### *2.7.4. Linear Solvers and Preconditioners*

All two-dimensional problems employ a direct solver (UMFPACK), and all three-dimensional problems use the iterative solver GMRES with ILUT pre-conditioner

method. These solvers and pre-conditioners are all part of the the TRILINOS package compiled at Sandia National Laboratory [20]. Trilinos provides MPI tools, compilers, mesh database utilities, load balancing scripts, solvers, pre-conditioners, and more.

### 2.8. Global Optimization and Sensitivity Analysis

Computational optimization is concerned with employing sophisticated numerical methods to find the best possible problem geometry to minimize an inverse performance measure (minimizing inverse of performance, maximizes performance). Formally the problem is posed as:

$$\begin{aligned} & \underset{\mathbf{s}}{\text{minimize}} \quad z(\mathbf{s}, \mathbf{f}(\mathbf{s})) \\ & \text{subject to} \left\{ \begin{array}{l} h_i(\mathbf{s}, \mathbf{f}(\mathbf{s})) = 0 \\ g_i(\mathbf{s}, \mathbf{f}(\mathbf{s})) \leq 0 \\ \mathbf{R}(\mathbf{s}, \mathbf{f}(\mathbf{s})) = \mathbf{0} \\ \mathbf{s} \in S_i \end{array} \right. \end{aligned}$$

Where  $z$  is the objective function to be minimized,  $\mathbf{s}$  is the vector of design variables,  $\mathbf{f}$  is the vector of state variables,  $h_i$  are the equality constraints, and  $g_i$  are the inequality constraints.  $S_i$  is the set of values the design variables  $\mathbf{s}$  can take, and  $\mathbf{R}$  is the global residual vector of the governing equations. Since it is possible to compute analytical gradients of the partial differential equations, gradient based optimization schemes only are included. Analytical derivatives must be computed due to the nature of the topology optimization, using numerical derivatives (finite difference) would extremely computationally inefficient. Some common gradient based algorithms to solve the optimization problem are: interior point

method, sequential quadratic programming, and the Method of Moving Asymptotes (MMA). Here a modified version of the MMA algorithm is utilized, namely the Globally Convergent Method of Moving Asymptotes (GCMMA). Both MMA and GCMMA were developed by Svanberg [21].

Converting the constrained optimization problem (above) into an unconstrained, minimization problem, the Lagrange functional is built:

$$\mathcal{L}(\mathbf{s}, \mathbf{f}(\mathbf{s}), \alpha_i, \omega_j) = z(\mathbf{s}, \mathbf{f}(\mathbf{s})) + \sum_{i=1}^{n_h} \alpha_i h_i(\mathbf{s}, \mathbf{f}(\mathbf{s})) + \sum_{j=1}^{n_g} \omega_j g_j(\mathbf{s}, \mathbf{f}(\mathbf{s})) \quad (51)$$

where  $n_h$  and  $n_g$  are the numbers of equality and inequality constraints, respectively. Here, the equality and inequality constraints have been converted to penalties by Lagrange multipliers  $\alpha_i$  and  $\omega_j$ . If the optimal value of a variable is denoted by giving it a superscript  $(\cdot)^*$ , then the Lagrange has some interesting properties [22]:

- $\mathcal{L}(\mathbf{s}^*, \mathbf{f}(\mathbf{s}^*), \alpha_i^*, \omega_j^*) = z(\mathbf{s}^*)$
- $\mathcal{L}(\mathbf{s}^*, \mathbf{f}(\mathbf{s}^*), \alpha_i, \omega_j) \leq \mathcal{L}(\mathbf{s}^*, \mathbf{f}(\mathbf{s}^*), \alpha_i^*, \omega_i^*) \leq \mathcal{L}(\mathbf{s}, \mathbf{f}(\mathbf{s}), \alpha_i^*, \omega_j^*)$

→ This shows us that the solution to the Lagrangian is a saddle point.

Next, the Karush-Kuhn-Tucker (KKT) optimality conditions are derived by taking the gradient of equation 51:

The first optimality condition is:

$$\begin{aligned} & \frac{\partial \mathcal{L}(\mathbf{s}^*, \mathbf{f}(\mathbf{s}^*), \alpha_i^*, \omega_j^*)}{\partial \mathbf{s}} = 0 \\ \rightarrow & \frac{\partial z(\mathbf{s}, \mathbf{f}(\mathbf{s}))}{\partial s_k} + \sum_{i=1}^{n_h} \alpha_i \frac{\partial h_i(\mathbf{s}, \mathbf{f}(\mathbf{s}))}{\partial s_k} + \sum_{j=1}^{n_g} \omega_j \frac{\partial g_j(\mathbf{s}, \mathbf{f}(\mathbf{s}))}{\partial s_k} = 0 \quad (52) \end{aligned}$$

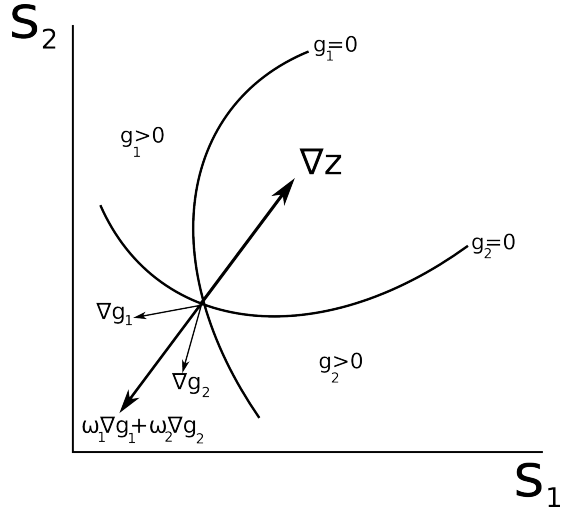


Figure 21: Illustration of optimality point in a two dimensional design space.

This condition is illustrated graphically in figure 21 for a two design variable, two inequality constraint problem. Note the equal and opposite vectors of gradient of the objective function, and the inequality constraints multiplied by the penalty values (Lagrange multipliers). The second optimality condition is:

$$\begin{aligned} \frac{\partial \mathcal{L}(\mathbf{s}^*, \mathbf{f}(\mathbf{s}^*), \alpha_i^*, \omega_j^*)}{\partial \alpha_i} &= 0 \\ \rightarrow h_i(\mathbf{s}^*, \mathbf{f}(\mathbf{s}^*)) &= 0 \quad \text{for all } i = 1, \dots, n_h \end{aligned} \quad (53)$$

The third optimality condition is:

$$\begin{aligned} \frac{\partial \mathcal{L}(\mathbf{s}^*, \mathbf{f}(\mathbf{s}^*), \alpha_i^*, \omega_j^*)}{\partial \omega_j} &= 0 \\ \rightarrow \omega_j g_j(\mathbf{s}^*, \mathbf{f}(\mathbf{s}^*)) &= 0 \quad \text{for all active } j = 1, \dots, n_g \end{aligned} \quad (54)$$

### 2.8.1. Sensitivity Analysis

The optimization algorithm searches given the sensitivity of the criteria (objective or constraint) with respect to the design variables  $\mathbf{s}$ . Employing the chain rule, the criteria sensitivity is:

$$\frac{dQ}{ds} = \underbrace{\frac{\partial Q}{\partial s}}_{\text{explicit}} + \underbrace{\left( \frac{\partial Q}{\partial f} \right)^T \frac{\partial f}{\partial s}}_{\text{implicit}} \quad (55)$$

$\frac{\partial f}{\partial s}$  is computed with:

$$\frac{dR}{ds} = \frac{\partial R}{\partial s} + \frac{\partial R}{\partial f} \frac{\partial f}{\partial s} = 0 \quad (56)$$

$$\rightarrow \frac{\partial f}{\partial s} = - \left( \frac{\partial R}{\partial f} \right)^{-1} \frac{\partial R}{\partial s} \quad (57)$$

Recognizing that  $\frac{\partial R}{\partial f}$  is the consistent tangent (Jacobian of residual vector with respect to state vector) in our Newton linearization scheme:

$$\frac{\partial R}{\partial f} = J \quad (58)$$

Substituting equation 57 into equation 55:

$$\frac{dQ}{ds} = \frac{\partial Q}{\partial s} - \left( \frac{\partial Q}{\partial f} \right)^T J^{-1} \frac{\partial R}{\partial s} \quad (59)$$

$$(60)$$

Finally, either the *direct* or the *adjoint* method is chosen:

$$\text{Direct} \begin{cases} \frac{d\bar{Q}}{d\bar{\mathbf{s}}} = \frac{\partial Q}{\partial \mathbf{s}} - \left( \frac{\partial Q}{\partial \bar{\mathbf{f}}} \right)^T \boldsymbol{\kappa} \\ \mathbf{J}\boldsymbol{\kappa} = \frac{\partial \bar{\mathbf{R}}}{\partial \bar{\mathbf{s}}} \end{cases} \quad (61)$$

$$\text{Adjoint} \begin{cases} \frac{d\bar{Q}}{d\bar{\mathbf{s}}} = \frac{\partial Q}{\partial \mathbf{s}} - \boldsymbol{\lambda}^T \frac{\partial \bar{\mathbf{R}}}{\partial \bar{\mathbf{s}}} \\ \mathbf{J}^T \boldsymbol{\lambda} = \frac{\partial Q}{\partial \bar{\mathbf{f}}} \end{cases} \quad (62)$$

Given the right hand sides for adjoint and direct linear solves, one can see that the direct method requires  $n_s$  linear solves, where the adjoint method requires as many linear solves as there are criteria (one for objective +  $n_g + n_h$ ). Therefore, if  $1 + n_g + n_h > n_s$ , then the direct method is faster, otherwise, the adjoint method is the better choice [23].

### **3. Summary of *The Level Set and Extended Finite Element Methods for Topology Optimization of Fluid-Structure Interaction Problems*.**

This study introduces the Level Set and extended Finite Element methods for topology optimization of fluid-structure interaction problems. The methods presented thus far, monolithic ALE incompressible-fluid structure interaction, are employed in a design optimization framework. The monolithic approach is desirable from the sensitivity analysis standpoint, because the entire FSI problem can be treated as one nonlinear system. Whereas employing a staggered or partitioned FSI solver, leads to a more cumbersome calculation of the sensitivities.

Density based (velocity penalization) approaches require a highly refined mesh to resolve fine details in the material geometry, and they can exhibit fuzzy or jagged material boundaries in topology optimization applications. In the context of fluid-structure interaction, the computational expense is already high. We introduce a new approach that can resolve fine, crisp boundaries even on a relatively coarse mesh. Furthermore, when extending to three dimensions, the density approaches begin to break down even further. The Level Set and XFEM methods perform quite well in three dimensions, and yield better performing designs. The LSM-XFEM methods do not converge as well as the density methods, because of the limited sensitivity information of the Level Set field. Density methods have a non-zero sensitivity value at every element in the design domain, whereas Level Set methods only provide sensitivity where there are non-zero gradients, which in proximity to the zero-contour. However, we do present numerical methods to expand the zone of influence via smoothing and regularization.

The fluid-structure problem is solved on a body fitted mesh, and the internal structural topology is optimized ensuring a *skin* along the structural FSI interface.

For density methods this means constraining the elemental density to be at the upper bound, and for Level Set methods, this means ensuring no intersected elements in the volume elements along the FSI boundary. The limitation here is that FSI boundary is not optimized. This framework is applicable for a specific set of applications where the outside shape is fixed, and one desires to optimize the topology, which in turns affects both the structural and fluid deformation profile.

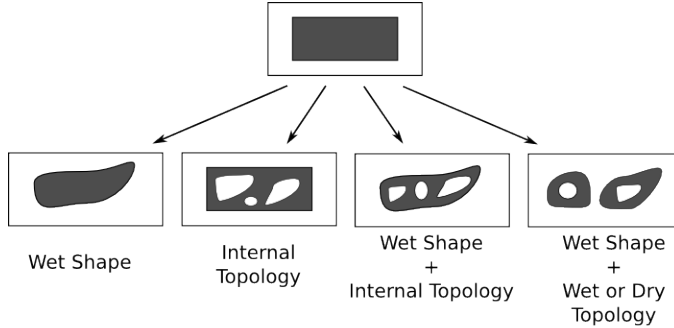


Figure 22: AeroElastic Optimization Schemes

#### 4. Generalized Lagrangian XFEM for Fluid-Structure Interaction

The extended finite element method (XFEM) has emerged as a powerful tool for analysis and optimization of multiphysics systems. The XFEM naturally accommodates complex boundaries within one unified finite element framework. In the field of computational design optimization, the XFEM, in conjunction with a Level Set (LSM) field to designate the location of the material boundary, has been shown to yield excellent results for both structural and fluidic systems [24],[25]. XFEM takes advantage of the level set description and approximates the physical field without the need for uniformly fine mesh, as is the case with density methods. This characteristic becomes increasingly important as real-world, transient, three-dimensional fluid-structure systems are optimized. In the context of fluid-structure interaction (FSI), these benefits have been demonstrated only recently.<sup>1</sup> The various types of design optimization schemes illustrated in Figure 22 range from a purely shape optimization, where the *wet shape* is optimized [26], to

---

<sup>1</sup>We presented *Topology Optimization of Fluid-Structure Interaction Problems using the Level Set and Extended Finite Element Methods* at the 10th World Congress on Structural and Multidisciplinary Optimization, May, 2013.

the more popular method of optimizing the internal topology, holding the fluid-structure interface constant. Note, there is an assortment of previous works depending on the fluid-structure interaction solver method (staggered, monolithic) and fluid-structure interface model (fixed [27], one-way coupled [28], two-way coupled<sup>1</sup>). The remaining two (right most illustrations) regimes of FSI optimization have been researched far less. Yoon [29] employed a porosity-velocity penalization approach to optimize FSI structures. However, velocity penalization methods can yield unphysical responses, and still suffer from the problems of high mesh resolution requirement and jagged or blurred material definitions.

In our previous study<sup>1</sup> an optimization approach where a structural member with internal topology described by a Level Set field and discretized with the XFEM, is immersed in a monolithic, incompressible ALE fluid-structure interaction solver was presented. The internal structure topology is optimized using the Level Set / extended finite element method. Seeking to further increase the generality of the optimization process for FSI problems, both the wet shape and the internal topology are optimized *simultaneously*. Our previous work operated on a body fitted mesh for the fluid-structure interface, and the design variables on the fluid-structure interface were constrained to ensure one layer of structural elements.

The method presented here is a generalization of this approach, by letting the Level Set iso-contour also govern the fluid-structure interface geometry in addition to the layout of the internal structure. The generalized method incorporates an ALE reference frame in the fluid and a Lagrangian reference frame in the struc-

ture. The internal structure 'void' phase is modeled as fluid, but since it is an isolated system, exerts no net force on the structure. Thus, the optimization of the Level Set field modifies only the fluid-structure interface, enabling both internal and external geometry manipulation.

Stabilized Lagrange multipliers are employed to enforce coupling conditions between fluid and structure: continuity of traction, velocity, and displacement. The coupling influences (tractions) are statically condensed out at the elemental-level leaving the original system size intact.

#### 4.1. The XFEM for Immersed Boundaries in Incompressible Flow

The XFEM enriches the trial solution space by enriching the interpolation functions, and the intersected cells are triangulated to integrate the equations accurately. For more details on the XFEM the reader is referred to Appendix A.. In the context of an Lagrangian structures, unless one of the phases is void, you have to constrain the materials to displace the same amount at the interface. Otherwise there is slipping, or penetration. With fluids, a similar idea is present, except the fluid is required to *see* the immersed boundary (of void, or structure, for example). Recall the stabilized weak form of the incompressible Navier-Stokes equations 16. The stabilized terms and the boundary term are omitted, and reprint the weak form of the momentum equation here:

$$R^v = \int_{\Omega^f} \left( \delta v_i \rho^f \left( \frac{\partial v_i}{\partial t} + v_j \frac{\partial v_i}{\partial x_j} \right) + \frac{\partial \delta v_i}{\partial x_j} \sigma_{ij}^f \right) d\Omega \quad (63)$$

Next, the weak form is augmented with stabilized Lagrange multiplier ( $\lambda_i$ ), with the associated test function  $\delta \lambda_i$  to enforce the velocity constraint on the interface  $\Gamma$ :

$$\begin{aligned} R^v = & \int_{\Omega^f} \left( \delta v_i \rho^f \left( \frac{\partial v_i}{\partial t} + v_j \frac{\partial v_i}{\partial x_j} \right) + \frac{\partial \delta v_i}{\partial x_j} \sigma_{ij}^f \right) d\Omega \\ & + \int_{\Gamma} \delta \lambda_i (v_i - \tilde{v}_i) d\Gamma - \int_{\Gamma} \delta v_i \lambda_i d\Gamma + k \int_{\Gamma} \delta \lambda_i (\lambda_i - \sigma_{ij}^f \hat{n}_j^f) d\Gamma \end{aligned} \quad (64)$$

where  $\tilde{v}_i$  is our prescribed velocity (zero for a stationary, no-slip wall), and  $k$  is scaling parameter. As  $k$  is increased, the Lagrange multiplier is stabilized further, resulting in a more benign linear system conditioning, yet a weaker enforcement of the penalty  $v_i - \tilde{v}_i$ . As  $k$  is decreased to zero, a standard Lagrange Multiplier formulation is achieved, and the linear system is further ill-conditioned, however, the constraint is enforced stronger.

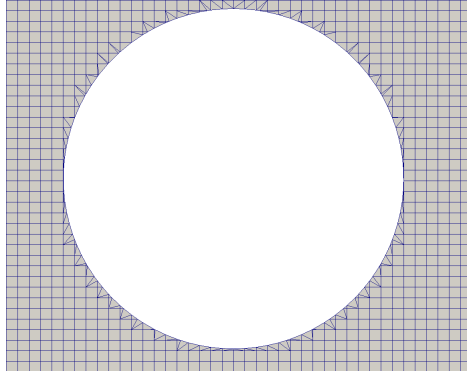


Figure 23: Zoomed view of the XFEM triangulated interface mesh for the cylinder.

#### 4.1.1. Numerical Example: Unsteady Flow about an immersed Cylinder

The test problem performed in section 2.3.1 using standard finite elements, is repeated here, using the Level Set/ XFEM with stabilized Lagrange multipliers to enforce the no-slip condition on the cylinder. The mesh used has 10862 grid points, and is shown in figure 23 and figure 24.

The velocity and pressure contours are given in figure ??, and the aerodynamic quantities in figure 25.

The LSM-XFEM reproduces the orginal benchmark results [10] very well. The results are slightly different than the body fitted configuration, due to a phase shift apparent in the results in figure 25. Although at the steady state, the phase shift goes to zero, and the two curves line up. This is most likely due to a small interface error (velocity is not exactly zero at interface), and could be studied by varying the interface scaling parameter  $k$  in equation 64. Here the study was run with a  $k$  of 0.001, divided by the interface line length of the intersected element:

$$k = \frac{0.001}{d\Gamma} \quad (65)$$

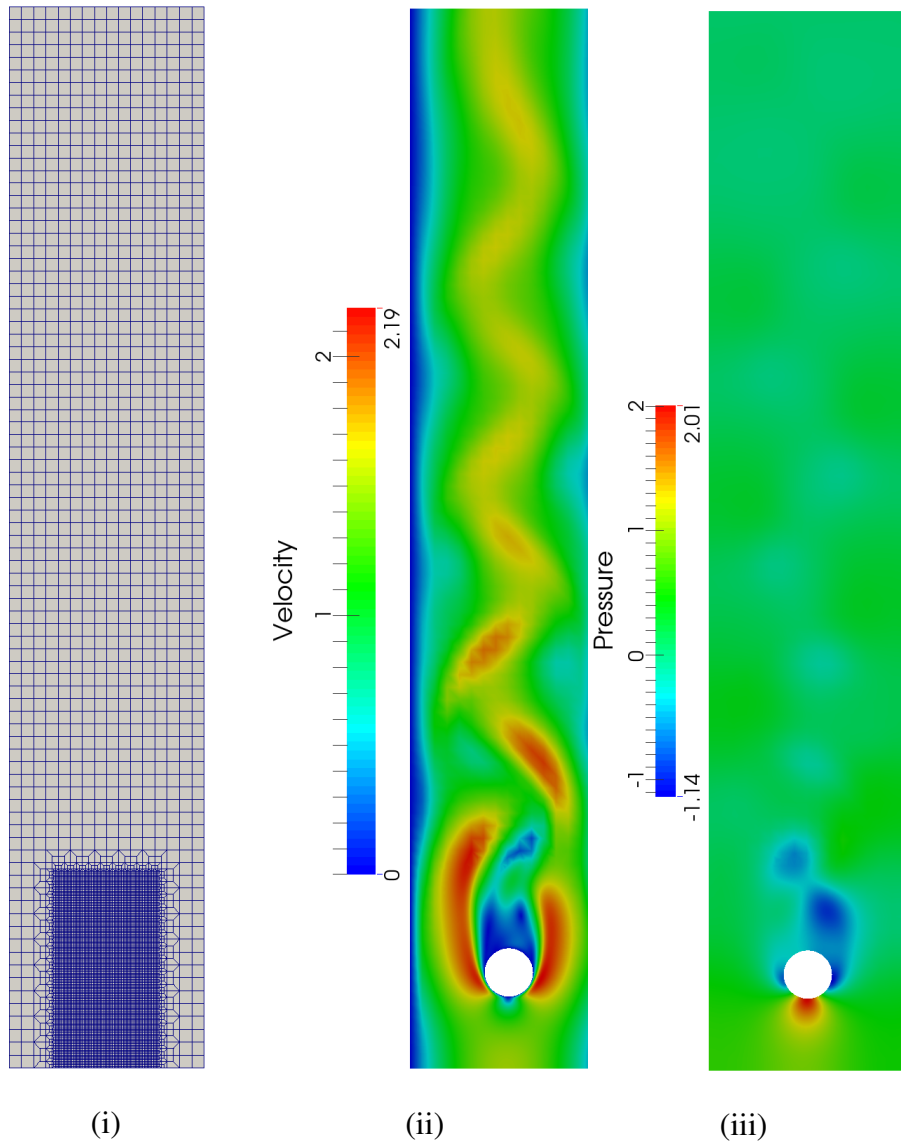


Figure 24: Unsteady cylinder flow (i) Un-intersected fixed grid mesh. (ii) Velocity contours. (iii) Pressure contours.

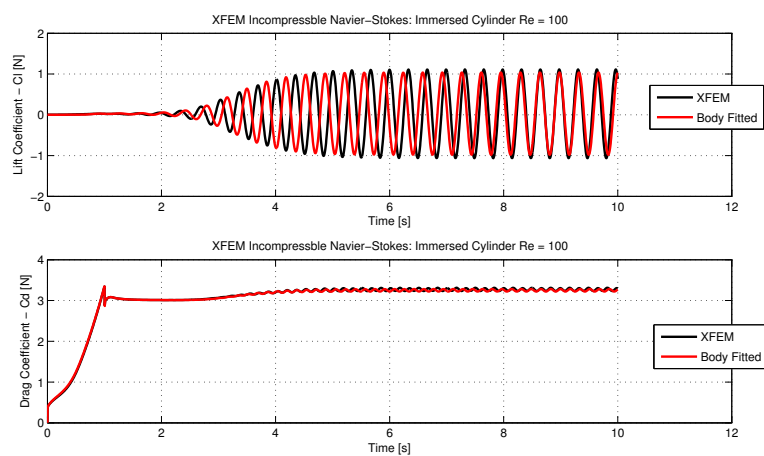


Figure 25: Aerodynamic Coefficients for the Body Fitted and LSM-XFEM for the unsteady cylinder benchmark.

#### 4.2. Stabilized Lagrange Multipliers for Fluid-Structure Coupling

Proceeding with the FSI analysis, the incompressible Navier-Stokes equations are solved on a moving grid using the LSM-XFEM method. Further, instead of void, a structural material is inserted for the second phase. The Level Set zero-contour will represent the interface between the fluid and structure. The only remaining piece is to implement the necessary interface constraints to enforce two-way coupling between the two materials.

A stabilized Lagrange multiplier formulation is presented for coupling of the fluid and structure without a body fitted mesh. The complete weak form of the coupled, stabilized, ALE fluid-structure equations are:

$$\begin{aligned}
R = & \int_{\Omega^f} \left( \delta v_i \rho^f \left( \frac{\partial v_i}{\partial t} + \hat{v}_j \frac{\partial v_i}{\partial x_j} \right) + \frac{\partial \delta v_i}{\partial x_j} \sigma_{ij}^f \right) d\Omega - \int_{\Gamma^f} \delta v_i \sigma_{ij}^f \hat{n}_j^f d\Gamma \\
& + \sum_{n_{elem}} \int_{\Omega^f} \eta_i^{PG} \left( \rho^f \left( \frac{\partial v_i}{\partial t} + \hat{v}_j \frac{\partial v_i}{\partial x_j} \right) - \frac{\partial \sigma_{ij}^f}{\partial x_j} \right) d\Omega - \int_{\Omega^f} \frac{\partial \delta d_i}{\partial x_j} \sigma_{ij}^m d\Omega \\
& \quad + \int_{\Omega^f} \delta p \frac{\partial v_i}{\partial x_i} d\Omega + \int_{\Omega} \left( \delta u_j \rho^s \frac{\partial^2 u_j}{\partial t^2} + \sigma_{ij}^s \frac{\partial \delta u_j}{\partial x_i} \right) d\Omega \\
& - \int_{\Gamma^s} \sigma_{ij}^s \delta u_j \hat{n}_i^s d\Gamma + k_{disp} \int_{\Gamma} \delta \lambda_i (d_i - u_i) d\Gamma + k_{vel} \int_{\Gamma} \delta \gamma_i (\dot{u}_i - v_i) d\Gamma \\
& \quad - \int_{\Gamma} \delta d_i \lambda_i d\Gamma - \int_{\Gamma} (\delta u_i - \delta v_i) \gamma_i d\Gamma \\
& + \int_{\Gamma} \delta \lambda_i \left( \lambda_i - \sigma_{ij}^m \hat{n}_j^f \right) d\Gamma + \int_{\Gamma} \delta \gamma_i \left( \gamma_i - \bar{\sigma}_{ij} \hat{n}_j^s \right) d\Gamma \quad (66)
\end{aligned}$$

where  $\eta^{PG}$  is given in equation 20. Note the boundary terms for the structure and fluid mesh fields have been omitted. Again,  $v_i$  is the fluid velocity,  $u_i$  is the structural displacement,  $d_i$  is the fluid mesh displacement.  $\bar{\sigma}_{ij}$  is the *mean stress* at the interface, given by:

$$\bar{\sigma}_{ij} = \frac{1}{2} \left( \sigma_{ij}^f + \sigma_{ij}^s \right) \quad (67)$$

$k_{disp}$  and  $k_{vel}$  are scaling penalty parameters. The language multipliers  $\lambda_i$  and  $\gamma_i$  are solved for on the element level, and the residuals are augmented with the values:

$$R^d = - \int \delta d_i \lambda_i d\Gamma \quad (68)$$

$$R^v = \int \delta v_i \gamma_i d\Gamma \quad (69)$$

$$R^s = - \int \delta u_i \gamma_i d\Gamma \quad (70)$$

Note  $\lambda_i$  is a function of  $d_i$  and  $u_i$ , and  $\gamma_i$  a function of  $u_i$ ,  $\dot{u}_i$ ,  $v_i$ ,  $d_i$ , and  $p$  (fluid mechanical pressure). The consistent tangent must account for the addition of these traction forces to the residuals. Each static Jacobian  $\mathbf{K}$  and 1st order Jacobian  $\mathbf{C}$  is shown here:

$$K_{d,d} = \frac{\partial R^d}{\partial d_j} = - \int \delta d_i \frac{\partial \lambda_i}{\partial d_j} d\Gamma \quad (71)$$

$$\frac{\partial \lambda_i}{\partial d_k} = - \frac{1}{\int \delta \lambda_i d\Gamma} \left( \int \delta \lambda_k d\Gamma + \int \delta \lambda_i \frac{\partial \sigma_{ij}^m}{\partial d_k} \hat{n}_j d\Gamma \right) \quad (72)$$

$$K_{d,u} = \frac{\partial R^d}{\partial u_j} = - \int \delta d_i \frac{\partial \lambda_i}{\partial u_j} d\Gamma \quad (73)$$

$$\frac{\partial \lambda_i}{\partial u_k} = - \frac{1}{\int \delta \lambda_i d\Gamma} \left( \int \delta \lambda_k d\Gamma \right) \quad (74)$$

$$K_{u,u} = \frac{\partial R^u}{\partial u_j} = - \int \delta u_i \frac{\partial \gamma_i}{\partial u_j} d\Gamma \quad (75)$$

$$\frac{\partial \gamma_i}{\partial u_k} = - \frac{1}{\int \delta \gamma_i d\Gamma} \left( \int \delta \gamma_i \frac{\partial \bar{\sigma}_{ij}}{\partial u_k} \hat{n}_j d\Gamma \right) \quad (76)$$

$$\frac{\partial \bar{\sigma}_{ij}}{\partial u_k} = \frac{1}{2} \frac{\partial \sigma_{ij}^s}{\partial u_k} = \frac{1}{2} D_{im} B_{mj} \quad (77)$$

$$C_{u,u} = \frac{\partial R^u}{\partial \dot{u}_j} = - \int \delta u_i \frac{\partial \gamma_i}{\partial \dot{u}_j} d\Gamma \quad (78)$$

$$\frac{\partial \gamma_i}{\partial \dot{u}_k} = - \frac{1}{\int \delta \gamma_i d\Gamma} \left( \int \delta \gamma_k d\Gamma \right) \quad (79)$$

$$K_{u,v} = \frac{\partial R^u}{\partial v_j} = - \int \delta u_i \frac{\partial \gamma_i}{\partial v_j} d\Gamma \quad (80)$$

$$K_{v,v} = \frac{\partial R^v}{\partial v_j} = - \int \delta v_i \frac{\partial \gamma_i}{\partial v_j} d\Gamma \quad (81)$$

$$\frac{\partial \gamma_i}{\partial v_k} = - \frac{1}{\int \delta \gamma_i d\Gamma} \left( - \int \delta \gamma_i d\Gamma - \int \delta \gamma_i \frac{\partial \bar{\sigma}_{ij}}{\partial v_k} \hat{n}_j d\Gamma \right) \quad (82)$$

$$K_{v,p} = \frac{\partial R^v}{\partial p} = - \int \delta v_i \frac{\partial \gamma_i}{\partial p} d\Gamma \quad (83)$$

$$\frac{\partial \gamma_i}{\partial p} = - \frac{1}{\int \delta \gamma_i d\Gamma} \left( - \int \delta \gamma_i d\Gamma - \int \delta \gamma_i \frac{\partial \bar{\sigma}_{ij}}{\partial p} \hat{n}_j d\Gamma \right) \quad (84)$$

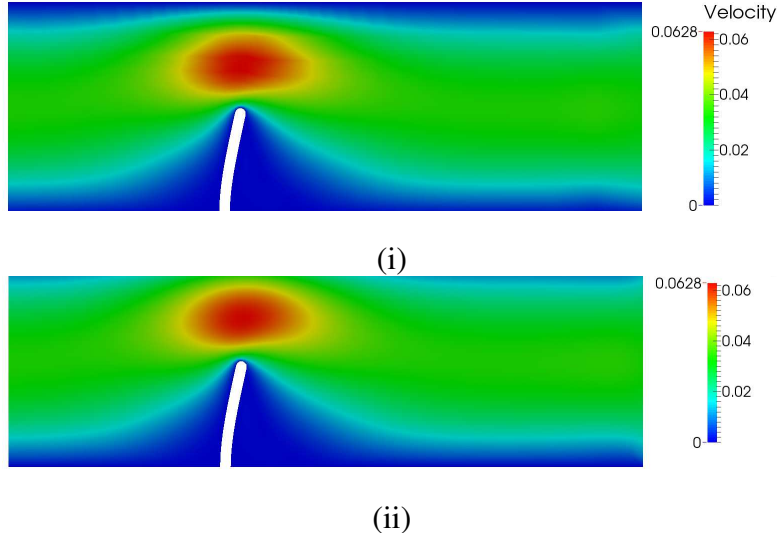


Figure 26: LSM-XFEM FSI Beam (i) Body Fitted Solution. (ii) LSM-XFEM with Stab. Lagrange Multipliers solution.

#### 4.2.1. Numerical Examples: Stationary FSI using LSM-XFEM

The FSI benchmark problem completed in section 2.6.1 is repeated here using the new generalized ALE LSM-XFEM method with stabilized Lagrange Multipliers. The velocity contours are shown for both body fitted (top image) and LSM-XFEM with stabilized Lagrange multipliers (lower image) in figure 26.

The solutions are very close, qualitatively. The global L2 error between the two solutions, is **0.00344**. Figure 27 shows the structural solution from the LSM-XFEM simulation plotted inside the fluid mesh displacement solution from the body fitted solution. Figure 28 shows a mesh resolution sweep together with a sweep of the velocity penalty parameter  $k_{vel}$  in equation 66.

There is little variation with respect to  $k_{vel}$ , given this example is stationary problem, this is to be expected, but the method shows good convergence with mesh refinement.

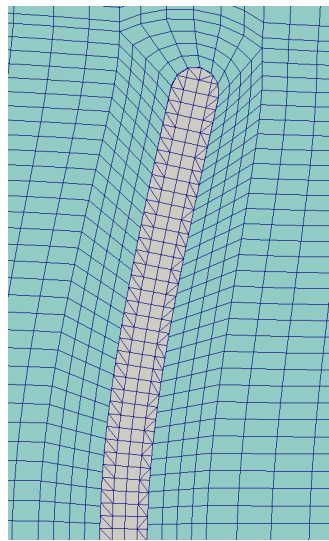


Figure 27: The LSM-XFEM structural solution plotted with the body fitted fluid solution.

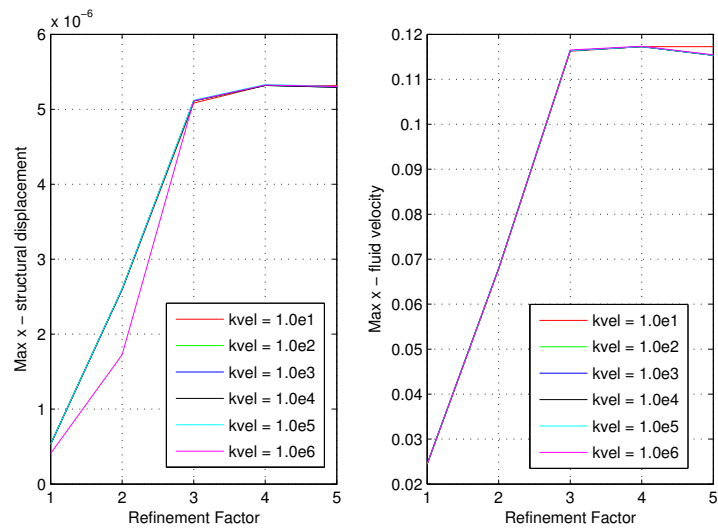


Figure 28: FSI Beam problem sweep for mesh resolutions and velocity penalty.

Variable	Lower Limit	Upper Limit	Step Size
$E^s$	1.0e2	1.0e12	1e4
$k_{disp}$	1.0e-2	1.0e12	1.0e2,1.0e4
$k_{vel}$	1.0e-2	1.0e12	1.0e2,1.0e4

Table 2: Sweep data for the generalized LSM-XFEM FSI cylinder problem.

To investigate further the penalty parameters  $k_{disp}$  and  $k_{vel}$  in equation 66, a structural cylinder in a parabolic channel flow is analyzed. This example uses the same dimensions as the previous 2D cylinder problem, except now a low Reynolds number of about 1.0 is modeled. The inflow is parabolic, with a mean velocity of 0.01  $\frac{m}{s}$ , the density  $\rho^f$  is 1000  $\frac{kg}{m^3}$ , and the dynamic viscosity is 1.0  $\frac{kg}{ms}$ . The structural Poisson's ratio is  $\nu^s = 0.33$ . Next the Elastic modulus  $E^s$ ,  $k_{disp}$ , and  $k_{vel}$  are swept over the following values given in table 3.

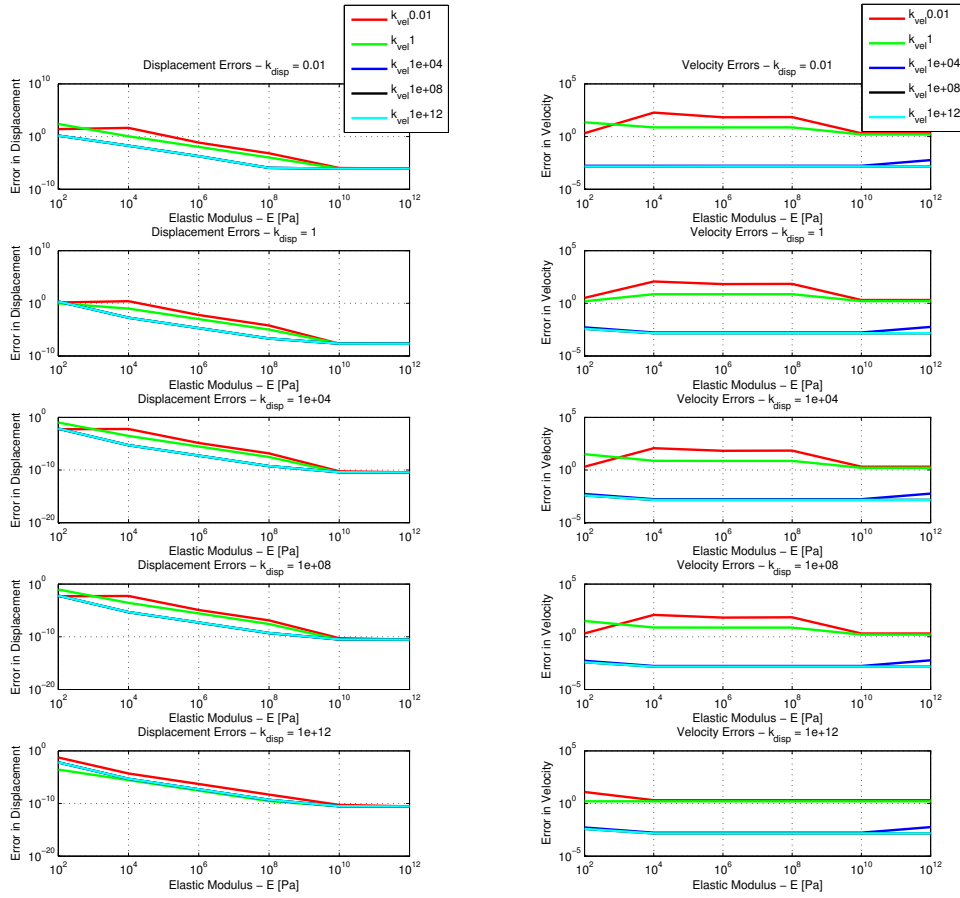
For each configuration, the interface error was calculated:

$$\text{error}_{disp} = \sqrt{(u_x - d_x)^2 + (u_y - d_y)^2} \quad (85)$$

$$\text{error}_{vel} = \sqrt{(v_x - \dot{u}_x)^2 + (v_y - \dot{u}_y)^2} \quad (86)$$

The interface errors for the sweep are given in figure 30.

Figure 30 shows excellent results for displacement for displacement parameters above **1.0e4**. The velocity error is minimized for velocity parameters above **1.0e4** as well, though the velocity error is not as low as desired even for a stationary problem. This particular issue is the subject of numerous works see [30], [31]. Further research will be dedicated to this issue with possibly looking to three Lagrange multiplier schemes for the interface, as well as Nitche type method [32],[33], [34].



(i)

(ii)

Figure 29: Stationary FSI cylinder sweep errors in (i) Displacement at interface. and (ii). Velocity at interface.

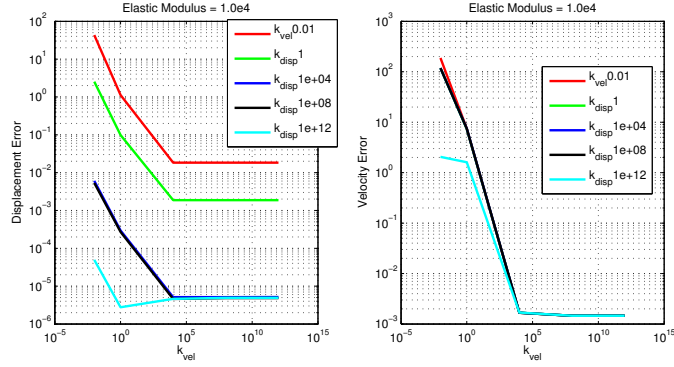


Figure 30: Stationary FSI cylinder sweep Elastic modulus  $1.0\text{e}4$  results for  $k_{vel}$  and  $k_{disp}$  sweep.

Next, various mesh resolutions and velocity scaling parameters are swept over. These results are illustrated in figure 31. Here, one can see that for scaling parameters **1.0e4** or above, there is a convergence, while smaller parameters diverge as the mesh is refined.

Finally, the global L2 error in horizontal fluid velocity is computed for each mesh resolution and velocity scaling parameter, given in Figure 32.

Again, a similar trend is seen where **1.0e4** and above give convergence.

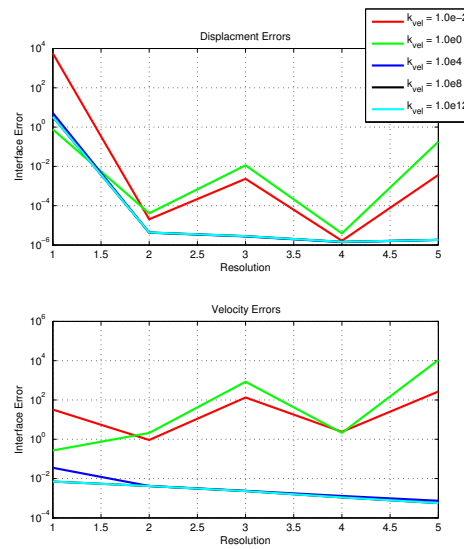


Figure 31: Stationary FSI cylinder resolution Sweep.

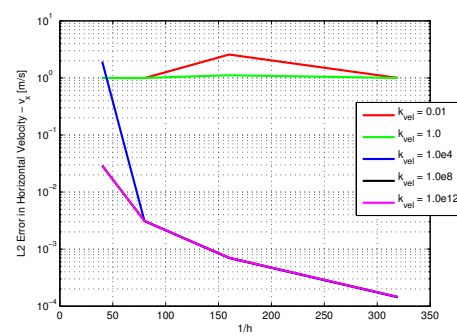


Figure 32: L2-errors in x-velocity for stationary FSI cylinder resolution Sweep.

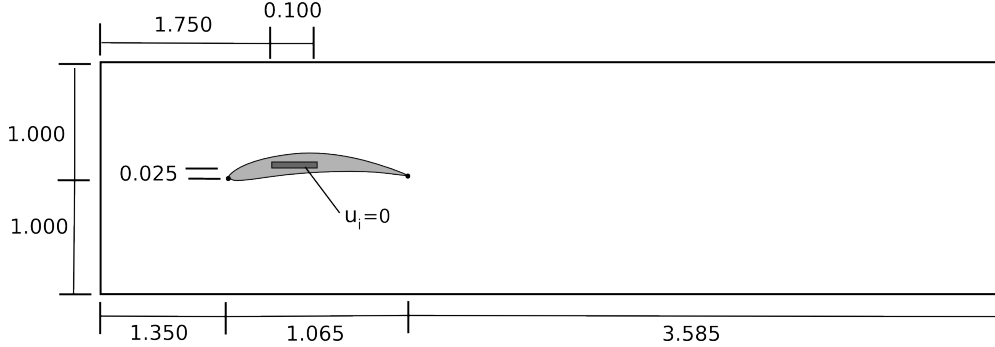


Figure 33: Problem setup for the FSI NACA 65 example. The line from the nose point to the bottom of the support region is 0.025

$\rho^f \left[ \frac{kg}{m^3} \right]$	$\mu^f \left[ \frac{kg}{ms} \right]$	$\bar{v}_{in} \left[ \frac{m}{s} \right]$	$L_c[m]$	$E^s[Pa]$	$\rho^s \left[ \frac{kg}{m^3} \right]$	$v^s[-]$	$dt[s]$	$T_f[s]$
1.0	0.0005	2.0	1.065	1.0e4	1000	0.33	0.001	10.0

Table 3: NACA 65 FSI Problem Setup parameters.

#### 4.2.2. Numerical Example: Deforming NACA 65 Airfoil in Channel Flow

Next, a NACA 65 airfoil fluid-structure response is simulated using the generalized LSM-XFEM method for fluid-structure interaction. The Reynolds number of the flow is **Re=4113.6**, using the chord length, **1.065 m**. The problem diagram is given in figure 33. The airfoil chord length is aligned with the flow (perfectly horizontal) in the undeformed configuration. The air foil is modeled by a hyperelastic St. Venant-Kirchhoff model. The entire problem (fluid+structure+fluid mesh) uses a generalized- $\alpha$  time integration scheme [16] with  $\rho = 0.25$  which determines all the values of the rest of the parameters. Figure 34 shows the velocity and pressure contours, and figure 35 gives the lifting and drag force evolutions.

As the contours and the aerodynamic forces show, the problem is highly nonlinear and transient. Further, the structural response is not intuitive as it deforms as a function of the pitching moment and the support boundary condition.

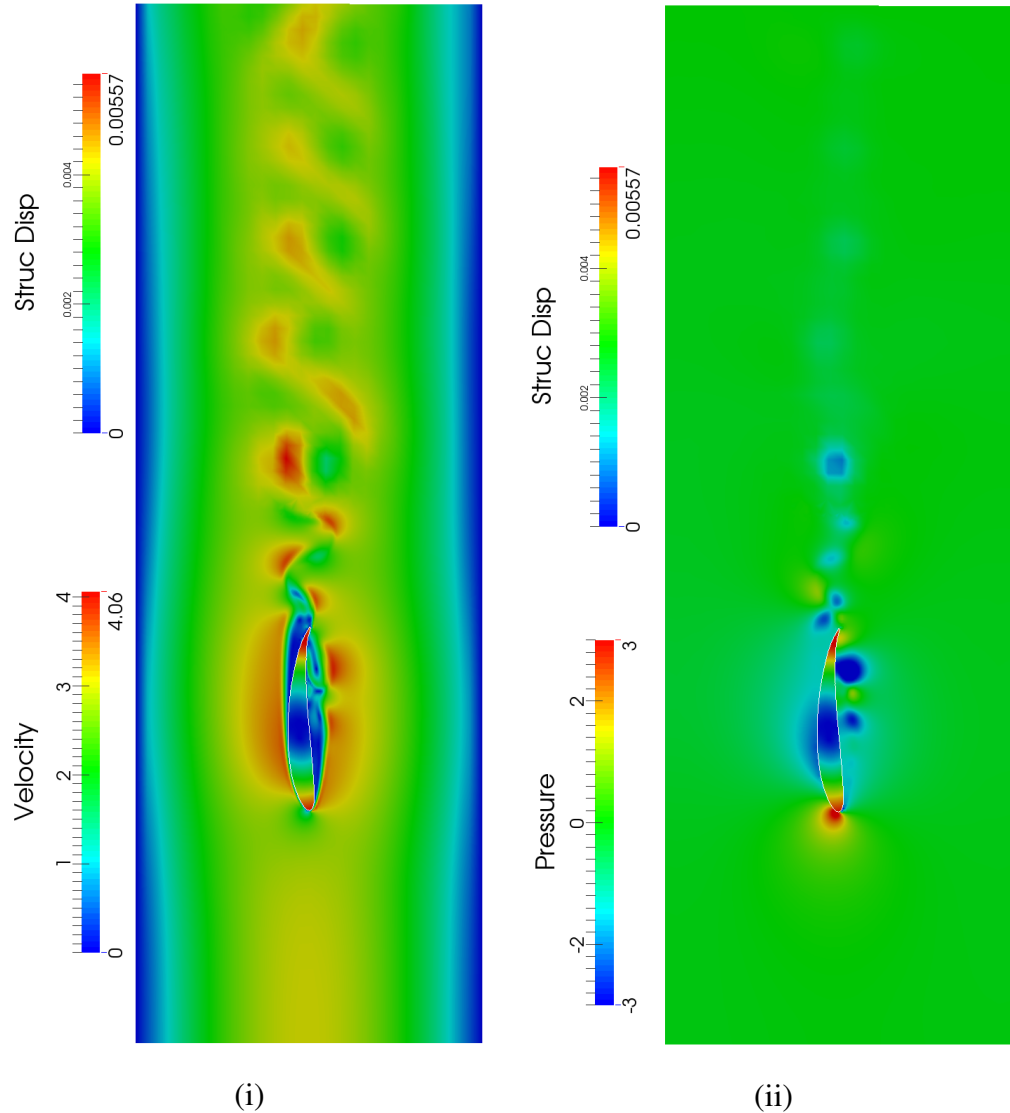


Figure 34: FSI NACA 65 Airfoil (i) Velocity contours. (ii). Pressure contours.

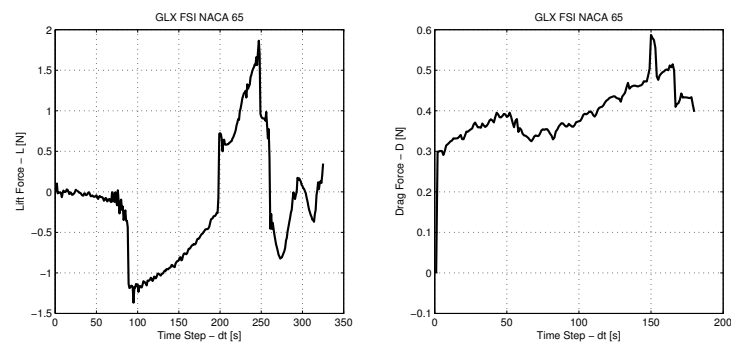


Figure 35: The Lift and Drag evolution for the NACA 65 FSI example.

#### *4.2.3. Numerical Example: Unsteady Cylinder-Flag Fluid-Structure Interaction*

The example from section 2.6.2 is completed using the LSM-XFEM method. Turek, et al's third FSI (FSI-3) case is simulated here, in contrast to section 2.6.2 where the FSI-2 case is repeated. The mean inflow velocity  $\bar{v}_x$  is  $2.0 \frac{m}{s}$ , the structural modulus  $E^s$  is  $5.6e6$ , and density  $\rho^s$  is  $1000 \frac{kg}{m^3}$ . The velocity, pressure, and deformed mesh geometries are illustrated in figure 36. The vertical tip displacement for the generalized method is overlaid **in red** with the benchmark result in figure 37.

Figure 37 shows even better results when compared to the body fitted method. It is intended to do further verification on the interface velocity and displacement error, however.

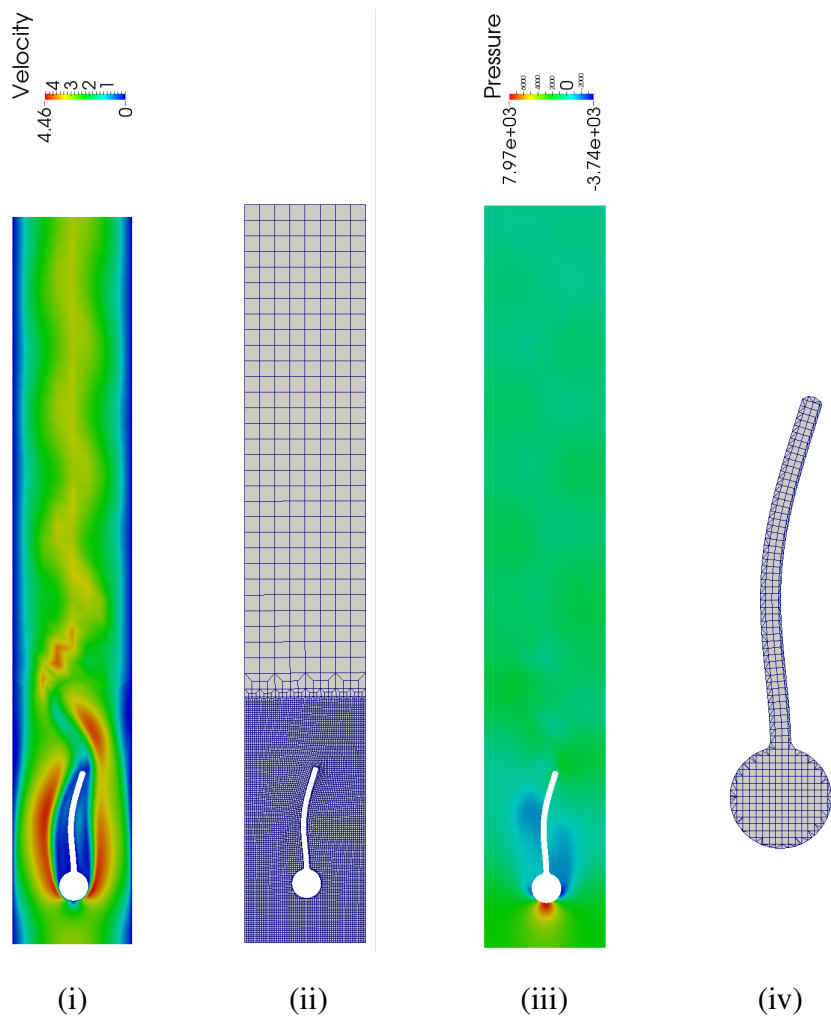


Figure 36: Transient FSI Cylinder-Flag Problem (i) Velocity contours. (ii) Deformed fluid mesh.  
(ii) Pressure contours. (iv) Deformed structural mesh.

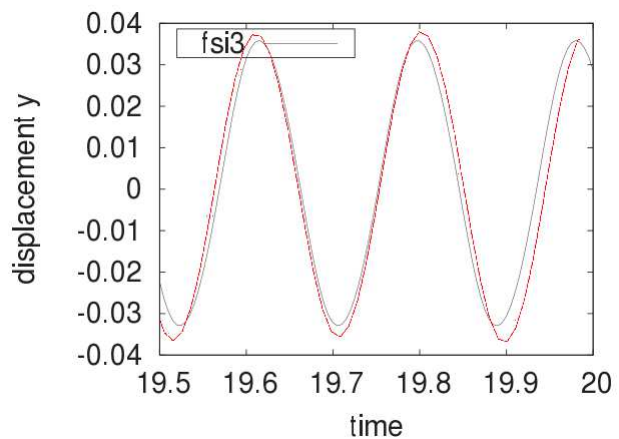


Figure 37: Generalized LSM-XFEM Method overlayed **in red** with Turek, et al results for the third FSI benchmark case.

## 5. Fully Eulerian Fluid-Structure Interaction

Thus far, ALE has been used to allow the fluid mesh to deform, and contour to the structural displacement profile. ALE is convenient, but has limitations on extreme mesh deformations. For example, in many hemodynamics and bio-type applications, solids can exert more of a dense/viscous fluid response. These types of fluid-structure, structure-structure interactions, lead to highly circulatory and complex deformation responses. Furthermore, since the fluid mesh cannot be created or destroyed, the ability to have a fluid-structure action problem where the structures make contact, is not possible with the ALE method.

To this end, I propose to develop a fully Eulerian fluid-structure interaction model. From the fluid side, this makes life simpler, without having to compute gradients of the fluid equations with respect to the mesh deformation, or perform any time averaging schemes. The mesh begins fixed, and stays fixed throughout the simulation. From the structural point of view, however, life becomes much more difficult. Solids are usually modeled via constitutive relationships that are a function of the strain. With a purely Eulerian structural analysis, only the structural velocity solutions are computed. Therefore leaving a gap on how to compute the structural stress tensor. Dunne [35] and Wick [36] have show promising results for fully Eulerian fluid-structure interaction using multiple types of immersed boundary techniques. Their formulations employ a fictitious displacement equation, which is *transported* at the rate of the structural velocity. The principle state variable of the momentum equation is structural velocity, yet it includes the stress, which directly is a function of the displacement. Given the concept of a material deformation, the location of the fluid-structure interface can be computed via the displacement at the current step using either Newton's method, or simple

algebraic calculations and interpolation.

I propose to implement and use their Eulerian structural mechanics formulation. However, I further propose employ a different method to track the location of the interface. Following the theme of this document thus far, I will employ the Level Set and extended Finite Element methods, except now the zero-contour evolves dynamically. Aiming to perform topology optimization with the framework, I seek to reduce any specialized or less modular methods, such as elemental Newton solvers, or algabraic computations. To this end, I assume the nodal Level Set values are degrees of freedom, and they are transported via the structural velocity degrees of freedom. Common practice has been to use a Hamilton-Jacobi equation to transport the scalar variable without any dissipation. However, these methods tend to diverge after multiple time steps, hindering the possibility of transient analyses and optimization routines.

I propose to research a modified Hamilton-Jacobi equation in order to transport the Level Set field, allowing for a streamlined set of partial differential equations that are solved using Newton's method, and can be employed as one nonlinear system into an adjoint sensitivity analysis framework.

### *5.1. Dynamically Evolving Level Set / XFEM Interface with Hamilton-Jacobi Equation*

The modified [18] Hamilton-Jacobi nonlinear partial differential equation is

$$\frac{\partial \phi}{\partial t} + v_i \frac{\partial \phi}{\partial x_i} = \gamma \frac{\partial}{\partial x_i} \left( \epsilon \frac{\partial \phi}{\partial x_i} - \frac{(1+\phi)(1-\phi)}{\left| \frac{\partial \phi}{\partial x_i} \right|} \frac{\partial \phi}{\partial x_i} \right)$$

where  $\phi$  is the Level Set degree of freedom, and  $\gamma$  and  $\varepsilon$  are tuneable parameters.

The weak form of the residual is derived:

$$R^\phi = \int_{\Omega} \delta\phi \left( \frac{\partial\phi}{\partial t} + v_i \frac{\partial\phi}{\partial x_i} - \gamma \frac{\partial}{\partial x_i} \left( \varepsilon \frac{\partial\phi}{\partial x_i} - \frac{(1+\phi)(1-\phi)}{\left| \frac{\partial\phi}{\partial x_i} \right|} \frac{\partial\phi}{\partial x_i} \right) \right) d\Omega = 0$$

Where  $\delta\phi$  is the test function for the Level Set degree of freedom. Next, the higher order derivatives are integrated by parts. For convenience the entire second term is integrated by parts:

$$R^\phi = \int_{\Omega} \delta\phi \left( \dot{\phi} + v_i \frac{\partial\phi}{\partial x_i} - \underbrace{\gamma \frac{\partial}{\partial x_i} \left( \varepsilon \frac{\partial\phi}{\partial x_i} - \frac{(1+\phi)(1-\phi)}{\left| \frac{\partial\phi}{\partial x_i} \right|} \frac{\partial\phi}{\partial x_i} \right)}_{\text{Integrate by Parts}} \right) d\Omega = 0$$

Thus, a boundary term is left over, and a sign switch on the domain term (making it positive). Finally, SUPG stabilization scheme is introduced to account for the convective nature of the PDE:

$$\begin{aligned} R^\phi &= \int_{\Omega} \delta\phi \left( \dot{\phi} + v_i \frac{\partial\phi}{\partial x_i} \right) + \gamma \frac{\partial\delta\phi}{\partial x_i} \left( \varepsilon \frac{\partial\phi}{\partial x_i} - \frac{(1+\phi)(1-\phi)}{\left| \frac{\partial\phi}{\partial x_i} \right|} \frac{\partial\phi}{\partial x_i} \right) d\Omega \\ &\quad - \gamma \int_{\Gamma} \delta\phi \left( \varepsilon \frac{\partial\phi}{\partial x_i} - \frac{(1+\phi)(1-\phi)}{\left| \frac{\partial\phi}{\partial x_i} \right|} \frac{\partial\phi}{\partial x_i} \right) n_i d\Gamma \\ &+ \sum_{e=1}^{n_{ele}} \int_{\Omega} \eta_j \left\{ \dot{\phi} + v_i \frac{\partial\phi}{\partial x_i} - \gamma \frac{\partial}{\partial x_i} \left( \varepsilon \frac{\partial\phi}{\partial x_i} - \frac{(1+\phi)(1-\phi)}{\left| \frac{\partial\phi}{\partial x_i} \right|} \frac{\partial\phi}{\partial x_i} \right) \right\} d\Omega = 0 \end{aligned}$$

where:

$$\begin{aligned} \eta_j &= \tau_{SUPG} v_i |v_i| \frac{\partial\delta\phi}{\partial x_i} \\ \tau_{SUPG} &= \frac{\Omega}{\frac{\pi}{2} |v_i|} \end{aligned} \tag{87}$$

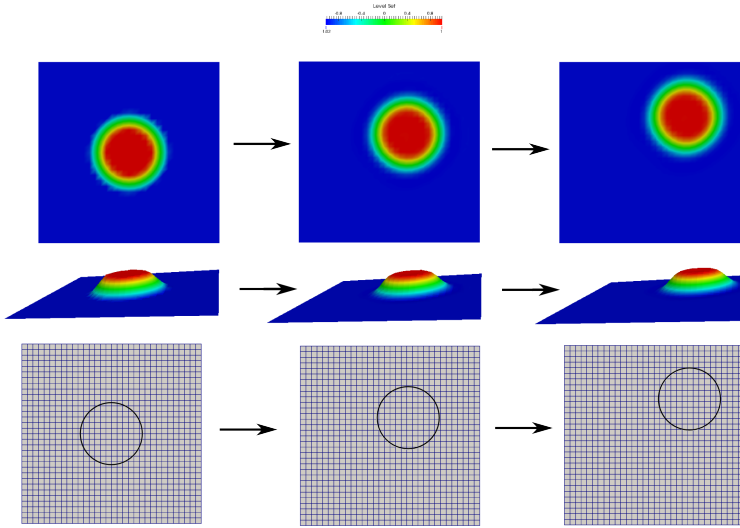


Figure 38: Translating circle Level Set field via Hamilton-Jacobi equation.

### 5.1.1. Numerical Example: Translating Level Set Field via modified Hamilton-Jacobi Formulation

The modified Hamilton-Jacobi formulation is used to translate a circle. Here the Level Set field is prescribed for a truncated cone, and the velocity at all node is  $v_i^o = [1.0, 1.0]$ . Figure 38 gives the evolution of the Level Set field, and resulting zero-contour translating over the mesh. This routine uses standard finite elements, and the values of  $\gamma$  and  $\varepsilon$  are **0.01** and **0.625**, respectively. Note that it is not obvious by the illustrations in figure 38, but the zero-contour, which begins as a perfect circle, begins to lose its circularity as it translates further and further. This has big implications on employing this method for Eulerian structural mechanics, as the interface governs the area or volume of the structure, and if the interface artificially dissipates or distorts, then mass is not conserved. Further investigation is needed into the stabilization and the parameters  $\gamma$  and  $\varepsilon$  to find a balance of stability and "conservation" of positive Level Set value.

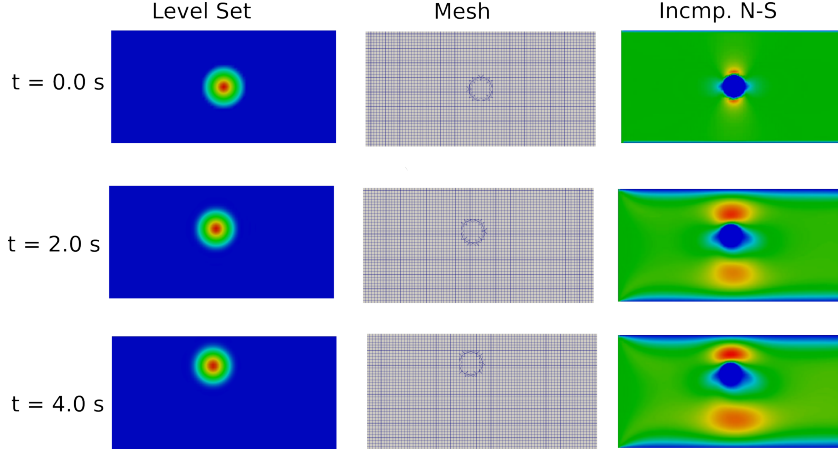


Figure 39: Vertically moving cylinder in parabolic channel flow of  $\text{Re} = 10$ .

### 5.1.2. Numerical Example: Vertically moving Cylinder in Channel Flow

Performing essentially the same problem as the last section, only now simultaneously building an XFEM discretization of the incompressible Navier-Stokes equations allows the simulation of flow about a translating cylinder. Note that the Hamilton-Jacobi equations are solved using standard finite elements. Note here, in contrast to section 4.1.1, the interface velocity  $\tilde{v}_i$  is non-zero, and is equal to the value at which the circle translates at. Here the velocity field is prescribed as  $v_i^o = [0.0, 1.0]$ . The channel width is 10 m, and the height is 5 m. The inflow velocity is parabolic with a mean of  $0.01 \frac{\text{m}}{\text{s}}$ . The viscosity  $\mu^f$  is  $0.01 \frac{\text{kg}}{\text{ms}}$ , and the density  $\rho^f$  is  $1.0 \frac{\text{kg}}{\text{m}^3}$ , and the cylinder diameter is 2.0 m. These parameters result in a Reynolds number of **Re = 10**. The timestep used is 0.01 s, and the simulation is run for 500 time steps (5 seconds final time). For the modified Hamilton-Jacobi equation 87, the parameters are  $\gamma = 0.01$  and  $\epsilon = 0.625$ . Figure 39 shows reasonable results, but given the low Reynolds number, I would expect to see better flow results. I hypothesize that as the Reynolds number is increased, the incom-

pressbile Navier-Stokes equations will begin to diverge with the method. Further stability analysis is needed for this method.

## 5.2. Eulerian Structural Mechanics

This section presents the theory behind an Eulerian (based on rates) structural analysis. Most of this section closely follows [35] and [36]. The constitutive equation for an incompressible Neo-Hookean material:

$$\boldsymbol{\sigma}_s = -p_s \mathbf{I} + 2C_1 \mathbf{B} \quad (88)$$

where  $p_s$  is the pressure,  $\mathbf{B}$  is the left Cauchy-Green deformation tensor, and

$$C_1 = \frac{\mu^s}{2} \quad (89)$$

where  $\mu^s$  is the shear modulus of the material. Note a bold symbol represents a tensor. Next, the conservation of momentum in a Lagrangian reference frame, and its incompressibility constraint (conservation of mass) are:

$$\rho^s \widehat{\delta v_{s,x}} \left( \frac{\partial \widehat{v}_{s,x}}{\partial t} \right) + \frac{1}{2} \left( \frac{\partial \widehat{\delta v_{s,x}}}{\partial y} + \frac{\partial \widehat{\delta v_{s,y}}}{\partial y} \right) \widehat{\boldsymbol{\sigma}^s} \widehat{\mathbf{F}}^{-T} = \mathbf{g}_x \quad (90)$$

$$\widehat{\mathbf{F}} = \mathbf{I} + \widehat{\nabla} \widehat{\mathbf{u}}_s \quad (91)$$

$$\widehat{\delta p_s} \det \widehat{\mathbf{F}} = 0 \quad (92)$$

$$\mathbf{B} = \widehat{\mathbf{F}} \widehat{\mathbf{F}}^T - 1 \quad (93)$$

where  $v_{s,i}$  is the structural velocity in the  $i$ th direction,  $\delta v_{s,i}$  is the test function for the structural velocity, and  $u_i$  is structural displacement.  $\mathbf{F}$  is the deformation gradient, and  $\delta p_s$  is the structure pressure test function. Here, a hat above a quantity represents an initial value at  $t=0$ . Next, a way of mapping the displacement a material point undergoes as the material deforms is required. A deformation function  $\mathbf{D}$  is introduced, and it is asserted that:

$$\det \widehat{\nabla} \widehat{\mathbf{D}} = \det \widehat{\mathbf{F}} = 1 \quad (94)$$

Next, a set of initial positions of all points  $\theta$  is presented. For all  $t$ ,  $\theta(t, x)$  will always provide the initial position of point  $x$ . Each material point advects with velocity  $v_s$ , which in a structure only field, the structural velocity is simply the convective velocity  $w$ . The weak form of the governing equation for the initial positions:

$$\delta\theta \left( \frac{\partial\theta}{\partial t} + (\mathbf{v} \cdot \nabla) \theta \right) = 0 \quad (95)$$

where  $\delta\theta$  is the test function for the initial point set. Further manipulation using the initial positions leads to a definition for the Eulerian displacement gradient  $\mathbf{F}$  and the Cauchy stress tensor:

$$\mathbf{F} = (1 - \nabla \mathbf{u})^{-1} \quad (96)$$

$$\boldsymbol{\sigma}_s = -p_s \mathbf{I} + \mu^s (\mathbf{F} \mathbf{F}^T - \mathbf{I}) \quad (97)$$

Next the momentum equation is written in Eulerian notation, and the continuity equation is replaced with the divergence of the velocity equals zero (similar to an incompressible fluid):

$$\rho^s \delta v_{s,x} \left( \frac{\partial v_{s,x}}{\partial t} + v_{s,x} \frac{\partial v_{s,x}}{\partial x} + v_{s,y} \frac{\partial v_{s,x}}{\partial y} \right) + \frac{1}{2} \left( \frac{\partial \delta v_{s,x}}{\partial y} + \frac{\partial \delta v_{s,y}}{\partial x} \right) \boldsymbol{\sigma}_s \mathbf{F}^{-T} = \mathbf{g} \quad (98)$$

$$\delta p_s (\nabla \cdot \mathbf{v}_s) = 0 \quad (99)$$

Next, the total structural velocity and displacement equations in weak form are given. Stabilization for the convective system will be ignored for now.

$$R_{u_x} = \int_{\Omega} \delta u_{s,x} \left( \frac{\partial u_{s,x}}{\partial t} - v_{s,x} + \left( v_{s,x} \frac{\partial u_{s,x}}{\partial x} + v_{s,y} \frac{\partial u_{s,x}}{\partial y} \right) \right) d\Omega \quad (100)$$

$$R_{u_y} = \int_{\Omega} \delta u_{s,y} \left( \frac{\partial u_{s,y}}{\partial t} - v_{s,y} + \left( v_{s,x} \frac{\partial u_{s,y}}{\partial x} + v_{s,y} \frac{\partial u_{s,y}}{\partial y} \right) \right) d\Omega \quad (101)$$

$$R_{v_x} = \int_{\Omega} \left( \rho^s \delta v_{s,x} \left( \frac{\partial v_{s,x}}{\partial t} + v_{s,x} \frac{\partial v_{s,x}}{\partial x} + v_{s,y} \frac{\partial v_{s,x}}{\partial y} \right) + \frac{1}{2} \left( \frac{\partial \delta v_{s,x}}{\partial y} + \frac{\partial \delta v_{s,y}}{\partial y} \right) \boldsymbol{\sigma}^s \mathbf{F}^{-T} \right) d\Omega \quad (102)$$

$$R_{v_y} = \int_{\Omega} \left( \rho^s \delta v_{s,y} \left( \frac{\partial v_{s,y}}{\partial t} + v_{s,x} \frac{\partial v_{s,y}}{\partial x} + v_{s,y} \frac{\partial v_{s,y}}{\partial y} \right) + \frac{1}{2} \left( \frac{\partial \delta v_{s,x}}{\partial y} + \frac{\partial \delta v_{s,y}}{\partial y} \right) \boldsymbol{\sigma}^s \mathbf{F}^{-T} \right) d\Omega \quad (103)$$

$$R_p = \int_{\Omega} \delta p_s \left( \frac{\partial v_{s,x}}{\partial x} + \frac{\partial v_{s,y}}{\partial y} \right) d\Omega \quad (104)$$

Here  $\delta u_{s,i}$  is the displacement test function in the  $i$ th direction. Where:

$$\boldsymbol{\sigma}^s = -p\mathbf{I} + \mu^s (\mathbf{F}\mathbf{F}^T - \mathbf{I}) \quad (105)$$

The above constitutive equation is the typical form for an incompressible Neo-Hookean material, and framework exists to build  $F$ , the displacement gradient tensor. Equations (13) and (14) take use of the fact that for the solid

$$\mathbf{u}_s(\bar{\mathbf{x}}, t) = \bar{\boldsymbol{\theta}} + \mathbf{v}_s(\bar{\mathbf{x}}, t) \quad (106)$$

Where  $\bar{\boldsymbol{\theta}}$  is the initial position of a material point. Therefore for a solid it appears that there is a transport equation for the displacement with convective velocity that is seen in the conservation of momentum equations. The structural displacement convective velocity is chosen to be the structural velocity, but this does not necessarily have to be the case. One interesting characteristic, is that the displacement equations have a source term that is the velocity. This is consistent with both [35] and [36], however.

## 6. Conclusion and Thesis Time Frame

I have presented the theory of incompressible fluid-structure interaction using a arbitrary-Lagrangian-Eulerian reference frame, nonlinear structural models, and a monolithic solver that is fully parallelized and 3D capable. I have verified my methods and implementation by presenting results for unsteady fluid problems, with stabilized finite elements, and ALE. I will be submitting the document *he Level Set and Extended Finite Element Methods for Topology Optimization of Fluid-Structure Interaction Problems* for publication in the near future, which presents theory for the aforementioned fluid dynamics on moving mesh coupled monolithically with structural models, in addition to the Level Set and extended finite element methods to be used for topology optimization. The document presents two and three dimensional topology optimization results both with a traditional density interpolation method, and the new Level Set / extended Finite Element method.

Next, I presented a new method that utilizes the Level Set and XFEM, in combination with stabilized Lagrange multipliers, to predict the coupled fluid-structure response without the need for a body fitted mesh. This generalization of the previously presented method allows for quick analysis of any Level Set zero-contour that is prescribed by mathematical functions or images. I verified the method using transient fluid-structure interaction problems with an immersed structural (nonlinear) boundary. Further, the new method allows for seamless integration to a topology optimization algorithm enabling simultaneous shape and topology (wet) optimization of the fluid-structure system. This is yet to be completed, and appears on the proposal schedule.

Finally, I presented the idea and theory of fully Eulerian fluid-structure interaction, and both why it is desirable, and potential challenges that lie ahead. I presented two simple problems that incorporate a dynamically evolving interface that is transported by a modified Hamilton-Jacobi formulation.

I propose to complete the following tasks for my doctoral thesis:

- Extend the generalized LSM-XFEM fluid-structure interaction method to three dimensions, and verify accuracy.
- Study further the stabilized Lagrange Multiplier interface coupling method and how it affects the interface error given stabilizing penalty factors. Potentially investigate 3-Lagrange Multiplier schemes, and/or Nitche schemes.
- Perform optimization with the generalized LSM-XFEM fluid-structure interaction method.
- Complete the implementation Eulerian structural element for the velocity based momentum equation, and the displacement evolution equation. Complete a simple structural test problem of a cantilever beam surrounded by void on a fixed grid. Use the Level Set method with Hamilton-Jacobi equation, and XFEM to verify against analytical deflection solution.
- Perform fully Eulerian fluid-structure interaction, and solve both stationary and transient problems as was presented for both methods in this document.
- As a capstone, perform topology optimization of the fluid-struture system, allowing for creation of pieces of structural material that could *simply fly down the channel*.

I propose the time of about *nine months* to complete the necessary development and verification to perform topology optimization of a fully Eulerian fluid-structure system. Completing verification and generating results by December, 2014, will allow me to compile and finalize my Doctoral Thesis enabling submission and graduation in Spring semester, 2015. Figure 40 shows a brief break down for when and what needs to be completed before December, 2014.

APR	MAY	JUN	JUL	AUG	SEP	OCT	NOV	DEC
3D Generalized LSM-XFEM	Begin publication for generalized LSM-XFEM optimization	USNCTAM Conference Presentation	Verify Mass Conservation Stability and Robustness of Eulerian Structural Formulation	Fluid-Structure Interaction with Eulerian Structural Formulation	Develop and verify transient 3D Eulerian FSI	Adjoint Sensitivity Analysis of Eulerian System	Topology Optimization of Eulerian Fluid-Structure System	Further examples and development of optimization of Eulerian FSI Systems
2D Generalized LSM-XFEM Optimization.	Cantilever Beam Eulerian Structural Test Problem	Develop Eulerian Structural Analysis	Compare to Analytical Solution					

Figure 40: Thesis development and results timeline.

## 7. Bibliography

- [1] Sandeep Sovani. Putting physics to work in next-generation automotive and aerospace engineering. Technical report.
- [2] L. Sun. Fretting crack investigation. *WEMESURF course, 21-25 June 2010, Paris*, 2010.
- [3] Annual report 20112012: Epsrc centre for innovative manufacturing in additive manufacturing. Technical report.
- [4] J. W. Whitehead. The micro-drone revolution: Roachbots, ravens, mosquitos, and more. *Before It's News*, 2013.
- [5] A. P. Randles. Multiscale hemodynamics. *Harvard School of Engineering*, 2013.
- [6] P. K. Kundu and I. M. Cohen. *Fluid Mechanics*. Elsevier Academic Press, 2008.
- [7] T.J.R. Hughes and E. Cliffs. *The Finite Element Method: Linear Static and Dynamic Finite Element Analysis*. Dover Publications, 2000.
- [8] A.N. Brooks and T.J.R. Hughes. Streamline upwind/petrov-gelerkin formulations for convection dominated flows with particular emphasis on the incompressible navier-stokes equations. *Comuter Methods in Applied Mechanics and Engineering*, 32:199–259, 1982.
- [9] T. E. Tezduyar, S. Mittal, S. E. Ray, and R. Shih. Incompressible flow computations with stabilized bilinear and linear equal-order-interpolation

- velocity-pressure elements. *Computer Methods in Applied Mechanics and Engineering*, 95:221–242, 1992.
- [10] M. Schafer and S. Turek. Incompressible flow computations with stabilized bilinear and linear equal-order-interpolation velocity-pressure elements. Technical report, University of Heidelberg, 1992.
- [11] J.P. Halleux J. Donea, S. Giuliani. An arbitrary lagrangian-eulerian finite element method for transient dynamic fluid-structure interaction. *Comuter Methods in Applied Mechanics and Engineering*, 33:689–723, 1982.
- [12] C. Farhat and P. Geuzaine. Design and analysis of robust ale time-integrators for the solution of unsteady flow problems on moving grids. *Comuter Methods in Applied Mechanics and Engineering*, 193:4073–4095, 2004.
- [13] M. Howard. *Finite Element Modeling and Optimization of High-Speed Aerothermoelastic Systems*. PhD thesis, University of Colorado, Boulder, 2010.
- [14] C. Farhat and P. Geuzaine. Space-time finite element computation of compressible flows involving moving boundaries and interfaces. *Comuter Methods in Applied Mechanics and Engineering*, 107:209–223, 1992.
- [15] C. M. Deluca. *Numerical Modeling and Optimization of Mechanically Active Electrochemical Systems*. PhD thesis, University of Colorado, Boulder, 2013.
- [16] J. Chung and G.M. Hulbert. A time integration algorithm for structural dynamics with improved numerical dissipation: The generalized- $\alpha$  method. *Journal of Applied Mechanics*, 60:372–375, 1993.

- [17] Micah Howard and Steven Bova. Coupling strategies for high-speed aero-heating problems. In *Aerospace Sciences Meetings*, pages –. American Institute of Aeronautics and Astronautics, 2011.
- [18] *Fluid-Structure Interaction.*
- [19] Stefan Turek and Jaroslav Hron. Proposal for numerical benchmarking of fluid-structure interaction between an elastic object and laminar incompressible flow. In Hans-Joachim Bungartz and Michael Schfer, editors, *Fluid-Structure Interaction*, volume 53 of *Lecture Notes in Computational Science and Engineering*, pages 371–385. Springer Berlin Heidelberg, 2006.
- [20] Michael Heroux, Roscoe Bartlett, Vicki Howle Robert Hoekstra, Jonathan Hu, Tamara Kolda, Richard Lehoucq, Kevin Long, Roger Pawlowski, Eric Phipps, Andrew Salinger, Heidi Thornquist, Ray Tuminaro, James Willenbring, and Alan Williams. An Overview of Trilinos. Technical Report SAND2003-2927, Sandia National Laboratories, 2003.
- [21] K. Svanberg. The method of moving asymptotes - a new method for structural optimization. *International Journal for Numerical Methods in Engineering*, 24(2):359–373, 1987.
- [22] Kurt Maute. Design optimization of aerospace structures. Technical report, University of Colorado, Boulder, 2007.
- [23] Sebastian Kreissl. *Topology Optimization of Flow Problems Modeled by the Incompressible Navier-Stokes Equations*. PhD thesis, University of Colorado, Boulder, 2011.

- [24] D. Makhija and K. Maute. Numerical instabilities in level set topology optimization with the extended finite element method. *Structural and Multidisciplinary Optimization*, 2013.
- [25] Sebastian Kreissl and Kurt Maute. Levelset based fluid topology optimization using the extended finite element method. *Structural and Multidisciplinary Optimization*, pages 1–16, 2012.
- [26] M. Allen and Kurt Maute. Reliability-based shape optimization of structures undergoing fluid structure interaction phenomena. *Computer Methods in Applied Mechanics and Engineering*, 194:3472–3495, 2005.
- [27] K. Maute and M. Allen. Conceptual design of aeroelastic structures by topology optimization. *Structural and Multidisciplinary Optimization*, 27:27–42, 2004.
- [28] Sebastian Kreissl, Georg Pingen, Anton Evgrafov, and Kurt Maute. Topology optimization of flexible micro-fluidic devices. *Structural and Multidisciplinary Optimization*, 42(4):495–516, 2010.
- [29] Gil Ho Yoon. Topology optimization for stationary fluid-structure interaction problems using a new monolithic formulation. In *8th World Congress on Structural and Multidisciplinary Optimization*, 2009.
- [30] Jessica D. Sanders, John E. Dolbow, and Tod A. Laursen. On methods for stabilizing constraints over enriched interfaces in elasticity. *Int. J. Numer. Meth. Engng.*, 78(9):1009–1036, 2009.
- [31] Isaac Harari and John Dolbow. Analysis of an efficient finite element method

- for embedded interface problems. *Computational Mechanics*, 46:205–211, 2010.
- [32] Chandrasekhar Annavarapu, Martin Hautefeuille, and John E. Dolbow. A robust nitsches formulation for interface problems. *Computer Methods in Applied Mechanics and Engineering*, 225:228(0):44 – 54, 2012.
- [33] Martin Hautefeuille, Chandrasekhar Annavarapu, and John E. Dolbow. Robust imposition of dirichlet boundary conditions on embedded surfaces. *International Journal for Numerical Methods in Engineering*, 90(1):40–64, 2012.
- [34] JessicaD. Sanders, TodA. Laursen, and MichaelA. Puso. A nitsche embedded mesh method. *Computational Mechanics*, 49(2):243–257, 2012.
- [35] Thomas Dunne and Rolf Rannacher. Adaptive finite element approximation of fluid-structure interaction based on an eulerian variational formulation. In Hans-Joachim Bungartz and Michael Schfer, editors, *Fluid-Structure Interaction*, volume 53 of *Lecture Notes in Computational Science and Engineering*, pages 110–145. Springer Berlin Heidelberg, 2006.
- [36] Thomas Wick. Fully eulerian fluidstructure interaction for time-dependent problems. *Computer Methods in Applied Mechanics and Engineering*, 255(0):14 – 26, 2013.

## **8. Appendix**

**A Pre-Print: The Level Set and Extended Finite Element Methods for Topology Optimization of Fluid-Structure Interaction Problems**

# The Level Set and Extended Finite Element Methods for Topology Optimization of Tightly Coupled Fluid-Structure Interaction Problems

Nicholas Jenkins, Kurt Maute\*

*Department of Aerospace Engineering, University of Colorado at Boulder, Boulder, CO 80305,  
United States*

---

## Abstract

This paper presents a new method for topology optimization of strongly coupled, steady fluid structure interaction (FSI) problems. We develop a smooth function to optimize the Level Set (LS) field directly, which describes the internal structural topology of the FSI problem. We employ the extended finite element method (XFEM) to discretize the structural geometry. The XFEM discretized structure is embedded in a monolithic FSI framework built on a stabilized arbitrary-Lagrangian-Eulerian incompressible Navier-Stokes formulation. The monolithic scheme is robust for large deformation FSI problems, and allows for a standard nonlinear adjoint sensitivity analysis calculation. The LS-XFEM allows for crisp structural design molds in contrast to coarse or blurred profiles observed with conventional density interpolation methods. Optimization results obtained using this new method are compared to results obtained with the well-known Solid Isotropic Material Penalization (SIMP) method. Differences and

---

\*Corresponding author. Tel.: (303) 735-2103

Email addresses: Nicholas.Jenkins@colorado.edu (Nicholas Jenkins),  
Kurt.Maute@colorado.edu (Kurt Maute)

advantages are discussed for two and three-dimensional numerical examples. In contrast to density based methods, the LS-XFEM yields clearly defined features on even a coarse design grid, and provides greater flexibility for multi-physics applications.

*Keywords:* Topology Optimization, Extended Finite Element Method, Level Set Method, Fluid-Structure Interaction, Monolithic

---

## 1. Introduction

Fluid structure interaction is of great interest in a variety of engineering disciplines such as in aerospace, bio-medical, and renewable energy. Designing a fluid-structure system is significant in the engineering community because of the often non-intuitive response of the coupled system. Tightly coupled fluid-structure systems, defined by flexible structures immersed in fluid, prove to be difficult to acquire numerical solutions to and are often overly approximated in the context of design optimization. Embedding an FSI forward analysis in a computational optimization framework has further challenges stemming from applying conventional methods that are poorly suited for multi-physics applications. In this work we propose a new class of solution methods to address the challenge of performing topology optimization of tightly coupled fluid-structure interaction problems.

The necessary constituents of applying gradient based optimization to a fluid-structure system are: numerical solution to the coupled partial differential equations (PDE) of structural elasticity and fluid mechanics, and calculation of the system response sensitivity to the design geometry. The paramount challenge associated with multi-physics optimization is incorporating each discipline in calculation of both the design response and the sensitivity.

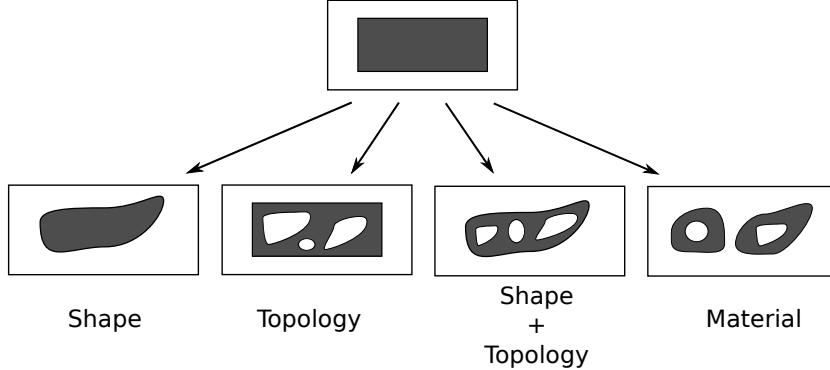


Figure 1: Fluid-Structure Interaction Optimization Methods.

Within the regime of FSI optimization each previous work varies by the following attributes: first, method of solving the FSI system; second, method of modeling the FSI interface; and third, method of varying the design geometry. Solving the FSI system is done in either of two ways: staggered or monolithic. The FSI interface can be assumed to be fixed (very small deformations), one-way coupled (structure only feels the fluid load), or two-way coupled (structure feels fluid load, and fluid displaces with structure). In the context of the design problem to be varied, one could vary only the outer shape, the internal topology, both the shape and topology, or the most general approach: material variation. Simple depictions of these methods are shown in figure 1.

Material variation is typically accomplished by velocity penalization, or the introduction of the idea of porosity, where high porosity is fluid, and low porosity is solid. In the staggered FSI solver category, Maute and Allen [1],[2] performed shape optimization with constant and one-way coupled interfaces. Maute and Allen [1], Stanford and Ifju [27], Stanford and Beran (2011) have performed topology optimization while holding the FSI interface constant in Euler flow sim-

ulations. James and Kai [12] performed a topology and shape optimization of an FSI system with staggered, Euler flow. Employing monolithic solvers, Kreissl and Maute [14] optimized the material topology of one-way coupled incompressible flow systems, and Yoon [32] employed a two-way coupled monolithic solver to optimize the material topology of FSI systems in viscous flow. Each geometric option yields both advantages and downfalls. Shape optimization is the most restrictive, but material optimization does not guarantee accuracy in the pressure field [15] and leads to blurred solutions. We choose to solve the purely topology optimization problem (second illustration from the left in figure1) with a fixed FSI boundary with respect to the design variables. However, we note that the FSI interface is two-way coupled and allows for large deformations in the system response calculation. For example, this optimization model would be applicable if the aerodynamic characteristics of a wing body have been determined, but it is desired to yield minimum compliance during flight.

The conventional method for topology optimization of structural systems is to assign each discrete volume a density design variable. All of the aforementioned work relies on density methods typically utilizing the well known Solid Isotropic Material Penalization (SIMP) method to push the density distributions to the minimum and maximum values (void and solid).

Density methods can suffer from fuzzy or jagged geometry edges (see figure 1), and require a high mesh density to yield clear design geometries which when combined with the large mesh constraints of FSI systems can be difficult to achieve. Further, as we will show, extending density methods to three dimensions proves cumbersome in acquiring clear solutions for fluid-structure interaction problems, and the hinderance of fine mesh requirements is compounded. To

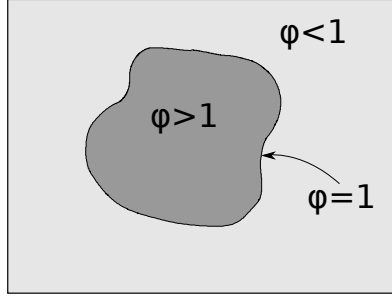


Figure 2: Levelset Field.

address these shortcomings, we propose to employ the Level Set Method (LSM) to designate the exact location of the interface between structural material and void (or a separate material, as will be discussed subsequently). The LSM, developed by Osher and Sethian [21], is widely used to track an interface by employing a higher dimensional field  $-1 \leq \phi_i \leq 1$ , where the zero contour  $\phi_i = 0$  designates the interface location. James and Martins [12] used the LSM in conjunction with a Hamilton-Jacobi transport filter between the optimization algorithm and the physical model. See also van Djik, et al [30] for use of the LSM in context of topology optimization. This work will take after that of Kreissl and Maute [15], Makhija and Maute [17], where an extended finite element method (XFEM) discretization is used to predict the response of a material with geometry described by the LSM. The XFEM has emerged as a viable method for multi-physics problems due to its accuracy in providing solutions to problems with discontinuities (eg. multiple materials, shocks, cracks) on a fixed grids. See [9], [8], [13] for a wide range of multi-physics problems solved using the XFEM.

We intend to show that the XFEM addresses the shortcomings of density based methods by yielding crisp interface definitions (see figure 1) on even relatively

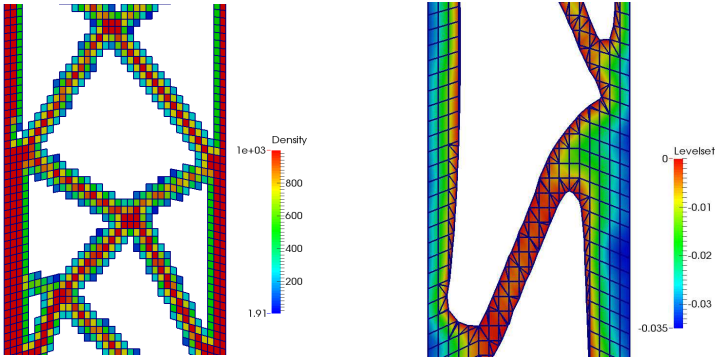


Figure 3: Examples of geometry described by density method (left) and Extended Finite Element Method (right)

coarse design meshes. Further, we present clear topology optimization results for three dimensional FSI problems where SIMP cannot provide non-fuzzy designs. We achieve these goals by employing the LSM as the link between the search algorithm and the XFEM discretization of the structural model. Aiming to reduce the complexity of the gradient computation and increase the robustness to be able to solve large deformation FSI problems, we immerse the structure in a monolithic two-way coupled FSI framework built on a stabilized finite element discretization of the incompressible Navier-Stokes (INS) equations in an arbitrary-Lagrangian-Eulerian (ALE) reference frame.

## 2. Fluid-Structure Interaction Model

We employ the Streamline-Upwind-Petrov-Galerkin (SUPG) and Pressure-Stabilized-Petrov-Galerkin (PSPG) stabilized Finite Element (FE) [29] formulation to compute solutions to the Incompressible Navier-Stokes (INS) balance equations. In order to couple the Eulerian frame of the fluid to the Lagrangian frame of the structure, the popular Arbitrary-Lagrangian-Eulerian (ALE) method

has been utilized to allow the fluid mesh to displace in a Lagrangian fashion. A moving fluid mesh enables the fluid to follow the deformed configuration of the structure. The alternative approach would be to evolve the structural velocity in an Eulerian configuration enabling a completely fixed grid Eulerian FSI analysis. See Dunne [6], Wick [31] for fully Eulerian monolithic FSI results. While a fully Eulerian framework boasts the most generality for large and complex deformations, an approximated and in-depth structural analysis is necessary due to the solid stress' dependency upon the displacement states (Eulerian analyses rely on rate based material-flow). Additionally, mass conservation and interface tracking are two issues that can lead to a loss of accuracy in a fully Eulerian FSI framework. A generalized Lagrangian framework (global grid deformation) has limitations on extremely large FSI displacements, but proceeds most naturally with the majority of the strongly coupled problems we focus on here.

The fluid, fluid mesh, and structural domains are  $\Omega^f$ ,  $\Omega^m$ , and  $\Omega^s$  with boundaries  $\Gamma^f, \Gamma^m, \Gamma^s$ , respectively. To showcase the new methods ability to accommodate multi-phase analyses, we denote the structure as being in general a composition of two structural phases  $\Omega^s = \Omega_A^s \cup \Omega_B^s$  and the interface between each phase  $\Gamma_{A,B}^s = \Omega_A^s \cap \Omega_B^s$ . In the examples shown we require a "skin" around the structure to not allow any existence of void or soft material resulting in a numerical instability. Therefore, the FSI interface is  $\Gamma^{fsi} = \Omega^f \cap \Omega^s = \Omega^f \cap \Omega_A^s$ .

Partitioned FSI schemes [7] have the advantage to be able to combine multiple discretization methods and different reference frames, but they are limited in solving strongly coupled FSI problems that result from large deforming soft structures. Additionally, staggered analyses require a specialized and more cumbersome sensitivity analysis, especially when operating in large, parallel scenarios

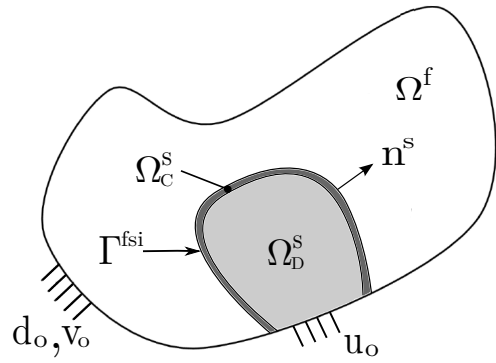


Figure 4: Diagram of fluid-structure interaction problem.  $v_0$ ,  $u_0$ , and  $d_0$  are the Dirichlet conditions for the fluid, structure, and fluid mesh, respectively.

[18]. Therefore, we present the weak formulation of the steady FSI problem in a monolithic set which is in general nonlinear and solved with Newton’s method.

Find  $p, v_i, u_i, d_i$ ,

such that:

$$R^f = \int_{\Omega^f} \left( \psi_i \frac{\partial v_i}{\partial x_j} v_j + \frac{\partial \psi_i}{\partial x_j} \sigma_{ij}^f + \eta \frac{\partial v_i}{\partial x_i} \right) d\Omega^f - \int_{\Gamma^f} \psi_i \sigma_{ij}^f n_j^f d\Gamma^f \\ + \sum_{n_e} \int_{\Omega^f} \left( \frac{\partial v_i}{\partial t} + \frac{\partial v_i}{\partial x_k} v_k^D - \frac{\partial \sigma_{ik}^f}{\partial x_k} \right) \left( \tau_{SUPG} v_j^D \frac{\partial \psi_i}{\partial x_j} + \tau_{PSPG} \frac{\partial \eta}{\partial x_i} \right) d\Omega^f = 0 \quad (1)$$

$$R^m = \int_{\Omega^f} \frac{\partial \xi_i}{\partial x_j} \sigma_{ij}^m d\Omega^f - \int_{\Gamma^f} \xi_i \sigma_{ij}^m n_j^f d\Gamma^f = 0 \quad (2)$$

$$R^s = \int_{\Omega_A^s} \frac{\partial \chi_{A,i}}{\partial x_j} \sigma_{A,ij}^s d\Omega_A^s - \int_{\Gamma_A^s} \chi_i^A \sigma_{ij}^{s,A} n_j^{s,A} d\Gamma_A^s \\ + \int_{\Omega_B^s} \frac{\partial \chi_{B,i}}{\partial x_j} \sigma_{B,ij}^s d\Omega_B^s - \int_{\Gamma_B^s} \chi_i^B \sigma_{ij}^{s,B} n_j^{s,B} d\Gamma_B^s \\ + \int_{\Gamma_{A,B}^s} [\chi_i] \lambda_i d\Gamma_{A,B}^s + \gamma \int_{\Gamma_{A,B}^s} \mu_i [u_i] d\Gamma_{A,B}^s + \int_{\Gamma_{A,B}^s} \mu_i \left( \lambda_i - \bar{\sigma}_{ij}^s n_j^{A,B} \right) d\Gamma_{A,B}^s = 0 \quad (3)$$

$R^f$ ,  $R^m$ , and  $R^s$  are the fluid, fluid mesh, and structural residuals.  $n_j^f$  and  $n_j^s$  are the fluid and solid outward facing normals, respectively. For brevity we assert that  $\Omega^m = \Omega^f$  and  $\Gamma^m = \Gamma^f$ .  $v_i$  is the fluid velocity,  $u_i$  is the structural displacement, and  $d_i$  is the mesh displacement.  $\psi_i$ ,  $\eta$ ,  $\xi_i$ , and  $\chi_i$  are the test functions for fluid velocity, fluid pressure, fluid mesh displacement, and structural displacement, respectively.

Equation (3) contains the weak form for both structural materials (A) and (B) in addition to the XFEM interface conditions necessary to preserve  $C^0$  continuity, which the FEM requires. Here a bracketed quantity represents the difference:  $[z] = z^A - z^B$ . The remainder of the terms in equation 3 will be described in detail in a subsequent section.

$\tau_{SUPG}$  and  $\tau_{PSPG}$  are parameters in the SUPG/PSPG stabilization scheme, and the definitions can be found in the original reference [29] or in the more recent work [16].  $\sigma_{ij}^f$ ,  $\sigma_{ij}^s$ , and  $\sigma_{ij}^m$  are the stress tensors for the fluid, solid, and fluid mesh with

constitutive laws given by:

$$\sigma_{ij}^f = -p\delta_{ij} + \mu^f \left( \frac{\partial v_i}{\partial x_j} + \frac{\partial v_j}{\partial x_i} \right) \quad (4)$$

$$\sigma_{ij}^{s,A} = \Phi(u_i^A) \quad (5)$$

$$\sigma_{ij}^{s,B} = \Phi(u_i^B) \quad (6)$$

$$\sigma_{ij}^m = \Phi(d_i) \quad (7)$$

where  $p$ ,  $\mu^f$  are the fluid mechanical pressure, and dynamic viscosity, respectively.  $\delta_{ij}$  is the Kronicker delta. Here,  $\Phi(z_i)$  is the elastic constitutive equation for state variable  $z_i$  with corresponding kinematic equation:

$$\Phi(z_i) = C_{ijkl}^z \epsilon_{kl}(z_i) \quad (8)$$

$$\epsilon_{ij}(z_i) = \frac{1}{2} \left( \frac{\partial z_i}{\partial x_j} + \frac{\partial z_j}{\partial x_i} \right) \quad (9)$$

$C_{ijkl}^s$  is the elastic constitutive tensor. After conservation of angular momentum, symmetry and isotropy assumptions,  $C_{ijkl}^s$  can be reduced to a function of the elastic modulus ( $E$ ) and Poisson's ratio only. For the fluid mesh constitutive tensor we set the Poisson's ratio to zero (fully compressible). The fluid mesh modulus has no physical relevance because the mesh is one-way coupled (has no reaction force), so we set  $E^m$  to 1.0.

We note that in an unsteady FSI formulation there would exist inertial terms in each momentum equation, and an ALE "differential" velocity to be taken into account in the fluid convective terms. Note further when computing the gradient of the residuals to be used in Newton's method and the sensitivity analysis, a consistent Jacobian matrix for all dependencies (fluid, mesh, and structural degrees of freedom) must be computed.

### 2.1. Levelset / Extended Finite Element Discretization

In standard finite element methods the structural displacement field  $u$  is represented by a sum of interpolated values computed from interpolation functions  $\chi_i(x)$  and the degrees of freedom  $u_i$ :

$$u(x) = \sum_{i=1}^n \chi_i(x) u_i \quad (10)$$

We adopt the generalized version of the step enrichment presented in [17], originally proposed by Hansbo and Hansbo [10]:

$$u(x) = \sum_{m=1}^M \left( H(-\phi) \sum_{i=1}^n \chi_i u_{i,m}^A + H(\phi) \sum_{i=1}^n \chi_i u_{i,m}^B \right) \quad (11)$$

where  $m$  is the "enrichment level", with maximum number  $M$ , and  $u_{i,m}^k$  is the degree of freedom at node  $i$  for phase  $k$ , and  $H$  is the Heaviside function,

$$H(z) = \begin{cases} 1 & \text{if } z > 0; \\ 0 & \text{if } z \leq 0. \end{cases}$$

The enrichment of the structural degrees of freedom given above allows for complex configurations, and eliminates any spurious transfer of physics [17]. Each cell in the structural domain can potentially be intersected (via the zero Level Set value) in a non-symmetric configuration. In order to accurately integrate the FEM equations, the intersected cells are decomposed into triangles (or tetrahedra in 3D) to allow for standard Gauss quadrature in each sub-domain.

### 2.2. XFEM Interface Conditions

The Heaviside degree of freedom enrichment does not satisfy the continuity requirements that the weak form is built on. For "material-void" problems, no interface contributions are necessary, however, for multiple materials (A and B)

we require such conditions. We employ the stabilized Lagrange multiplier method to augment the weak form to satisfy the structural displacement continuity across XFEM intersections.

In equation (3) we introduce the Lagrange Multiplier  $\lambda_i$  with the associated test function  $\mu_i$  to model the addition of a discontinuous interface between material (A) and material (B). The fifth term in equation (3) accounts for the addition of this Lagrange Multiplier from both sides (A) and (B). The sixth term in equation (3) enforces the continuity in the displacement fields, and the last term accounts for compatibility in the traction field. The weight  $\gamma$  determines how well the interface condition is satisfied yet leads to ill-conditioning of the linear system.

### 2.3. FSI Model: Interface Coupling

The fluid and structure are coupled at the fluid structure interface  $\Gamma^{fsi}$  by enforcing continuity of traction, displacement, and velocity. Howard and Bova [11] describe a method of coupling the heat equation to the compressible flow energy equation by enforcing continuity of head flux across the interface. The same idea was employed here as a boundary traction (momentum flux). This embedded method does not rely on Lagrange Multipliers, which lead to ill conditioning of the linear system.

For all  $x_i \in \Gamma^{fsi}$ :

$$\int_{\Gamma^{fsi}} (\sigma_{ij}^f \cdot n_j^f - \sigma_{ij}^s \cdot n_j^s) d\Gamma^{fsi} = 0 \quad (12)$$

$$\int_{\Gamma^{fsi}} (v_i - \dot{u}_i) d\Gamma^{fsi} = 0 \quad (13)$$

$$\int_{\Gamma^{fsi}} (d_i - u_i) d\Gamma^{fsi} = 0 \quad (14)$$

### 3. Geometry Description

Referring to figure 4,  $\Omega_C^s = \Omega_A^s$  is the domain where the structure is constrained to have only solid material "A", and  $\Omega_s^D$  is the structural domain on which the optimization algorithm can prescribe variable topology which consists of both material A and B (or material A and void). Therefore,  $\Gamma^{fsi} = \Omega^f \cap \Omega_A^s$ , and the total structure volume consists of the union of the two domains  $\Omega^s = \Omega_D^s \cup \Omega_C^s$ . Further,  $\Omega_D^s = \Omega_A^s \cup \Omega_B^s$ .  $\Omega_C^s$  is designated to be one layer of elements along the FSI interface on the structural side. In the density based problems the elemental densities are constrained to have the upper limit. In the LS-XFEM the Level Set values are constrained to be the same sign on all nodes on each volume element along the FSI interface.

#### 3.1. Solid Isotropic Material Penalization

The physical design variables are the elemental structural elastic modulus ( $E^{(e)}$ ) and structural density ( $\rho^{s(e)}$ ). First an auxiliary elemental value  $\bar{s}$  is computed using the exponential penalization:

$$\bar{s} = \frac{\sum_{i=1}^{N_{nodes}^{(e)}} s_i}{N_{nodes}^{(e)}} \quad (15)$$

$$E^{(e)} = E_1 \bar{s}^\beta \quad (16)$$

$$\rho^{s(e)} = \bar{s} \quad (17)$$

$$(18)$$

Where  $E_1$  is the maximum value of structural elastic modulus and structural density, and the value used for phase (A) in the LS-XFEM cases. Note that the density

$\rho^{s(e)}$  is only used for the volume constraint, as the structural mass has no relevance in the steady state problem studied.  $N_{nodes}^{(e)}$  is the number of nodes on element element (e). Note equations (16) and (17) serve to smooth the design space, rather than use a gradient smoother [25].

### 3.2. LSM-XFEM Optimization and Regularization

Level Set optimization problems are typically slow to converge [30], and have oscillatory sensitivity at the interface. We introduce two methods to reduce spurious, ill conditioned, and slow converging design evolutions: smoothing and regularization. In regions away from the interface between material (A) and (B) the LS values are constant and therefore provide no calculable gradient. The Levelset values  $\phi_i$  are an explicitly prescribed function of the optimization variables  $s_i$ :

$$\phi_i = \frac{\sum_{j=1}^N \max(0, (r - d_{ij}) s_j)}{\sum_{j=1}^N \max(0, (r - d_{ij}))} \quad (19)$$

Equation (19) smooths out the "plateau" to allow for more gradient information to be available to the optimization algorithm thus improving design convergence. Here  $\phi_i$  is the Levelset scalar value at the  $i$ th node,  $d_{ij}$  is the distance from the  $i$ th node to the  $j$ th node.  $r$  is the so-called smoothing radius typically set to be approximately 1.5 the length of one design element.

To address the oscillatory interface sensitivity and the resulting creation of small, spurious surface features we apply a perimeter penalty in the optimization objection function. The interface perimeter (surface area in 3D) penalty introduces a "surface tension" to regularize the Level Set field and counteract any unrealistic interface geometries.

Due to a high number of design variables and a small number of constraints, we employ the Globally Convergent form of the Method of Moving Asymptotes [28] We use an adaptation of 0.7 and a step size of 0.02 for all results shown here.

#### 4. Numerical Examples

In all examples presented the objective is to minimize strain energy of the structure, subject to a volume constraint:

$$\begin{aligned} & \underset{s_i}{\text{minimize}} \quad z(s_i) \\ & \text{subject to} \quad g(s_i) = \frac{1}{n^V V_T} \int_{\Omega^s} d\Omega^s - 1.0 \leq 0 \end{aligned} \tag{20}$$

where the objective function is:

$$z(s_i) = \begin{cases} k_D \int_{\Omega^s} \sigma_{ij}^s \epsilon_{ij}^s d\Omega^s & \text{for SIMP,} \\ k_D \int_{\Omega^s} \sigma_{ij}^s \epsilon_{ij}^s d\Omega^s + k_P \int_{\Gamma_{A,B}^s} d\Gamma_{A,B}^s & \text{for LS-XFEM.} \end{cases}$$

Where  $n^V$  is the maximum volume fraction allowed, and  $V_T$  is the total volume if the structural domain is completely filled with material (A).  $k_D$  and  $k_P$  are weighting factors for the strain energy and perimeter, respectively. Typically  $k_D$  is between one and two orders of magnitude larger than  $k_P$ , as was used in the results shown here.

The design criteria (objective and constraint) sensitivities to the design variables ( $s_i$ ) are computed using the adjoint method. The Jacobian of the state equations (1) - (3) and derivative of criteria with respect to  $s_i$  are computed using analytical implementations, and elemental residuals and perimeter calculations are computed via central difference.

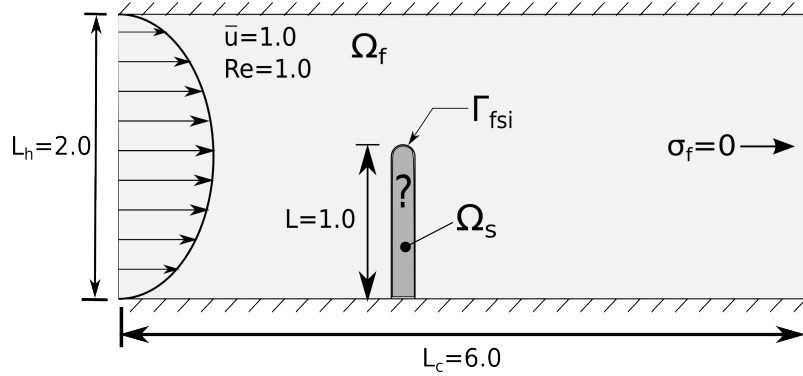


Figure 5: Two-Dimensional Beam Problem Setup. The width of the beam is 0.1 meters.

We use the iterative linear solver Generalized Minimum Residual Method (GMRES) and the Dual Threshold Incomplete LU Factorization (ILUT) preconditioning scheme to solve the linear systems in both the forward and backward (adjoint) computations. The first set of examples are two-dimensional beam optimization problems solved with both density and LS-XFEM. We investigate multi-phase results for both methods, as well as "material-void" examples. The second set of numerical examples consists of a three-dimensional analogue to the beam problem with a rectangular wing in a channel.

#### 4.1. Two-Dimensional Beam in a Parabolic Fluid Channel

A flexible structure is immersed in a fluid channel with stick conditions at both the top and bottom of the channel. A parabolic velocity profile is prescribed at the inlet, and a traction free condition is prescribed at the outlet. We limit the volume fraction to 60% ( $n^V = 0.6$ ). Figure 5 illustrates the problem setup and relevant flow parameters which result in a Reynolds number of 1.

The elastic modulus ( $E_1$ ) used for all two-dimensional examples is 40 kPa, and

Table 1: Computational Mesh Attributes.

Configuration	Structural Nodes	Fluid Nodes	Approx. Struc. Element Width
1	2736	7598	0.005 [m]
2	10259	23768	0.002 [m]

Poisson's ratio is 0.33. Newton's method was used to drive the global (fluid, fluid mesh, and structure) FEM residual norm to 1.0e-5 on each optimization iteration forward problem. The SIMP penalty parameter  $\beta$  was 3.5 in all cases presented here. The LS-XFEM routines use an initial "hole" radius of 0.038 meters, and a smoothing radius of 1.5x the average structural element size. Note that the same fluid and structure meshes are used in both the SIMP and XFEM routines, which are given in Table 4.2. The flow solutions for both the SIMP and LS-XFEM routines are approximately the same, therefore we present the fluid velocity, fluid pressure, and fluid mesh contours in figure 6. For the remainder of the 2D beam problem results we give a fluid velocity "max" value to indicate variation in the fluid-structure interaction resulting from the design iteration process.

We present results for both "material-void" problem as well as a "two-phase" problem to illustrate the XFEM's natural extension to composite structure optimization, and further analyze similarities to the SIMP method. To perform density topology optimization for two phases we employ the elastic modulus function of the design variables (in contrast to equation 16):

$$E^{(e)} = E_2 - (E_1 - E_2) \bar{s}^\beta \quad (21)$$

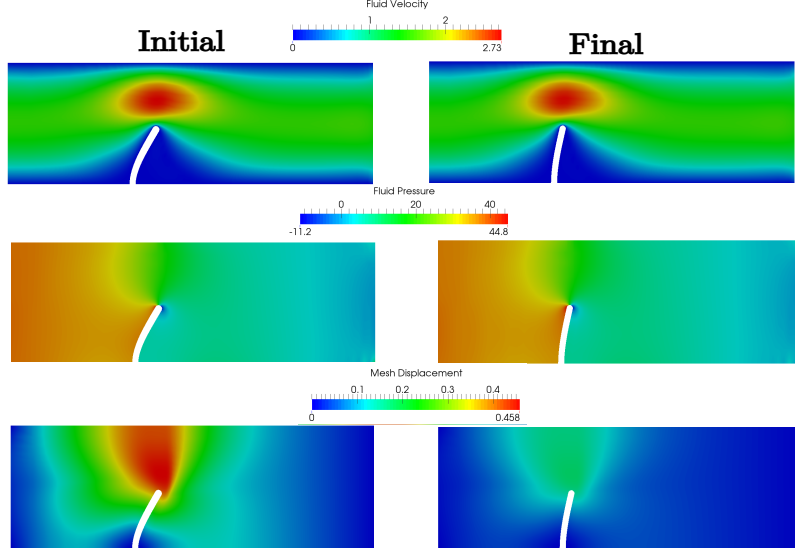


Figure 6: FSI flow solutions at the GCMMA optimality condition.

Figure 7 illustrates the objective evolution and snapshots of the structural topology throughout the GCMMA iteration process. The initial Level Set configuration is also given in figure 7. We infer that the SIMP method yields a smooth, quick convergence to the optimality point shown in the last snapshot. We expect the Level Set routine to be slower to converge, however in the context of Fluid-Structure interaction we observe multiple spikes. This search process results in ill-posed structural geometries and lead to extreme deformation, as can be seen at the "jump" points in figure 7. We emphasize the robustness of the monolithic solver in conjunction with the ALE method to allow high levels of fluid mesh deformation. Figure 8 shows the optimal designs for both methods on both meshes with and without an auxiliary material. We point out that the LS-XFEM yields the "best" solution with the least strain energy employing a second phase elastic modulus of  $E_2 = \frac{E_1}{10}$ , but only marginally better. Secondly, SIMP yields

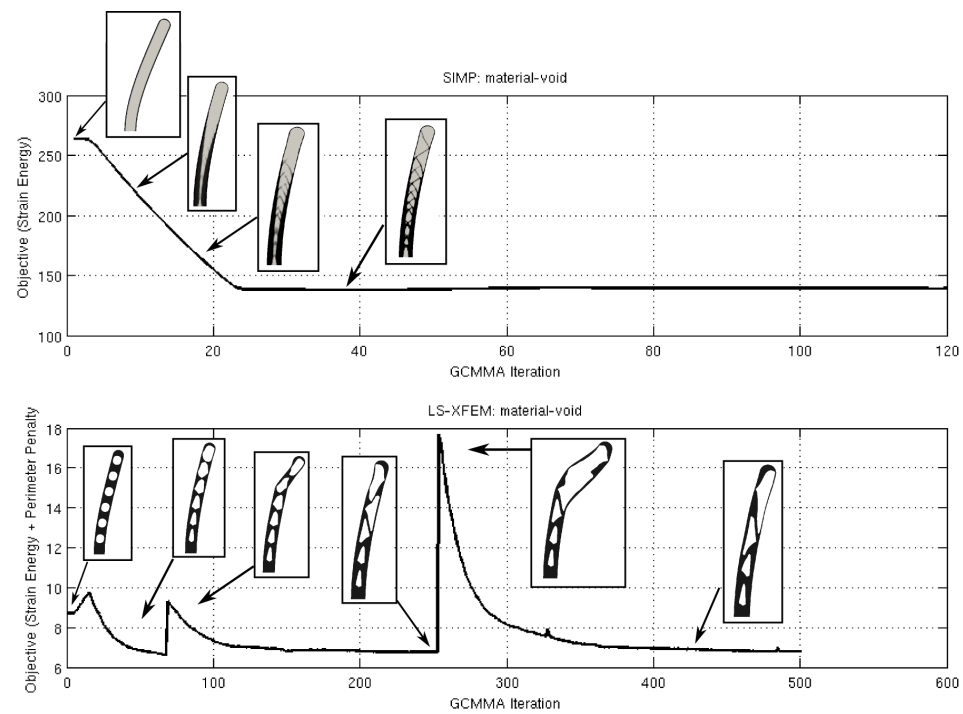


Figure 7: SIMP and LS-XFEM objective evolution for the "material-void" problem on the coarse grid.

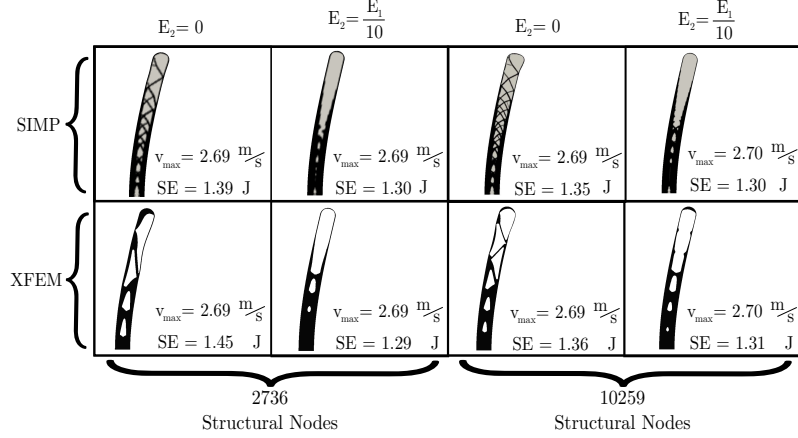


Figure 8: Comparison of SIMP and LS-XFEM for both mesh resolutions and second phase material.

relatively (in the context of the structural space) fuzzy geometries where as expected the LS-XFEM provides crisp, swept molds. SIMP displays some form of mesh dependence with an increasing number of "ribs" per mesh refinement, and this is seen to some degree with the LS-XFEM, yet not as severely. Finally we study the effect of different second phase structural materials as compared to the "material-void" problem. Figure 9 shows the results for a sweep of secondary elastic modulus values given by equation 21. We deduce that as the secondary material is increased in stiffness the optimal geometry maximizes material in the lower region, and minimizes material in the region near the top of the beam. This is because once the material is stiff enough to not allow a large deformation near the top of the beam (as seen in 7), the algorithm puts the stronger material closer to the base and the pinned boundary condition for more leverage.

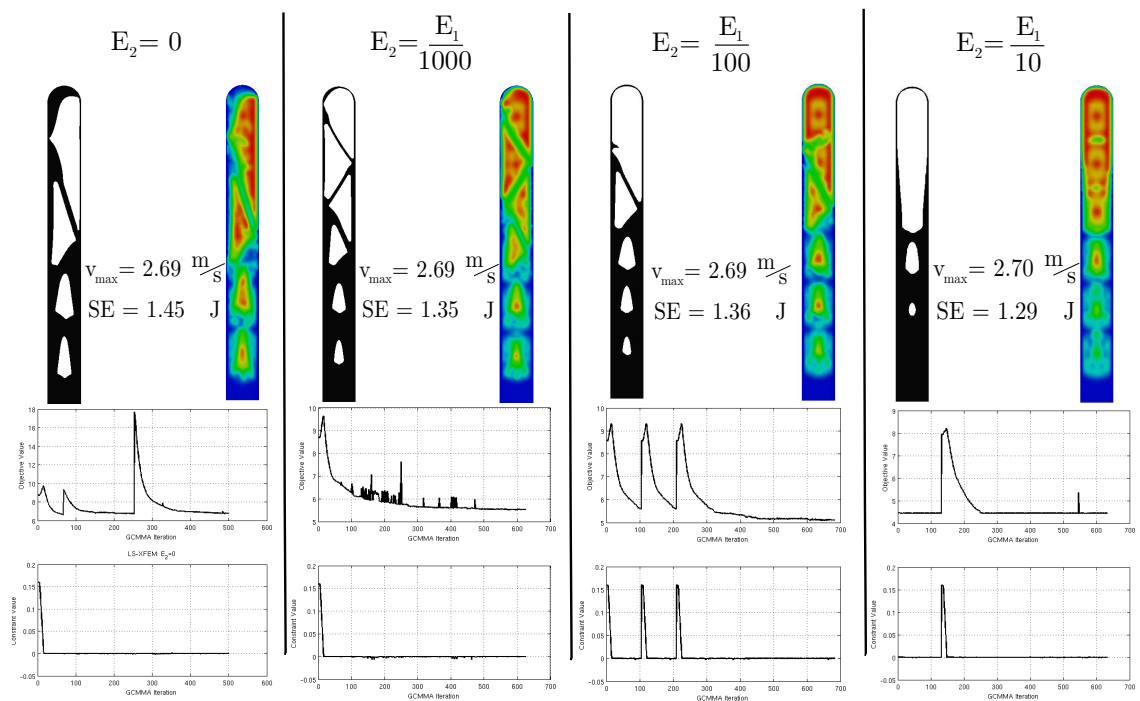


Figure 9: LS-XFEM with four different second phase materials on the coarse mesh.

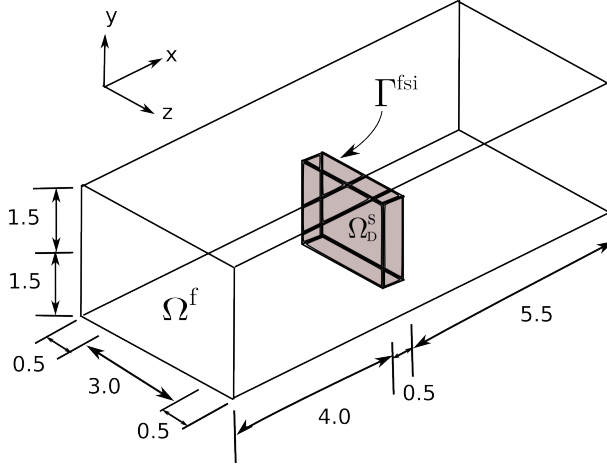


Figure 10: Flexible Wall FSI Problem Dimensions

#### 4.2. Three-Dimensional Flexible Wall in a Parabolic Fluid Channel

The three-dimensional analog to the previous beam example is given here as a flexible wall in a 3D channel. The channel inflow condition is parabolic in  $y$  and  $z$ , and the channel long axis the  $x$ -axis. A no-slip condition is prescribed on four walls down the length of the channel. The outflow condition is not prescribed and is left free. The channel dimensions are given in figure 10. Extending the current framework to three dimensions requires parallel computing and use of iterative linear solvers. These are two details are the paramount challenges in 3D computational mechanics. A purely fluid dynamics problem can prove difficult due to the addition flow modes, and introducing a nonlinear coupling with a flexible structure only magnifies the ill-condition on the global system of equations. Here robust and aggressive pre-conditioners are a requirement of not only the forward analysis, but the adjoint calculation also, to ensure accurate sensitivities.

As in the previous example, we optimize a structure using the SIMP density

Table 2: Computational Mesh Attributes.

Configuration	Structural Nodes	Fluid Nodes	Approx. Struc. Element Width
1	24576	82864	0.0037 [m]
2	61440	143856	0.0029 [m]

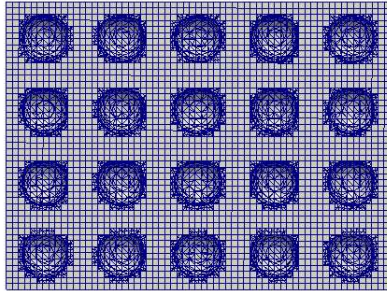


Figure 11: XEFM Triangulate (Tetrahedra) Initial Mesh Topology for Mesh Configuration 2.

penalization method, and the proposed Level Set / extended finite element method with a Reynolds number of 1.0 flow. Again, we ensure one layer of uninterseeted (Level Set) / full density (SIMP) structural elements on the fluid-structure interface. The simulations are done on two 3D grids: The elastic modulus for the structure is  $E^s = 5.0e3$ , and  $n^V = 0.60$ .  $k_P$  and  $k_D$ , the perimeter and displacement (strain energy) penalty multipliers used, are 0.01 and 100, respectively. In the density simulation, the entire structural volume is initialized to 0.6 density, and in the Level Set simulation the structural volume is initialized with 20 spheres (4 in the y-direction, 5 in the z-direction) of radius 0.12 m. The initial mesh tetrahead / hexahedra topology is shown in figure 11 for the 2cd mesh configuration. The velocity solution is shown in figure 12 in the Lagrangian deformed state, at the Level Set initial design solution, where the red lines are fluid streamlines. The

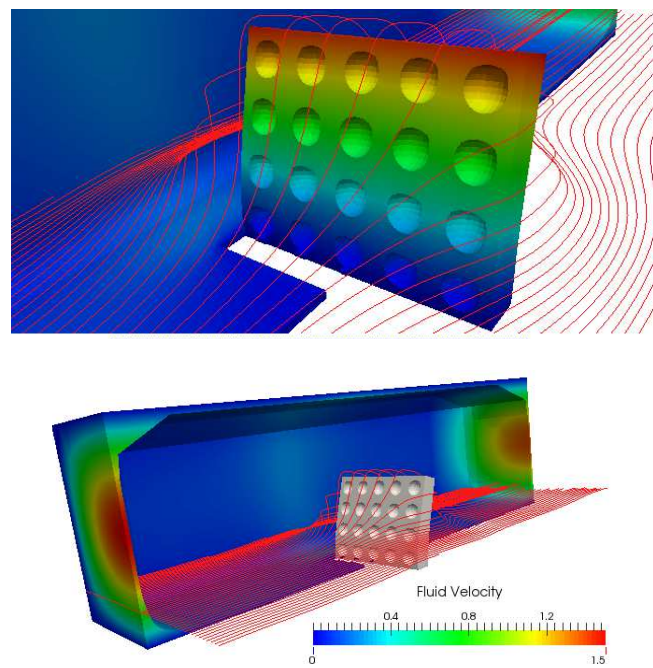


Figure 12: Deformed configuration in channel with velocity contours. The leading half of the wall has been cut away to show the topology. The red lines are fluid streamlines.

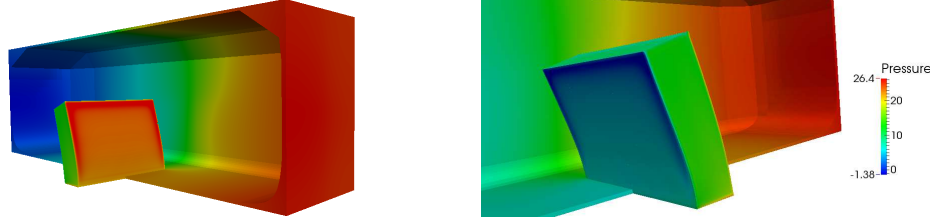


Figure 13: Pressure solution at initial design configuration.

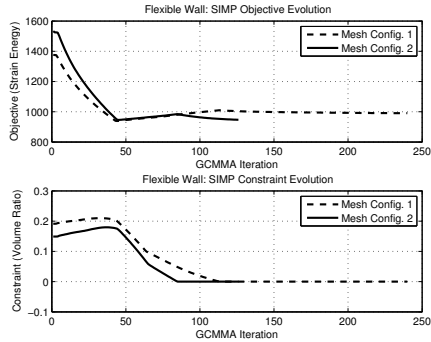


Figure 14: (i)

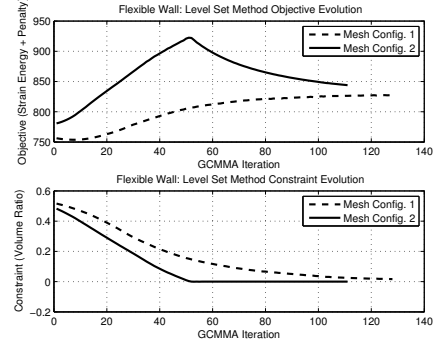


Figure 15: (ii)

Figure 16: (i) Objective and constraint evolution for the LSM-XFEM method. (ii) Objective and constraint evolution for the SIMP method.

pressure contours at the initial optimization iteration are given in figure 13. The SIMP method uses a exponent penalty of  $\beta = 3.5$ , and the strain energy is scaled by 100 ( $k_D$  from equation 20). The evolution of the objective and constraint for both SIMP and LSM-XFEM are illustrated in figure 16. The xy-plane view of the final deformed structural designs for both LSM-XFEM and SIMP in figure 21. A graphical evolution of the Level Set zero-surface, colored by displacement contours, is given in figure 22.

The yz plane view of the final structural geometries (undeformed) is given in figure 23.

In the three dimensional flexible wall case, the LSM-XFEM performed signifi-

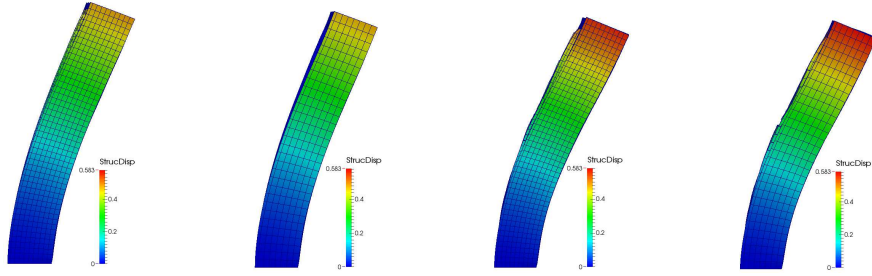


Figure 17: (i)

Figure 18: (ii)

Figure 19: (iii)

Figure 20: (iv)

Figure 21: (i) LSM-XFEM Mesh Config. 2. (ii) LSM-XFEM Mesh Config 1. (iii) SIMP Mesh Config. 2. (iv) SIMP Mesh Config. 1

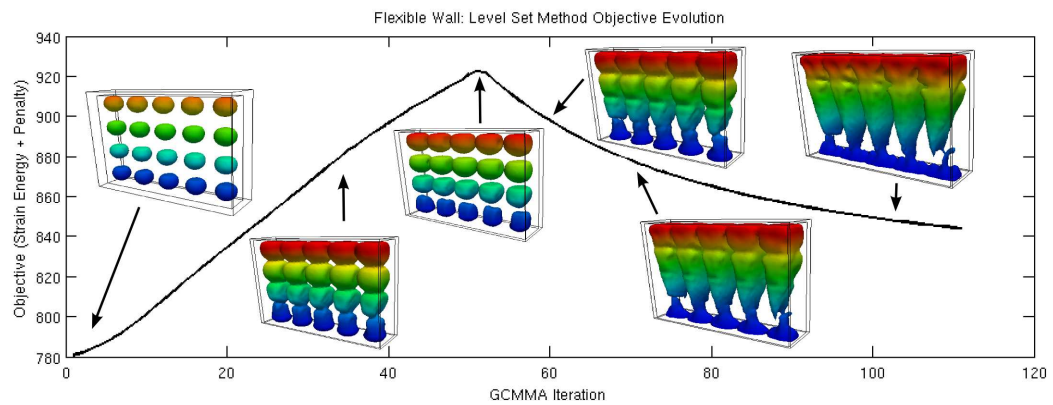


Figure 22: Final structural topology configurations for both XFEM and SIMP, with cut half-way through x-thickness.. Dark color in the SIMP simulation is material, and light color is low density. The LSM-XFEM images show the structural phase geometry.

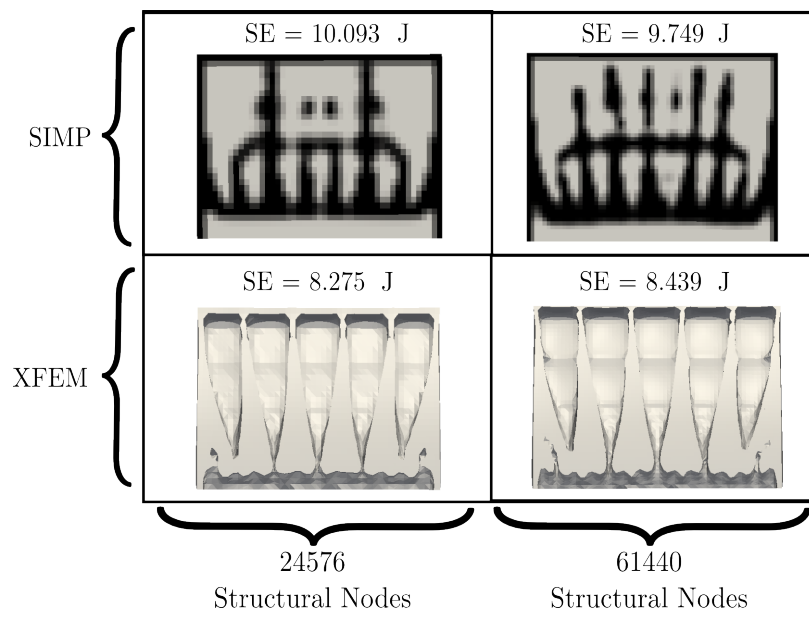


Figure 23: Final structural topology configurations for both XFEM and SIMP, with cut half-way through x-thickness.. Dark color in the SIMP simulation is material, and light color is low density. The LSM-XFEM images show the structural phase geometry.

cantly better on both mesh configurations. Further, the design geometry is smooth and crisp. Again, as in the two dimensional example, the designs are different, but observe similar overall similarities. The top right and top left regions, for example, are void for both, as well as the very bottom region across the z-direction.

## 5. Conclusions

We have introduced the Level Set / extended Finite Element Method for topology optimization of fluid-structure interaction problems. We demonstrated both a two dimensional and a three-dimensional example for low Reynolds number flow, optimizing the stiffness of the structure immersed in the flow. The LSM-XFEM requires more work to develop, and does not converge as quickly or monotonically as the traditional method. However, it is apparent, especially in the context of three-dimensional fluid-structure interaction problems, the ability to resolve fine features on a relatively coarse mesh is significant. Further, based on the examples showed, there is not much gained from refining the design domain further. In addition, for three dimensional problems the SIMP method breaks down when compared to performance of the LSM-XFEM.

## Acknowledgments

The authors acknowledge the support of the National Science Foundation under grants ...

## References

- [1] M. Allen and K. Maute. Reliability based optimization of aeroelastic structures. In *Proceedings of the 9th AIAA/ISSMO Symposium on Multidisciplinary Analysis and Optimization, September 4-6, Atlanta, GA*, number 5560. AIAA/ISSMO, 2002.
- [2] M. Allen and K. Maute. Reliability based optimization of aeroelastic structures. *Structural and Multidisciplinary Optimization*, 24:228–242, 2004.

- [3] M. P. Bendsøe and O. Sigmund. *Topology Optimization: Theory, Methods and Applications*. Springer, 2003.
- [4] T. Borrrell and J. Petersson. Topology optimization of fluids in Stokes flow. *International Journal for Numerical Methods in Fluids*, 41(1):77–107, 2003.
- [5] X. Duan, Y. Ma, and R. Zhang. Shape-topology optimization for navier-stokes problem using variational level set method. *Journal of computational and applied mathematics*, 222(2):487–499, 2008.
- [6] T. Dunne and R. Rannacher. Adaptive finite element approximation of fluid-structure interaction based on an eulerian variational formulation. In H.-J. Bungartz and M. Schfer, editors, *Fluid-Structure Interaction*, volume 53 of *Lecture Notes in Computational Science and Engineering*, pages 110–145. Springer Berlin Heidelberg, 2006.
- [7] C. A. Felippa, K. Park, and C. Farhat. Partitioned analysis of coupled mechanical systems. *Computer methods in applied mechanics and engineering*, 190(24):3247–3270, 2001.
- [8] T. P. Fries. The intrinsic xfem for two-fluid flows. *Int. J. Numer. Meth. Fluids*, 60(4):437–471, 2009.
- [9] A. Gerstenberger and W. A. Wall. An embedded dirichlet formulation for 3d continua. *International Journal for Numerical Methods in Engineering*, 82(5):537–563, 2010.
- [10] A. Hansbo and P. Hansbo. A finite element method for the simulation of strong and weak discontinuities in solid mechanics. *Computer Methods in Applied Mechanics and Engineering*, 193(33-35):3523 – 3540, 2004.

- [11] M. Howard and S. Bova. Coupling strategies for high-speed aeroheating problems. In *Aerospace Sciences Meetings*, pages –. American Institute of Aeronautics and Astronautics, 2011.
- [12] K. A. James, J. Martins, and J. Hansen. Three-dimensional structural topology optimization of an aircraft wing using level set methods. In *Proceedings of the 12th AIAA/ISSMO Multidisciplinary and Optimization Conference, Victoria, British Columbia, Canada*, pages 1–12, 2008.
- [13] M. Kabiri and F. J. Vernerey. An xfem based multiscale approach to fracture of heterogeneous media. *International Journal for Multiscale Computational Engineering*, 11(6):565–580, 2013.
- [14] S. Kreissl and K. Maute. Topology optimization for unsteady flow. *International Journal for Numerical Methods in Engineering*, 87:1229–1253, 2011.
- [15] S. Kreissl and K. Maute. Levelset based fluid topology optimization using the extended finite element method. *Structural and Multidisciplinary Optimization*, pages 1–16, 2012.
- [16] S. Kreissl, G. Pingen, and K. Maute. An explicit level set approach for generalized shape optimization of fluids with the lattice boltzmann method. *International Journal for Numerical Methods in Fluids*, 65(5):496–519, 2011.
- [17] D. Makhija and K. Maute. Numerical instabilities in level set topology optimization with the extended finite element method. *Structural and Multidisciplinary Optimization*, 2013.
- [18] K. Maute, M. Nikbay, and C. Farhat. Sensitivity analysis and design optimization of three-dimensional nonlinear aeroelastic systems by the ad-

- joint method. *International Journal for Numerical Methods in Engineering*, 56(6):911–933, 2003.
- [19] K. Maute and G. Reich. An aeroelastic topology optimization approach for adaptive wing design. In *Proceedings of the AIAA/ASME/AHS Adaptive Structures Conference, April 19-22, Palm Springs, CA*, number 1805. AIAA/ASME/AHS, 2004.
- [20] K. Maute and G. Reich. Integrated multidisciplinary topology optimization approach to adaptive wing design. *AIAA Journal of Aircraft*, 43(1):253–263, 2006.
- [21] S. J. Osher and J. A. Sethian. Fronts propagating with curvature dependent speed: algorithms based on Hamilton-Jacobi formulations. *Journal of Computational Physics*, 79:12—49, 1988.
- [22] C. Othmer. CFD topology and shape optimization with adjoint methods. In *VDI Fahrzeug- und Verkehrstechnik, 13. Internationaler Kongress, Berechnung und Simulation im Fahrzeugbau*, Würzburg, Germany, 2006.
- [23] S. Ragon, Z. G-uacute, rdal, R. Haftka, and T. Tzong. Bilevel design of a wing structure using response surfaces. *Journal of aircraft*, 40(5):985–992, 2003.
- [24] J. Sethian. *Level Set Methods*. Cambridge University Press, 1996.
- [25] O. Sigmund and K. Maute. Sensitivity filtering from a continuum mechanics perspective. *Structural and Multidisciplinary Optimization*, pages 1–5, 2012.

- [26] B. Stanford and P. Beran. Optimal structural topology of a platelike wing for subsonic aeroelastic stability. *American Institute of Aeronautics and Astronautics*, 2011.
- [27] B. Stanford and P. Ifju. Aeroelastic topology optimization of membrane structures for micro air vehicles. *Structural and Multidisciplinary Optimization*, 38(3):301–316, 2009.
- [28] K. Svanberg. The method of moving asymptotes - a new method for structural optimization. *International Journal for Numerical Methods in Engineering*, 24(2):359–373, 1987.
- [29] T. E. Tezduyar, S. Mittal, S. E. Ray, and R. Shih. Incompressible flow computations with stabilized bilinear and linear equal-order-interpolation velocity-pressure elements. *Computer Methods in Applied Mechanics and Engineering*, 95:221–242, 1992.
- [30] N. van Dijk, K. Maute, M. Langelaar, and F. Keulen. Level-set methods for structural topology optimization: a review. *Structural and Multidisciplinary Optimization*, pages 1–36, 2013.
- [31] T. Wick. Fully eulerian fluidstructure interaction for time-dependent problems. *Computer Methods in Applied Mechanics and Engineering*, 255(0):14 – 26, 2013.
- [32] G. H. Yoon. Topology optimization for stationary fluid-structure interaction problems using a new monolithic formulation. In *8th World Congress on Structural and Multidisciplinary Optimization*, 2009.